SCUOLA DI DOTTORATO
UNIVERSITÀ DEGLI STUDI DI MILANO-BICOCCA

Department of Materials Science

PhD program in Materials Science and Nanotechnology
XXXVI Cycle

Processing of single-element 2D materials towards integration in electronic devices

Surname: **Massetti** Name: **Chiara**

Registration number: **877387**

Tutor: **Prof. Emiliano Bonera**

Supervisor: **Dr. Alessandro Molle**

Coordinator: **Prof. Francesco Montalenti**

ACADEMIC YEAR 2022/2023

"Vita brevis, ars longa, occasio praeceps,
experimentum pericolosum, iudicio difficile."

Ippocrate

Contents

List of Figures

List of Tables

Introduction

In the world of materials science, the mechanical exfoliation of graphene, the well-known single layer of carbon atoms, certainly marked a turning point date for all subsequent materials research [1, 2]. The extraordinary properties predicted for the so-called two-dimensional (2D) materials have led, in recent decades, to an ever-increasing interest of the scientific community, which has turned into a huge production of appealing materials which differ in both properties and methods of synthesis [3]. In general, the group includes materials formed by a single or a few atomic layers which can range from insulators, e.g., hexagonal boron nitride (h-BN) [4], to semiconductors, such as molybdenum disulfide (MoS_2) [5] and black phosphorus [6], or even to superconductors, e.g., niobium diselenide ($NbSe_2$) [7].
In this large heterogeneous group, there is a class of single-element 2D materials which are called Xenes [8] precisely to recall the analogy with graphene and, at the same time, to emphasize the substantial difference with the latter one, since they are formed from X elements other than carbon. Originally, this term was used to refer only to group IVA of the periodic table, but in recent years it has also been extended to some elements of the groups IIIA, VA and VIA. Their artificial nature also outlines their main peculiarity, which is to be characterized by a pseudo-planar lattice. This represents an additional degree of freedom called buckling, namely the vertical displacement between the top and bottom atoms, intrinsically related to a state of mixed sp^2-sp^3 hybridization [9]. This aspect can result in a high environmental instability of the materials when exposed to ambient conditions and it represents one of the hardest challenges to be faced when working with Xenes. It then becomes clear that the substrate on which the material is grown plays a crucial role both in its resulting properties and in terms of the interaction that affects its subsequent device integration.
The purpose of this work of thesis is to study and investigate the actual

manipulation of Xenes from a processing point of view, in order to discuss and solve the main issues toward the implementation into device structures. In particular, the considered material will be silicon (resulting in silicene) because it is the most attractive in terms of integration and compatibility with a large part of the existing technology, and tin (resulting in stanene) which will be discussed and treated either as a template layer for the silicene growth and as a promising 2D topological material.
For each type of sample, the processing schemes are first developed and optimized in order to provide access to characterization techniques used to probe the materials properties.
The first issue that is presented is the stabilization of silicene out of the ultra-high-vacuum system used for its synthesis. A first proposed solution, based on a capping layer deposition directly after the growth, such as an alumina layer [10], allows the Xenes to be stabilized and protected in environmental condition. However, the problem occurs again when the material has to be transferred from the growth substrate to the desired one. By taking advantage of the interface engineering of silicene-stanene heterostructures [11], the role of stanene as a sacrificial layer against silicene degradation is tested, paving the way to the subsequent transfer to the device.
After dealing with the full stabilization, it is possible to exploit the silicene properties by trying to prototype possible applications that best suit its intrinsic characteristics. For example, it should be emphasized as recently, in the 2D materials framework, there has been an increasing research focused on flexible materials [12, 13], with the ultimate goal of a completely bendable device scheme for sensing and strain engineering applications. In this context, by exploiting the cleavable nature of the growth substrate, the stabilized silicene can be an excellent alternative, especially for what concerns the integration and compatibility with the complementary metal-oxide semiconductor (CMOS) technology.
Finally, stanene is also regarded as a paradigmatic material from a topological point of view and, in particular, it will be treated in the form of few-layer stanene to try to assess its nontrivial properties.

Chapter 1

Two-dimensional materials

In order to give the most general possible definition for two-dimensional (2D) materials, it can be stated that they refer to a set of crystalline materials consisting of a single layer of atoms. Despite their simple and straightforward definition, actually their handling and processing always present new challenges and non-trivial difficulties to consider, especially when the aim is to try to integrate them into a working device: most of them are related to the interaction which the material has with the external environment and the substrate, its quality and the precise control of its interfaces. However, although difficult to manipulate, the exceptional properties that arise when dimensionality is reduced, such as high carrier mobility [14], a tunable bandgap [15], non-linear optical properties [16] or mechanical elasticity [17], combined with the technological progress which inevitably requires ever more extreme miniaturization, lead to an ever wider study of them.

1.1 Overview of the 2D world

Since the exfoliation of graphene [1], the class of 2D materials has seen an impressive increase, both in terms of material types and synthesis methods (see Figure 1.1a). On this last aspect, the first major distinction can be made by identifying a top-down approach, thus based on obtaining the material from the solid bulk through physical or chemical processes, from a bottom-up strategy, which basically involves the direct growth of the material itself by means of physical and chemical depositions (as schematized in Fig. 1.1b).
The positive aspects of the top-down approach are practically the ease of execution, the low cost, and the versatility of this method that allows

the material to be transferred to any desired substrate. In this case, some of the most commonly used techniques are, for example, the mechanical or liquid-phase exfoliation. The biggest disadvantage, however, relates to the low yield and, especially, to the randomness of the entire process, which does not allow for full control over some key parameters, such as thickness. It should also be emphasized that this method is only suitable to those bulk crystals which have a layered structure and, as we will see in the case of Xenes, is therefore not applicable to every type of material.

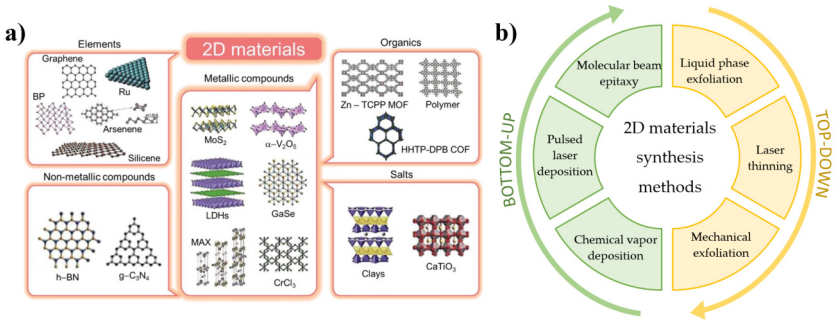

Figure 1.1: ***(a)*** *Classification of the main types of 2D materials Adapted from Ref. [18].* ***(b)*** *Schematic summary of the main fabrication methods of 2D materials in the case of bottom-up and top-down approaches.*

On the other hand, the bottom-up strategy, based on the growth of the material from the fundamental atomic or molecular level, is more oriented to the mass production horizon. The most commonly used techniques in this context are Chemical Vapor Deposition (CVD) and Physical Vapor Deposition (PVD). However, like any other method, also in this case there are negative aspects and challenges which are mainly related to the actual cost of the technologies employed, the special care required during the growth and the choice of suitable technologically relevant substrates.

With regard to graphene, for example, both approaches are feasible. In 2004, graphene was first mechanically exfoliated from graphite [1], but at the same time, various methods have been investigated to achieve large-scale growth by CVD [19, 20]. In many aspects, graphene is an outstanding 2D material, thanks to both its properties and the whole research that has subsequently resulted. Its crystal structure is honeycomb-like and consists of sp^2-hybridized carbon atoms that thus form a perfect planar lattice, as shown in Fig. 1.2a. Concerning the electrical properties, it is a zero-gap semimetal where, therefore, the valence and conduction

band merge at the Dirac points, which are characterized by a local linear dispersion [21].
Its extraordinary properties are related to its high carrier mobility [22, 23], tunable optical properties [24], its strength [25] and high thermal conductivity [26]. At the same time, the missing gap represents a very limiting factor from the aspect of applications and, although it is possible to tune the band structure through different techniques [27, 28], there has been no actual breakthrough over the years.

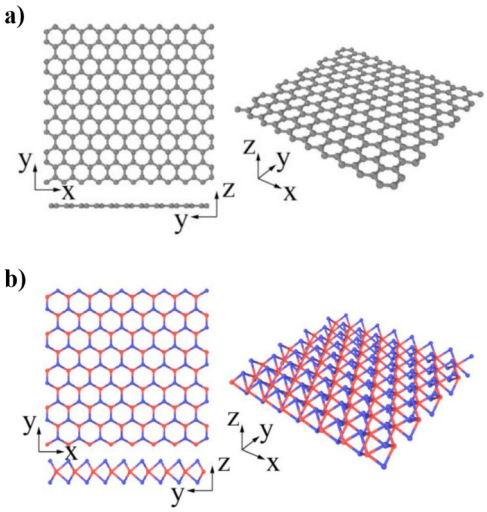

Figure 1.2: *Atomic model of the lattice structure of* ***(a)*** *graphene and* ***(b)*** *transitional metal dichalcogenides (TMDs). Adapted from Ref. [29].*

Beyond graphene, however, there are other groups of similar crystalline 2D materials which may have completely different properties [30]. A significant group is represented, for example, by the layered van der Waals crystals which can easily be mechanically or chemically exfoliated to obtain single and few layers 2D materials. Their crystal structure is composed of layers of atoms covalently or ionically bonded, while the different layers are held together by weak van der Waals bonds perpendicular to the layers axis, which allows their easy exfoliation. This group includes, for instance, the transition-metal dichalcogenides (TMDs) which are atomically thin materials composed of one layer of transition-metal M atoms sandwiched between two layers of chalcogen atoms X, with typical MX_2 stoichiometry (see Figure 1.2b). The most common and studied ones are molybdenum disulfide (MoS_2) [31], molybdenum ditelluride ($MoTe_2$) [32] or tungsten disulfide (WS_2) [33].

In particular, these are semiconductive with a tunable and thickness-dependent bandgap, which is typically between 1 and 2.2 eV and, hence, is very convenient in nanoelectronic [34] and optoelectronic [35] applications.
Another type of 2D material that belongs to the family of van der Waals solids is the hexagonal boron nitride (h-BN) [36], characterized by a wide bandgap of ~ 6 eV which makes it an ideal candidate for electrical insulation and, specifically, a great gate insulating layer for graphene [37].
Finally, it is also possible to add other types of materials to the list of 2D layered solids that attract a lot of attention due to their potential topological properties [38], represented by other chalcogenides such as Bi_2Te_3 [39] and Sb_2Te_3 [40].
It should be remembered in general, that all the 2D materials presented so far can be obtained either through a top-down approach, due to their layered nature, but also through the bottom-up method. It is clear that, with the increase of interest in them, the problem of scalability becomes a challenge to be faced if the aim is to target industrial applications. So far, the most widely used method of synthesis, for most of them, is growth by CVD, although perfect control of the growth process is not always easy to achieve and problems related to the non-uniform thickness and the defects presence have to be taken into account.

1.2 The Xenes generation

The 2D world is experiencing a continuous expansion and among its members, here we focus on the class of elementary 2D crystals, termed Xenes (see Fig. 1.3a), which possess a honeycomb-like lattice structure similar to that of graphene and which has seen the discovery and expansion in the last decade. Originally, the term was used to refer only to the elements of group 14 of the periodic table (in particular Si, Ge and Sn resulting in silicene, germanene and stanene, respectively) characterized by the absence of a bulk crystal from which exfoliate layers, and therefore only achievable by means of 2D crystal growth. These elements gave rise to the first-generation Xenes and the key technique in this case, as described further below, is growth by epitaxy.
Recently, the class of the Xenes has been extended to include other elements from groups 13, 15 and 16 of the periodic table that have an electronic configuration different from carbon and which can also be obtained by methods different from epitaxy, such as CVD. In Figure 1.3a the main types of Xenes discovered to date are shown. Anyway, in this

thesis work, only Xenes belonging to the first generation will be treated, specifically silicene and stanene, and the only growth technique used will be through epitaxy (see Chapter 2). The main feature of this group of materials is to have, compared with the flat structure of graphene, a buckled structure, where the hexagonal symmetry is still preserved (Figure 1.3b).

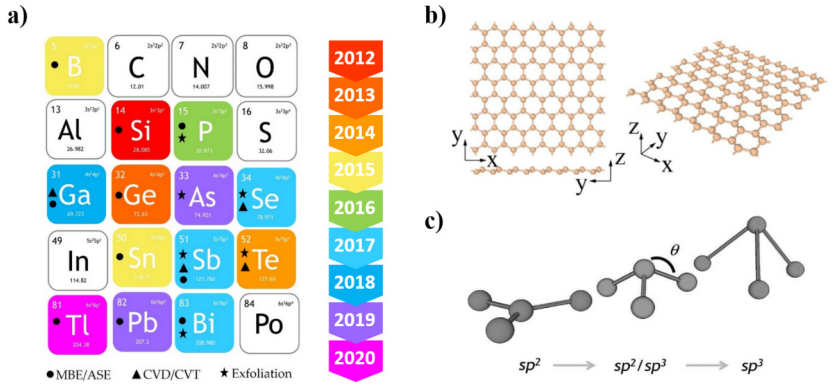

Figure 1.3: ***(a)*** *Periodic table where elements of 2D monoelemental crystals are highlighted and their respective methods of synthesis are given.* ***(b)*** *Typical buckled lattice structure of silicene, germanene and stanene.* ***(c)*** *Sketch of the evolution of the hybridization from sp^2 to sp^3. Adapted respectively from Ref. [8, 29, 41].*

This additional degree of freedom represented by buckling Δ (see Figure 1.3c) originates from the state of hybridization and, while graphene is characterized by a complete sp^2 hybridization, in the case of the Xenes, a mixed sp^2-sp^3 hybridization of the atomic orbitals occurs and represents the most favorable energy condition [42]. This peculiarity is what causes high environmental reactivity that results in rapid oxidation and degradation when the material is exposed to air. As will be seen later, the stability issue will be a key element to be taken into account during all the fabrication processes leading up to the realization of a device, and it is definitely one of the toughest challenges that I faced out in the present work. It should be noted that the process is favored when the grown material has a reduced thickness, compared to a multilayer growth where the first layers can be seen as sacrificial slowing down or inhibiting the degradation [43]. One possible solution, which has been employed over the years, is the post-growth encapsulation with a non-reactive protective layer [44, 45], which allows the sample to be handled outside of the growth vacuum conditions.

In the following, the essential aspects regarding silicene and stanene, as the main Xenes addressed in the present work, are reported.

1.2.1 Silicene properties

The atomic structure of what would later be termed as silicene was first theoretically predicted in 1994 through first-principles calculations [46] which showed that, in contrast to C atoms, in the case of Si and Ge, the atoms prefer to be arranged in a corrugated structure, as shown in Figure 1.4a, where the symmetry D_{6h} changes to the D_{3d} one. After the discovery of graphene [1], interest in this type of materials grew over the years and, first through tight-binding models [47] and, later through density functional theory (DFT) calculations [48], the electronic structure of silicene was also theorized. As mentioned before, silicene has the same honeycomb lattice structure of graphene with the only difference consisting in the presence of a vertical displacement perpendicular to the plane, which is relative to the sp^3 bonding.
In particular, two configurations more stable than the flat structure can be identified: a low-buckled (LB) one which corresponds to a partial sp^2-sp^3 hybridization with a buckling parameter of $\Delta_{LB} = 0.44$ Å and a high-buckled (HB) configuration, predominantly sp^3-like, with $\Delta_{HB} = 2$ Å. Although, from an energetic point of view, the HB configuration appears to be at lower energy, the phonon modes actually exhibit imaginary frequencies in most directions of the Brillouin zone, turning out that the LB configuration is the most stable one. This type of structure, with a lattice constant $a \sim 3.8$ Å, induces the p_z orbitals to combine with the s orbitals, resulting in a σ and π bands coupling.
This configuration shows a semimetallic character, where the π and π^* bands cross the Fermi level E_f resulting in a linear dispersion at the K and K' points (see Figure 1.4b), namely a Dirac cone, with a Fermi velocity of $\sim 10^6$ m/s [49].
From the experimental point of view, it should be noted that the lattice structure shown in Figure 1.4a refers to the freestanding form of silicene and, hence, the realization by means of growth techniques inevitably presents considerable differences. In fact, growth by epitaxy [50] necessarily takes place on a substrate that also plays a fundamental role in defining the properties of the material grown.
Not all substrates can be suitable for growth, as this only takes place in the case of commensurability between substrate and grown material, and the final atomic arrangement of the Xene will depend on the lattice match. For this reason, silicene itself has a polymorphic nature characterized by different deformed structures, each governed by hexagonal symmetries, which often coexist, even in the case of the same substrate,

and thus regarded as silicene phases.
The majority of the substrates used so far are metallic [51, 52, 53] and, in this thesis work, the material used as a template is Ag(111), which can be considered as the most investigated one since its hexagonal surface unit cell is nearly commensurate with the silicene one [54, 55]. Depending on different growth parameters, when silicene is grown on Ag(111), there are several possible phases [55, 56, 57, 58, 59], which over the years have been simulated and experimentally observed, for instance, through Scanning Tunneling Microscopy (STM).

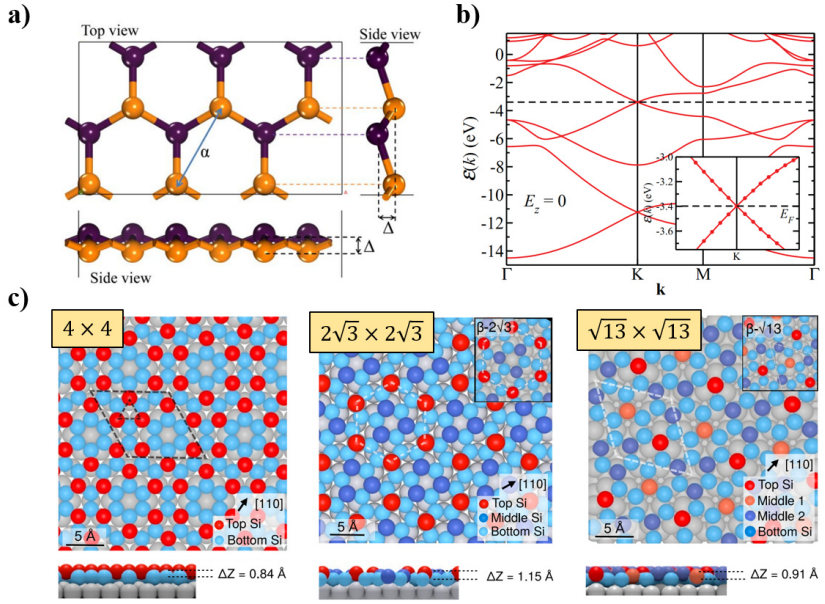

Figure 1.4: ***(a)*** *Atomic structure of silicene where the buckling parameter* Δ *and the hexagonal lattice constant* α *are highlighted.* ***(b)*** *Calculated band structure of silicene.* ***(c)*** *Top and side representations of the* 4×4, $2\sqrt{3} \times 2\sqrt{3}$ *and* $\sqrt{13} \times \sqrt{13}$ *silicene superstructures on Ag(111). Adapted respectively from Ref. [60, 49, 61].*

Structural models, obtained through DFT calculations, are illustrated in Figure 1.4c and respectively predict three representative silicene phases on Ag(111) denoted as 4×4, $2\sqrt{3} \times 2\sqrt{3}$ and $\sqrt{13} \times \sqrt{13}$. The common phase expression is based on the Wood notation [62] and identifies the size of the silicene supercell with respect to the Ag(111) surface unit cell, but omits, for the sake of clarity, the orientation with respect to the Ag[110] axis (which is respectively 0°, 30° and 13.9°). These are

just some of the multiple superstructures in which silicene can arrange itself when grown, in general, on metallic substrates. Although complex, several efforts have been made to define phase diagrams [63, 64] and predict the structural evolution of silicene as a function of the two key growth parameters, namely temperature and time of deposition: the balance of these parameters aiming a single phase selection leads to a non-trivial complexity of the Xene growth processing.
The as-grown silicene also differs from the freestanding case in terms of electronic properties since the interaction with the substrate must be taken into account. The metal substrate greatly influences the silicene electronic behaviour leading to a strong hybridization resulting in phase-dependent electronic structure for the supported silicene [65, 66, 54]. Hence, the interaction with the substrate poses a great challenge in the realization of a device since the actual decoupling is basically a non-trivial task.
This issue motivates the use, in the present work, of Ag(111) on mica substrate which in principle, after an *ad-hoc* transfer process, allows the thin layer of Ag ($\sim$ 300 nm) to be employed for electrical contacts acting on an Ag-free silicene conductive channel. At the same time, the problem of interaction with the substrate also opens the way for the study of heterostructures in which different layers of Xenes can be used as templates for the growth of silicene, in order to decouple it from the metal substrate. To address this issue, among the samples taken into consideration, I focused on silicene-stanene heterostructure configuration, first realized in 2021 [11]. All these aspects are discussed in Chapter 3.

1.2.2 Stanene properties

If we consider the bulk state, it is possible to find tin (Sn) in two allotropic forms: the first called α-Sn (or also grey tin), which corresponds to the stable phase at low temperatures, and a second one called β-Sn (or also white tin), which is obtained for temperature higher than 13.2 °C. The former has a diamond structure (see Fig. 1.5a) and is a gapless semiconductor, while the latter has a body-centred tetragonal structure and it is a metal. In 2013, a single layer of α-Sn, called stanene [67], was proposed and theorized for the first time. As can be seen in Figure 1.5b, stanene as well as silicene exhibits a hexagonal honeycomb structure characterized by a buckled shape with a lattice constant, obtained through DFT calculations, of $\sim$ 4.6 Å. As in the case of silicene, the used synthesis technique is growth by epitaxy, and the first experimental result was obtained on the bismuth telluride substrate (Bi_2Te_3) [68] and, subsequently, also on other materials such as indium antimonide (InSb) [69] and lead telluride (PbTe) [70]. For each of these substrates, as demonstrated also by STM

images, the obtained stanene has a smaller lattice constant compared to the simulated one, and the result is a lattice subjected to compressive strain with a highly buckled configuration. Obtaining a flatter stanene is possible if metallic substrates such as Ag(111) [71] or Cu(111) [72] are used.

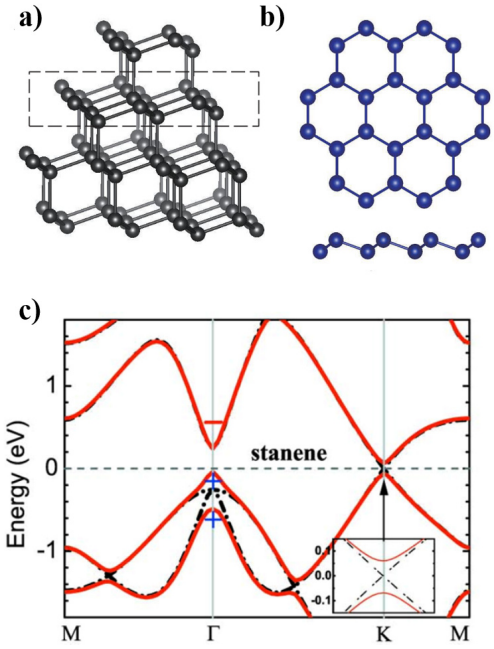

Figure 1.5: ***(a)*** *Bulk structure of α-Sn. Single layer of α-Sn (111) is highlighted by a black dotted rectangle.* ***(b)*** *Crystal structure for stanene.* ***(c)*** *Band structure of stanene without (black dash-dotted lines) and with (red solid lines) spin-orbital coupling. Adapted from Ref. [73, 67].*

In Figure 1.5c it is shown the calculated stanene band structure. As can be seen by observing the black dotted line, the bands cross linearly at the K and K' points, when spin-orbit coupling (SOC) is not considered. On the other hand, when SOC is included, as in the case of the red solid curve, there is a gap of ∼0.1 eV opening. Tin, indeed, is an element with a large atomic number, in comparison with silicon or germanium, so it has an intense SOC term which makes it a perfect candidate for being considered a topological material [67], as discussed in detail in Chapter 6.

The topological character can come out only if the cubic symmetry of the crustal lattice is broken and one way to get it is to take advantage of the

strain induced by the substrate on which Sn is grown. The strain, in fact, corresponds to applying a deformation to the material that changes the geometrical structure of the crystal, which is then reflected in a change in the electronic band structure and in a tuning of its physical properties. First-principles calculations in the case of InSb(111) substrate [74] predict that, in the case of compressive strain, a topological Dirac semimetal (TDS) [75] can be obtained, while in the case of tensile strain, few-layer stanene turns into a topological insulator (TI) [76].
It is interesting to note that a crossover between TDS and TI is possible by exploiting quantum confinement, that is, by reducing the thickness of the material of a 3D TDS to the 2D limit. In the case of Sn, the transition from α-Sn, which can be treated as 3D TDS, to stanene, which can be considered as 2D quantum spin Hall insulator, paves the way for many thickness-dependent opportunities for the system Sn on InSb.

1.3 Motivation and thesis outline

It is evident that Xenes have exceptional and interesting properties to explore but, at the same time, they are difficult to manipulate if compared to graphene or TMDs. The lack of their freestanding form and the necessity to employ a substrate for the epitaxial growth poses non-trivial challenges on two main fronts:

- the growth engineering, which requires the accurate control of parameters and the choice of an appropriate substrate
- the post-growth processing, which can get complicated and be necessary for characterization techniques or device architecture integration.

In this thesis work, silicene and stanene will be considered in order to investigate and solve the main issues toward the development of device platforms. Considering the high compatibility of silicene with all existing silicon-based technology, the scope of this work will focus on solving the major problems related to its processing schemes. While, since stanene is one of the most promising and attractive candidates in the field of topological materials [74], it will be investigated in the few-layer form through different types of characterizations.
The reason behind the study of these two materials is originated by the fact that the specific choice of a substrate determines both the direction of the potential application of Xenes and the development of the associated processing steps. For this reason, on one hand, the silicene can be taken as a case study to explore the possibility of growth and transfer of a standard Xene configuration grown on a metallic substrate, and on the

other hand, the few-layer stanene grown on a semiconductor substrate can represent a paradigmatic example to investigate a direct approach that allows processing the material without the need for transfer, as in the case of solid-state physics applications.
Within this framework, the focal points of this thesis work are:

- studying and optimizing process procedures for handling Xenes;
- to present a possible solution for the stabilization of silicene in environmental conditions;
- exploitation of silicene in possible applications as future perspectives;
- characterization of stanene as a case study of Xene directly grown on a semiconductor substrate.

As shown in Chapter 2, both types of samples are realized through Molecular Beam Epitaxy (MBE), characterized through *in-situ* and *ex-situ* techniques and prepared by means of common cleanroom fabrication techniques. Chapter 3 presents the different types of configurations used and defines the optimized transfer and processing procedures necessary according to the specific purposes.
Then, the following Chapters deal with the results obtained, firstly, in the case of silicene and finally for stanene. One of the main issues to address in silicene respect is the stabilization out of the ultra-high-vacuum system used for its deposition. In-situ encapsulation through capping layer [10] is a partial solution that offers protection against degradation in environmental conditions for ex-situ characterization, but it does not ensure long-term stability when the silicene is stripped off from its native substrate and transferred to the target one. As shown in Chapter 4, interface engineering of silicene-stanene heterostructures may provide a new stabilization scheme in the pre-growth stage with benefits in the processing step.
Moreover, from the perspective of possible applications, in recent years, there has been an increasing interest in the study of 2D material-based bendable systems that may constitute a background for flexible electronics and photonics [77, 12]. In this context, taking advantage of the cleavable native substrate, which is epitaxial Ag(111) on mica, and the effective encapsulation method, silicene and its heterostructures can be promising candidates, as presented in Chapter 5.
Finally, in Chapter 6, the topological properties related to stanene will be discussed, performing different types of characterization carried out in the case of few-layer stanene grown on indium antimonide (InSb)

substrate.

Chapter 2

Xenes synthesis, characterization and processing techniques

The present Chapter provides an overview of the growth method used for the synthesis of Xenes, i.e., through Molecular-Beam Epitaxy (MBE), and of the main available *in-situ* and *ex-situ* characterization techniques. Finally, some basic processing steps are explained, considering the available facilities in the CNR-IMM laboratories in Agrate Brianza.

2.1 Molecular-Beam Epitaxy growth

The MBE technique is one of the physical vapor deposition techniques in which the material to be evaporated is supplied by heating a source of the material itself (solid in this case), in order to have a uniform deposition rate that will form a thin layer on the substrate. Although, for some Xenes, other synthesis routes can be followed, such as liquid exfoliation or vapor transport deposition, epitaxy is still the technique that provides extreme atomic precision, high quality and scalability. It is worth mentioning, in particular, how for this same technique there are three different methods to achieve growth, which are defined as:

- epitaxy by *deposition*: this type of growth is characterized by the condensation of molten material on the substrate, occurring in a self-organizing way. In this case, silicene on silver is the most typical example [78, 79];

- epitaxy by *segregation*: this method, used, for instance, in the case of germanene on silver [80], involves the interdiffusion of the atoms from a substrate, which represents the material reservoir, placed below the growth surface;
- epitaxy by *intercalation*: in this last case, the material is evaporated onto a matrix crystal, which can be either crossed by atoms to form a sheet of material on its surface or reactive to form a crystalline film with a Zintl phase, where the material is placed between two metallic layers. An example is given by silicides, such as $SrSi_2$, realized on silicon substrate [81].

The vacuum conditions play a key role during the entire process, and it is only thanks to these that it is possible to grow high-purity thin films. Growth takes place under ultra-high vacuum (UHV) conditions (i.e. $\sim 10^{-10}$ mbar) and the deposition rates are so low as to allow the growth of stacks of different materials. UHV conditions are continuously monitored through a Residual Gas Analyzer (RGA).
The Xenes samples considered in the present work are realized through epitaxy by deposition, and the following Chapter 3 will discuss the different realized configurations, giving details of the growth parameters employed in each case. Two different types of MBE systems have been used and, in particular, the LAB10 MBE from Scienta-Omicron is used for the growth of silicene and stanene (Figure 2.1a), while the growth of few-layer stanene takes place in the Omicron NanoTechnology GmbH system (Figure 2.1b).
The basic operating principle for both is almost identical, while they differ in terms of *in-situ* surface analysis techniques, which will be shown in the next Section 2.2. The first MBE system basically consists of three interconnected chambers, namely the loading chamber (in yellow in Fig. 2.1a), the preparation chamber (in violet) and the growth chamber (in red), in each of which the position of the sample can be moved by means of high-precision manipulators. In this system, the growth chamber is equipped with an apparatus for Low Energy Electron Diffraction (LEED) and Auger Electron Spectroscopy (AES). Also the second MBE system has three interconnected chambers but, in this case, they correspond to preparation (in red in Fig. 2.1b), analysis (in blue) and Scanning Probe Microscopy (in green) chambers. The preparation chamber holds the MBE evaporators and a Reflection of High-Energy Electron Diffraction (RHEED) apparatus, while the analysis chamber is equipped with X-ray Photoelectron Spectroscopy (XPS) system. The last chamber, on the other hand, is dedicated exclusively to the Scanning Probe Microscope (SPM) techniques.

Generally, before growth, the preparation of the substrate surface takes place through several cycles of sputtering with Ar^+ ions and high temperatures annealing. After this step, the actual growth occurs: the basic principle is always the heating of the material inside a crucible but, according to the type of material, different evaporation mechanisms can be used, such as Knudsen-cells (which are effusion cells), electron bombardment or sublimation. The evaporation rate is carefully controlled by changing the growth parameters and it is calibrated through a quartz microbalance.

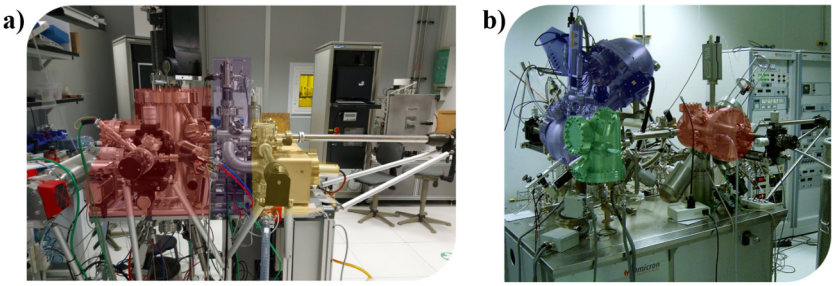

Figure 2.1: *Images of the two MBE systems.* ***(a)*** *Image of ScientaOmicron LAB10 MBE system, where the loading chamber, the preparation chamber and the growth chamber are highlighted in yellow, violet and red respectively.* ***(b)*** *Image of Omicron NanoTechnology GmbH MBE system, where preparation (growth), analysis and SPM chambers are highlighted in red, blue and green, respectively.*

2.2 In-situ characterizations

Although the two MBE systems are equipped with instruments for different *in-situ* characterizations, only the main techniques used for the samples under consideration will be actually discussed, specifically XPS and LEED techniques.

2.2.1 X-ray Photoelectron Spectroscopy

XPS is a surface analysis technique widely used in several fields. The operation principle is based on X-ray irradiation of the sample and the consecutive collection of electrons emitted from the core levels of the material by the photoelectric effect, as shown in Figure 2.2. The X-ray photon incident on the surface of the sample ionizes the core electrons of the atom of the material, which then, after interacting with the surrounding system, escape with a certain kinetic energy E_k. During their path toward the surface, the electrons lose a part of their energy due

to inelastic scattering interaction within the material, and only a portion of them will reach the detector. This mechanism limits the escape depth to a few nanometers below the sample surface making XPS a surface-sensitive technique, as only photoelectrons close to the surface will have enough residual energy to be emitted.
According to the Beer-Lambert law, the XPS sampling depth l can be estimated as:

$$l \sim 3\lambda(E)\cos\theta \tag{2.1}$$

where $\lambda(E)$ is the inelastic mean free path of the electrons of energy E and θ is the take-off angle (TOA) measured from the sample plane. By varying the TOA at which the electrons are detected from the surface, for example by tilting the sample, it is possible to enhance the surface contribution, which can play a major role in the 2D materials characterization. In particular, one can identify a surface-sensitive condition, characterized by relatively small values of TOA, and a bulk-sensitive condition, realized with TOA values closer to the right angle.
It has to be noted, that after the photoelectrons emission, the system presents a hole in the core energy level of the atom, hence, the kinetic energy of the emitted photoelectrons is also determined by the interaction between the system and the potential created by the core hole. However, by assuming this interaction as instantaneous (sudden-approximation), the kinetic energy can be expressed as:

$$E_k = h\nu - |E_B| - \Phi_{spec.} \tag{2.2}$$

where $h\nu$ is the energy of the incident photon, E_B is the binding energy of the core level, conventionally expressed as a positive quantity (typically referred to the Fermi level E_F) and $\Phi_{spec.}$ is the spectrometer workfunction. Hence, by measuring the kinetic energies, one can directly derive the binding energies.
A typical XPS spectrum represents the intensity (as counts per second) as a function of the binding energy of the emitted core electrons and, by identifying the peak positions, information on the material can be obtained. The electrons collected, in fact, possess information about the electronic structure and chemical state, characteristics that make it possible to detect each element and identify both different atomic species in chemical compounds and the chemical bond type between them.
XPS spectra typically consist of several peaks with different shape and intensity, often overlapping each other, related to numerous physical phenomena that take place in the analyzed sample. Generally, the oxidized component of an element appears as a higher binding energy

contribution often relatively close to the the core-level peak. Hence, for example, XPS can be used to determine the chemical state of a Xene that has just been freshly grown but also after being processed. Specifically, in this work, XPS has been used to identify Xenes degradation or interaction with the substrate in terms of a change in the chemical state against a change in the shape profile of the core-level line.

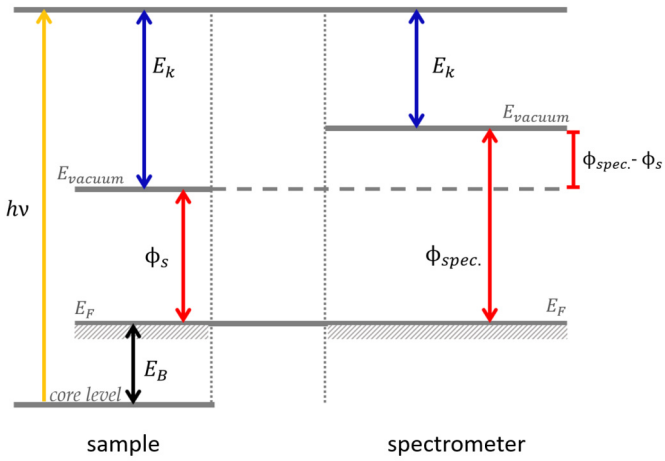

Figure 2.2: *Energy level schematization illustrating the XPS binding energy measurement. It should be noted that the kinetic energy in the spectrometer is different due to a different workfunction compared to the sample.*

2.2.2 Low-Energy Electron Diffraction

The LEED technique is useful in analyzing surface crystallography, allowing the determination of atomic positions at crystalline surfaces. It is based on the diffraction by a crystal lattice of electrons which, impacting on a fluorescent screen, create light patterns reproducing the reciprocal lattice of the unit cell through which the symmetry and periodicity of the material grown can be determined. A typical LEED characterization experiment is shown in Figure 2.3a.
An electron beam with energies in the range of 20-300 eV impinges perpendicularly on the surface of the sample. The electrons are backscattered passing through a system of grids placed before a hemispherical fluorescent screen. The backscattered electrons will be either elastically or inelastically diffracted. Thanks to the retarding grids, only the elastically diffracted electrons will be accelerated toward the screen and detected, creating a bright spots pattern which corresponds to a

representation in the reciprocal space.
In terms of the physical underlying mechanisms [82], in a two-dimensional system, if one defines in the real space the primitive translational vectors as **a** and **b**, and a unit vector **n** normal to the surface then, in the reciprocal space, it is possible to express the primitive reciprocal lattice vectors as:

$$a^* = 2\pi \frac{\mathbf{b} \times \mathbf{n}}{\mathbf{a} \times \mathbf{b} \cdot \mathbf{n}} \tag{2.3}$$

$$b^* = 2\pi \frac{\mathbf{n} \times \mathbf{a}}{\mathbf{a} \times \mathbf{b} \cdot \mathbf{n}}. \tag{2.4}$$

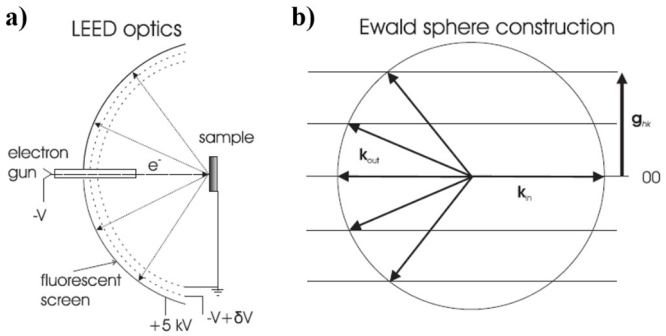

Figure 2.3: ***(a)*** *Schematization of a LEED experiment.* ***(b)*** *The corresponding Ewald sphere construction. Taken from Ref. [83].*

If the incoming and outgoing wavevectors parallel to the surface are respectively named as $\mathbf{k}_{in\parallel}$ and $\mathbf{k}_{out\parallel}$, in addition to the condition of energy conservation for the elastic scattering, which translates into $|\mathbf{k}_{in}| = |\mathbf{k}_{out}|$, in order to obtain the diffraction pattern, it is necessary to satisfy the constructive interference condition given by:

$$\mathbf{k}_{out\parallel} = \mathbf{k}_{in\parallel} + \mathbf{G}_{hk} \tag{2.5}$$

where h, k are integers and $\mathbf{G}_{hk}$ is any of the reciprocal lattice vectors defined as:

$$\mathbf{G}_{hk} = h\mathbf{a}^* + k\mathbf{b}^*. \tag{2.6}$$

This condition can be visualized through the construction of Ewald's sphere [84], shown in Figure 2.3b, noticing that, instead of reciprocal lattice points, there are reciprocal lattice *rods* perpendicular to the surface. In this way, the condition expressed in 2.5, is satisfied whenever the wave vector $\mathbf{k}_{out}$ terminates at the intersection of the sphere and a rod.
As shown in Chapter 3, in this work the LEED technique has been used

to characterize the substrate before the growth and to understand the crystal structure of the Xene layer, for example, in order to identify the silicene reconstructions, such as those shown in Figure 1.4c.

2.3 Raman Spectroscopy

Raman spectroscopy is a well-known and powerful non-destructive technique that can be used in various fields to characterize and identify different materials. In general, when light interacts with matter, scattering processes [85] can occur and, depending on the wavelength of the scattered light, can be classified as elastic or inelastic. In the former case, the frequency of the scattered light is the same as the incident radiation (Rayleigh scattering), while in the latter case, it is different and the process is called Raman scattering, as shown in Fig. 2.4. Since the two frequencies are different, it means that after the interaction, the outgoing photons may be more likely to have a lower energy (i.e., Stokes Raman scattering) or, in minor cases, a higher one (i.e., anti-Stokes Raman scattering).

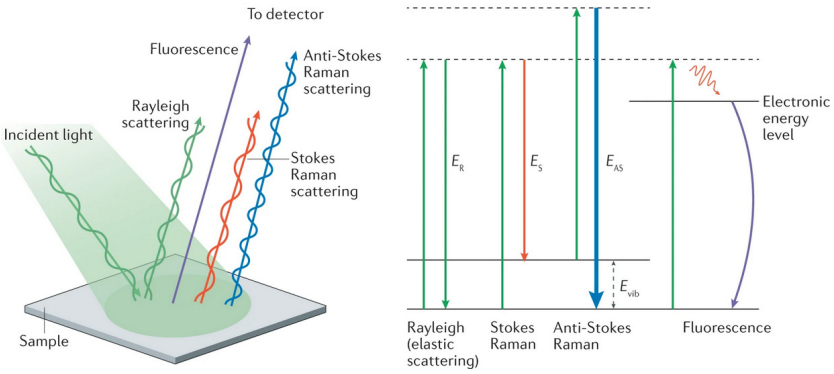

Figure 2.4: *Schematization of elastic and inelastic scattering processes of light incident on a material. Ref [86].*

There is, therefore, an energy transfer associated with vibrational or rotational transitions of the material, that is related to a change of polarizability α, which provides valuable information about the material properties.
Using a quantum approach [87, 88], the energy transfer caused by the incident radiation **E** can be associated with a transition between discrete energy levels that will be described by a wave function of the initial state ψ_i and one of the final state ψ_f. It can be therefore defined a transition

moment given by:

$$\mu_{fi}^{(1)} = \langle \psi_f | \alpha | \psi_i \rangle \cdot \mathbf{E} \tag{2.7}$$

where α indicates the polarizability tensor, whose matrix element, is expressed as:

$$[\alpha_{xy}]_{fi} = \langle \Phi_f | \alpha_{xy} | \Phi_i \rangle \,. \tag{2.8}$$

In this case, the rotational part is ignored, hence Φ is the vibrational wavefunction and, in the case of the harmonic oscillator model, it can be expressed as: $\Phi_n = \prod_k \Phi_{v_k^n}(Q_k)$ where v_k^n is the vibrational quantum number of a certain state n. Hence, considering the first-order approximation, it can be obtained:

$$[\alpha_{xy}]_{fi} = (\alpha_{xy})_0 \langle \Phi_f | \Phi_i \rangle + \sum_k \left(\frac{\partial \alpha_{xy}}{\partial Q_k} \right)_0 \langle \Phi_f | Q_k | \Phi_i \rangle \tag{2.9}$$

where $(\alpha_{xy})_0$ is the value at the equilibrium configuration and Q_k are the nuclear coordinates expressed in normal coordinates of vibrations. In this equation, the first term expresses the Rayleigh scattering and it is non-zero only if the quantum numbers of the initial and final state are equal, while the second term is related to the Raman scattering. Thus, it is possible to state that a vibrational mode is Raman active if at least one element of the $\frac{\partial \alpha_{xy}}{\partial Q_k}$ tensor is non-zero, and in particular, in the harmonic approximation, the vibrational quantum number must change according to $\Delta v_k = \pm 1$, i.e., $\Delta v_k = 1$ for Stokes Raman scattering and $\Delta v_k = -1$ for the anti-Stokes Raman scattering. More generally, however, it is possible to identify selection rules governing the Raman scattering which are a consequence of symmetry requirements that can be derived from group theory: a transition between an initial state ψ_i and a final state ψ_f is only permitted if at least one element of the triple product $\psi_i \alpha_{xy} \psi_f$ belongs to a representation whose structure contains the totally symmetric species. In general, the Raman scattering phenomenon is related to the degree of crystallinity of the materials, showing sharp and intense peaks in the case of crystalline materials, and resulting in broader and less intense peaks in the case of amorphous materials. Moreover, apart from materials that are Raman inactive due to strictly symmetry-related issues, if the material surface is characterized by the presence of many free electrons, as in the case of metals, the laser light penetration can be limited, resulting in a weak or even undetectable scattered signal (Raman silent mode).

In the present work, Raman spectroscopy has been used for different purposes, such as, for characterizing Xenes crystal quality after the growth,

as a material control test after specific processing steps or as a probe to quantify the level of stress/strain applied to the sample. Typically, the basic apparatus for performing Raman spectroscopy consists of a laser source that induces Raman scattering, a system for collecting the scattered radiation, usually in backscattering configuration, a spectrometer and a Charge Coupled Device (CCD) detector. A notch or edge filter is usually used to eliminate the Rayleigh and anti-Stokes radiation so that only the component of the Stokes scattered light is measured.
Lasers of different wavelengths can be used as sources, ranging from 500 nm to 1000 nm, but it should be noted that decreasing the wavelength increases the likelihood of fluorescence phenomena [89], as it will be treated in Chapter 3.
In this work, the Raman measurements are performed using a single monochromator Renishaw InVia spectrometer in a backscattering configuration with a continuous-wave 514 nm excitation coupled to a Leica optical microscope equipped with different objectives and a motorized translation stage which allows to obtaining micrometric spatial resolution.

2.4 Fabrication process

When the growth of the sample is completed and it is brought out of the UHV conditions of MBE, depending on the type of characterization or test to be performed, it is typically necessary to employ standard fabrication processes, e.g., to make electrical contacts or to define a specific geometrical structure. The two most commonly used fabrication steps are explained below, while the next Chapter 3 will discuss in detail how these techniques have been used in the device realization procedures which have been tested and optimized.

2.4.1 Lithography technique

In general, lithography is a common technique through which it is possible to print a pattern on a sample by exposing with electrons or photons a polymer, called resist, which has been previously spin-coated on the substrate. The effect of the exposure is to change the solubility of the resist in a development solution with respect to the unexposed resist. If the solubility is increased the resist is said to be positive, instead if it decreases, the resist is said to be negative. After the development, the result is a resist mask that can be used to perform chemical etching or to evaporate metals. In the end, by removing the remaining resist, it is possible to achieve the desired pattern. A scheme of this process is described in Figure 2.5.
The main steps for any kind of lithographic process are:

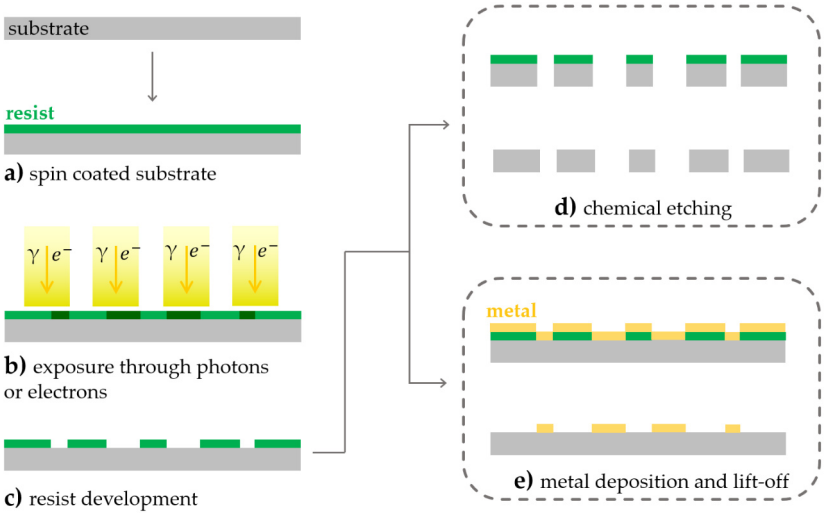

Figure 2.5: *Schematic description of the lithographic process (electron beam and optical) and the typical two possible next steps, i.e., etching or metal deposition.*

- cleaning: at the beginning of the process, the surface of the sample has to be prepared by means of a pre-bake or by oxygen plasma cleaning;
- spin-coating: the sample surface is covered with the resist, spinning the sample on itself so as to obtain a thin uniform resist layer (Fig. 2.5a);
- baking: the sample has to be backed on the hotplate in order to completely dry the resist layer;
- exposure: the desired pattern is printed on the sample surface (this step depends on the technology used but, in the most common cases, the sample is irradiated with photons or electrons, see Fig. 2.5b);
- development: by immersing the sample in a specific acid solution (i.e., the developer), the exposed (in case of positive resist) or unexposed (negative resist) regions are removed (Fig. 2.5c);
- processing step: at this point, the two most common steps following a lithographic process are chemical etching of the material (Fig. 2.5d) or metal deposition (Fig. 2.5e);
- resist removal: at the end, the resist left on the surface of the sample

is removed by soaking in acetone.

In this work, the optical lithographies have been mainly performed with Tabletop Maskless Aligner μMLA manufactured by Heidelberg Instruments Mikrotechnik GmbH. It uses a LED with a wavelength of 390 nm as source and the drawn pattern is directly exposed with a 2D spatial light modulator (SLM). During the exposure, the sample is moved by a motion stage under the optical unit, which projects the pattern to be exposed onto the wafer surface.
However, some of the initial samples, i.e. the oldest ones, have been lithographed through the Mask Aligner MJB4 manufactured by SUSS MicroTec. The operating principle is the same, but in this case, the pattern is not directly printed, but a transparent chrome photomask has to be used. The chrome layer reproduces the desired pattern and, in this way, the UV light directed towards the sample will only be transmitted through metal-free regions, reproducing the pattern of the mask on the sample surface.
Regardless of the employed technology, also for optical lithography, it is possible to define the dose concept expressed in mJ/cm^2. Compared to other types of lithography techniques such as Electron Beam Lithography (EBL), the advantages of this technology are the speed of the process in the case of extended patterns, the absence of problems in the case of insulating substrates and the overview camera through which it is possible to inspect the sample before exposure.
As resist it is used AZ5214 reversal photoresist which, according to the final goal, can be either positive or negative. Indeed, depending on the upcoming process to be carried out, it should be emphasized that it becomes fundamental to choose the correct type of resist. In fact, the underlying chemical process is different and can affect the resist profile: even if the desired result should be a resist with a vertical profile in order to achieve the best pattern fidelity, it is actually relatively difficult to obtain it.
In the case of a positive process, after development, the resist profile has typically a positive slope (namely overcut profile, visible in an extreme version in Figure 2.6a) caused by an attenuation that light undergoes when penetrating the resist layer, which then results in a higher dissolution rate at the top and lower dissolution rate at the bottom of the resist. Generally, this process is the one selected in case the sample needs subsequent chemical etching.
Conversely, in the case of a negative tone, the most exposed regions, i.e., those at the top, will be crosslinked at higher temperatures with respect to those at the bottom, which will then have a higher dissolution

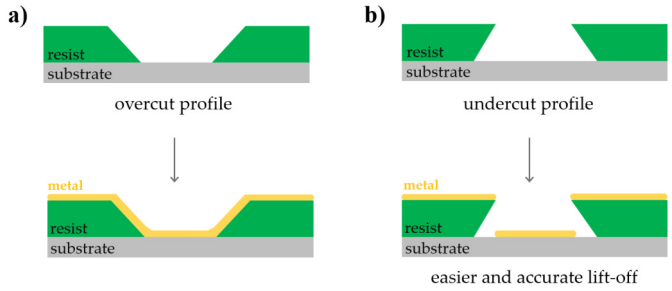

Figure 2.6: *Different photoresist profiles.* ***(a)*** *Overcut profile typical of a positive-tone photoresist and* ***(b)*** *undercut profile generally associated with a negative one. The latter is more suitable for the lift-off process.*

rate. This produces a profile with a negative slope (namely, undercut profile, see Figure 2.6b), which is ideal in the case of lift-off after metal deposition (process described below).
The two types of tones also differ in process conditions. In the case of positive resist the steps are the following:

- cleaning and dehydration of the sample carried out by acetone and isopropanol and subsequent heating by the hot plate at 120 ^{o}C for 4 minutes;
- spin-coating of the resist on the surface at a speed of 6000 rpm for 30 seconds;
- tempering of the resist through the hot plate at 90 ^{o}C for 1 minute;
- exposure of the sample according to the desired pattern;
- development of lithography by developer AZ400K for $\sim$ 40 seconds;
- if the sample has to undergo chemical attack by wet etching, then a step of resist hard bake through hot plate at 120 ^{o}C for 3 minutes is necessary in order to harden and make the resist durable.

On the other hand, to obtain a resist with a negative tone, the process steps after the resist spin-coating are slightly different and in particular:

- the resist tempering, in this case, is performed on the hot plate at 110 ^{o}C for 1 minute;
- exposure of the sample according to the desired pattern;
- reversal bake of resist on the hot plate at 110 ^{o}C for 1 minute;

- flood exposure with a higher dose value (two or three times higher than the initial) for converting the unexposed areas into a developable form;
- development of lithography by developer AZ400K for $\sim$ 40 seconds.

2.4.2 Metal deposition and lift-off

The metal deposition is realized using the electron-beam evaporation system Auto 304 from Edwards. In this process, the sample is mounted on a sample holder in the vacuum chamber of the evaporator. The material to be evaporated is put in a crucible and, when the pressure inside the chamber is sufficiently low ($\sim 10^{-6}$ mbar), it is heated through the electron beam and it is deposited on the sample surface until the desired thickness is reached. When the metal evaporates its deposition rate is measured by a quartz microbalance which can monitor rates of the order of $\sim$ nm/s.
This procedure is repeated also for the other metals to be deposited. Depending on the type of material and the measurement to be performed, different metals can be used; in this work, the pads are realized by first depositing an adhesion layer of titanium of $\sim$ 5 nm followed by a gold layer of $\sim$ 50 nm. The following step is the lift-off of the metal. This procedure consists of immersing the sample in a becher full of acetone in order to dissolve the resist mask, thus leaving only the metal pattern corresponding to what has been previously lithographed. The sample is immersed in acetone for a time sufficient to easily remove all metal in excess by spraying acetone with a syringe on the surface. Finally, the sample is rinsed with isopropanol and dried with nitrogen gas.

Chapter 3

Xenes configurations enabling device fabrication procedures

The purpose of this Chapter is to present the different types of investigated samples and explain the relative processing procedures that have been studied and optimized. The first part is concerned with silicene samples, while the second one is related to the case of few-layer stanene.

3.1 Silicene and its heterostructures samples

The first samples to be presented are the silicene samples. In this case, the substrate used is the commercial Ag(111)-on-mica substrate, supplied by Mateck. The mica layer has a thickness of 300 µm, while the Ag film is 300 nm thick. The silicene samples are grown in the Scienta Omicron LAB10 MBE system described in Sec. 2.1.
Two types of sample configurations have been studied: silicene samples grown directly on Ag(111), as shown in Fig. 3.1a, and silicene-stanene heterostructures, where the stanene layer grown on Ag(111) is used as a template for silicene growth, as reported in Fig. 3.1b. In both cases, the silicene can be monolayer or multilayer. The general steps for realizing the samples can be summarized as follows:

- substrate preparation: the Ag(111)-on-mica substrate is prepared through several cycles of sputtering and annealing;
- growth of silicene samples (Fig. 3.1a): the silicene is directly grown

on top of the silver layer, increasing the deposition time for the multilayer growth;

- growth of heterostructure samples (Fig. 3.1b): the stanene is deposited on top of the silver layer and subsequently, the silicene is grown on top of tin;
- encapsulation: the samples are protected through *in-situ* sequential deposition of the capping layer.

Before the growth, the substrate preparation takes place through several cycles of sputtering (through Ar^+ ions bombardment) and annealing at high temperature ($\sim$ 550 ^{o}C), in order to clean the substrate surface from organic contaminants and restore the crystalline periodicity.

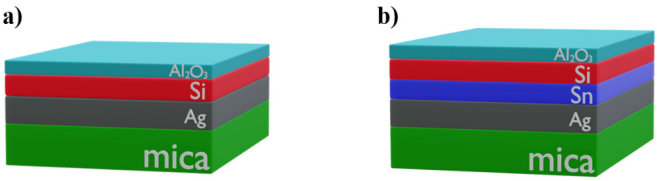

Figure 3.1: *Two configurations of the investigated samples.* ***(a)*** *Silicene samples structure and* ***(b)*** *silicene-stanene heterostructure samples. Representation not to scale.*

Subsequently, depending on the type of sample to be realized, Xenes growth is carried out by carefully controlling the temperature and deposition time, keeping the substrate at 200–225 ^{o}C. After both the substrate preparation and the growth of each Xene layer, the LEED pattern is acquired in order to characterize the crystal structure of the surfaces. The LEED patterns obtained are shown in Figure 3.2.
The first row of the Figure is referred to the case of Ag(111) as substrate and, in particular: panel (a) shows the pattern of the prepared Ag:1$\times$1 substrate showing the hexagonal symmetry, panel (b) reports the case of monolayer silicene with mixed phases [64] (4$\times$4 and $\sqrt{13} \times \sqrt{13}$ R13.9^o), while panel (c) shows the pattern for the multilayer silicene, characterized by a $\sqrt{3} \times \sqrt{3}$ R30^o termination [90].
The second row, instead, refers to the case where the stanene on Ag(111) is used as growth template and, in particular: panel (d) shows the result obtained for the stanene, with a $\sqrt{3} \times \sqrt{3}$ R30^o reconstruction on the Ag(111) [71], while panels (e) and (f) are respectively showing the monolayer and multilayer silicene grown on top the stanene, both char-

acterized by a $\sqrt{3} \times \sqrt{3}$ R30º superstructure.
After growth, the samples are protected against degradation by encapsulation, carried out through *in-situ* sequential deposition of a 5 nm thick Al_2O_3 capping layer, by means of reactive molecular beam deposition [10]. The presence of the Al_2O_3 layer on top allows the sample to be taken out of the MBE without damaging it, but at the same time, still allows optical characterizations, such as Raman spectroscopy.

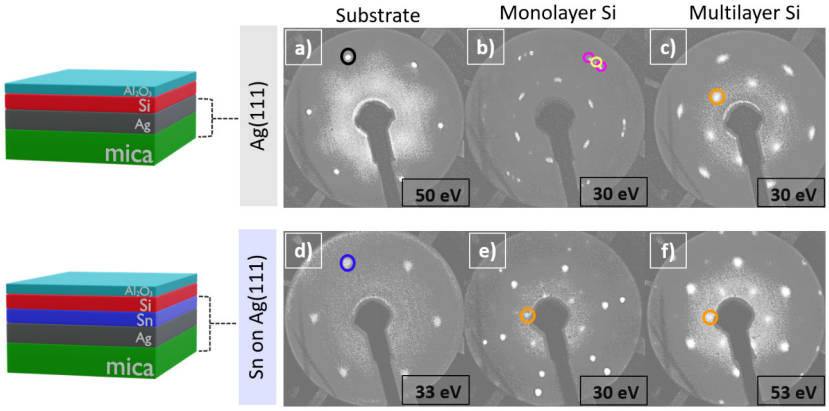

Figure 3.2: *In-situ LEED characterization with the respective incidence energies. Pattern obtained for* ***(a)*** *Ag:1×1 substrate (black circle),* ***(b)*** *Pattern obtained for monolayer Si on Ag(111), where the yellow and violet circles are mixed silicene phases (4×4 and* $\sqrt{13} \times \sqrt{13}$ *R13.9º respectively),* ***(c)*** *multilayer Si, grown on Ag(111), with* $\sqrt{3} \times \sqrt{3}$ *R30º termination (orange circle),* ***(d)*** *Sn:*$\sqrt{3} \times \sqrt{3}$ *R30º (blue circle) on Ag(111),****(e)*** *monolayer Si on Sn and* ***(f)*** *multilayer Si on Sn, both with phase* $\sqrt{3} \times \sqrt{3}$ *R30º (orange circles).*

3.1.1 Raman characterization

The Raman technique is one of the most useful tools for characterizing *ex-situ* the samples immediately after growth and encapsulation in the MBE. In Figure 3.3 the top and bottom views of the sample surface are shown together with the respective Raman characterization. Typically, the samples have a size of about 1 cm^2, but the growth of the material takes place only in the region highlighted in red in Fig. 3.3, since the samples are fixed to the sample holder by clamps (corresponding to the region highlighted in black).
The Ag(111) layer has no Raman active modes (Fig. 3.3a), while mica substrate, on the contrary, due to its chemical composition, has several

Raman modes (Fig. 3.3c) characterized by complicated symmetries [91]. As will be explained in Subsection 3.1.2, these two spectra are of high importance during processing techniques because they can provide a reference during sample delamination and transfer, but also in the etching processes case.

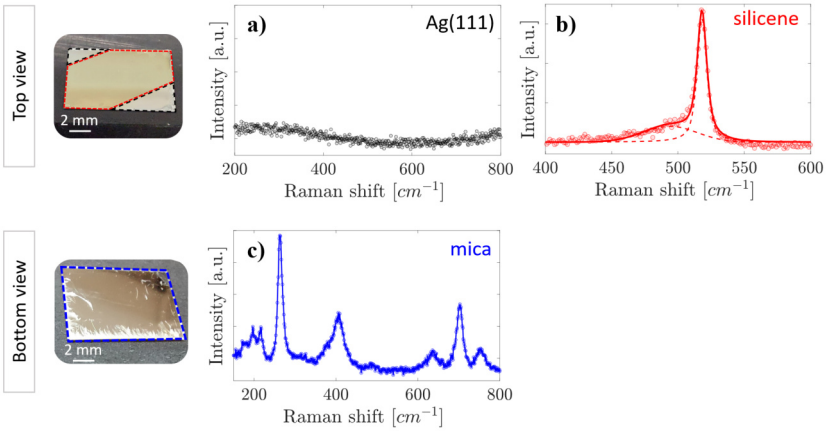

Figure 3.3: *Optical images of the top and bottom view of the sample with the respective Raman characterization. In the top view, the silicene growth region and the Ag(111) substrate areas are respectively highlighted in red and black, while the bottom view shows the mica layer (highlighted in blue).* ***(a)*** *Raman spectrum of Ag(111).* ***(b)*** *Fitted Raman spectrum of silicene, where the raw data are the scattered points, the solid curve is the corresponding fit result, and the two dashed curves show the two components used in the fitting procedure.* ***(c)*** *Raman spectrum of mica.*

The Raman spectrum of silicene (Fig. 3.3b) is generally characterized by the main E_{2g} peak, related to the symmetric stretching of Si-Si atoms in planar hexagons and, depending on the specific silicene superstructure, by minor components, at lower frequencies, of A_{1g} and B_{2u} symmetry [42, 66]. In particular, the former is related to the intrinsic disorder related to the non-uniform buckling, while the latter one is associated with Kekule-distorted hexagonal rings, that together give rise to the characteristic asymmetrical shoulder around 450-500 cm^{-1}. Also the E_{2g} mode wavenumber is phase-dependent and it is located at 516 cm^{-1} for the mixed phase including 4×4 and $\sqrt{13}\times\sqrt{13}$ superstructures, or at 521 cm^{-1} for the $2\sqrt{3}\times2\sqrt{3}$ superstructure. Furthermore, it should be mentioned that the first order Raman mode also depends on the specific sample configuration: in the case of multilayer silicene samples, due to

shorter Si-Si bond length [92], it is characterized by a frequency blue-shift, compared to the monolayer case, which results in a peak around 522-525 cm^{-1}. In order to perform the Raman analysis, the spectra are fitted with two Voigt function components, through the WiRE (Windows-based Raman Environment) software by Renishaw Ltd.

3.1.2 Transfer processes

After the realization of the sample, different types of processes have been examined to investigate the properties of silicene or to integrate it into some prototypical devices. One of the first processes tested is based on the cleavable nature of mica which allows, through mechanical delamination, to obtain a cm^2 scale bendable sample that is sufficiently deformable to study the effects of an applied strain on silicene.
As discussed in more detail in Chapter 5, flexible samples can be realized starting from mono and multilayer silicene and silicene-stanene heterostructures epitaxially supported by Ag(111) substrates and will be referred to as bendable silicene membranes. The fabrication steps of the bendable silicene membranes are summarized in Figure 3.4.

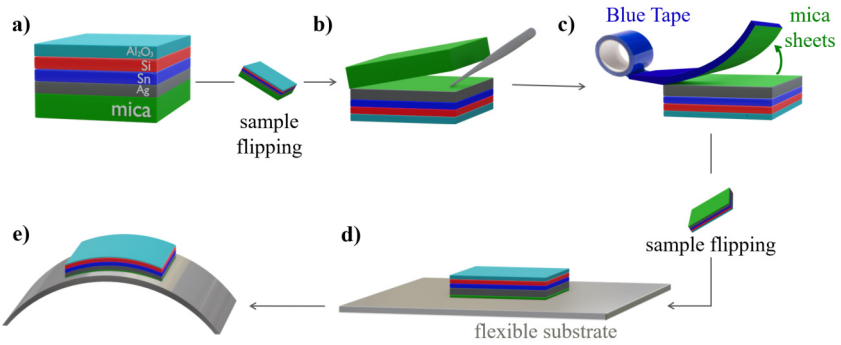

Figure 3.4: *Schematization of the processing steps used for fabricating the Xenes-based membranes.* ***(a)*** *After the Xenes growth and the deposition of the Al_2O_3 capping layer, the sample is flipped for mica delamination with* ***(b)*** *tweezers and* ***(c)*** *blue Nitto tape.* ***(d)*** *The sample is then flipped back and attached on a flexible substrate* ***(e)*** *allowing characterization of the properties of the bendable membranes under mechanical deformation.*

From top to bottom, the starting sample configuration (Figure 3.4a) includes Al_2O_3 capping layer, active Xenes layers (being silicene or silicene-stanene), and the Ag(111)/mica substrate as a template. The process starts by flipping back the whole stack and mechanically removing a bulk part of the native mica substrate (Figure 3.4b). Then, the delamination is further refined by means of multiple scotch-tape (3M^{TM}

Blue Nitto tape) peelings, thus leaving only some residual layers of mica (Figure 3.4c). Subsequently, the sample can be turned upside down and attached to a secondary host-substrate, namely a flexible polymer substrate, using a double-sided tape (Figure 3.4d-e).
In the present case, the polymer used as carrier substrate is a commercial polyethylene terephthalate (PET) sheet which has been preferably chosen for its good thermal and chemical stability [93, 94]. Anyway, thanks to the chemical and structural stability of the Xenes layers in the heterostructure, this transfer process is universally applicable to any other kind of flexible substrates like amorphous (polycarbonate), semi-crystalline thermoplastic polymers (polypropylene) or bio-compatible and -resorbable materials (cellulose, collagen, silk fibroin) [12, 95, 96, 97]. In the time scale required to perform the lithography and lift-off processes, the PET sheet is resistant to both temperature and the solvents used, such as acetone and AZ400K developer. As a demonstration, a test pattern has been lithographed directly on PET substrate, as shown in Figure 3.5.

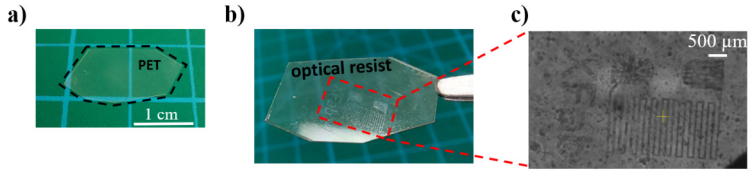

Figure 3.5: ***(a)*** *Optical image of the defined PET substrate used for the process.* ***(b)*** *Optical picture of the PET substrate after the optical resist spin-coating, lithography execution and subsequent development in diluted acid solution.* ***(c)*** *Optical image of the realized pattern (a microheater with the XFab project logo) acquired through the optical microscope.*

A second type of examined process aims to exploit the Ag(111) layer to electrically contact the Xene layer. To do this, the samples are flipped upside down and attached, through an adhesive layer, to a target substrate, for example, a metal plate (Figure 3.6a). Mica is stripped off with the help of a tweezer (Figure 3.6b) and the remaining residues are cleaned up further through a stick and take-off procedure by using the 3M^{TM} blue Nitto tape (Figure 3.6c). This step is repeated until the mica removal is confirmed by close inspection through Raman spectroscopy monitoring, as shown in Figure 3.7. After complete removal of the mica residues (Figure 3.6d), the Ag can be selectively etched (Figure 3.6e) with an optimized *home-made* solution (see Subsection 3.1.3). At this point, the Ag layer can either be entirely etched off or patterned so as to realize

electrical contacts through isolation trenches made of Ag itself.
Although this is a method that has already been demonstrated and presented in several cases [98, 99], it must be emphasized that it does not represent a scalable process leading, for example, to a serial definition of silicene devices.
The most challenging problem of this procedure is the detachment of the mica from silver, which typically results in a very rough and disconnected surface of the latter, and severely limits the subsequent lithographic process, as shown in Figure 3.8a-d.

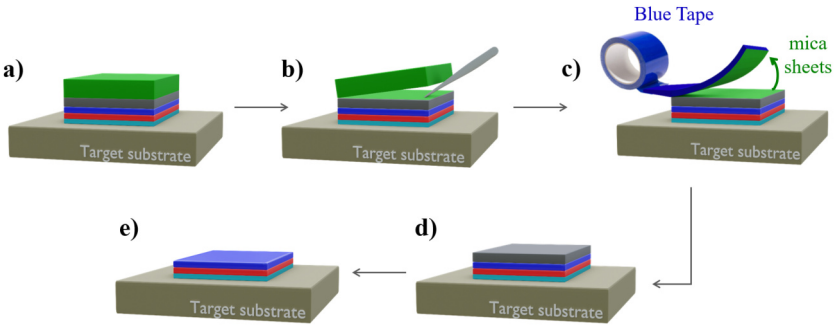

Figure 3.6: *Schematic representation of the process used for transfer and delamination of the sample.* ***(a)*** *The sample is attached face-down to the target substrate, for example, a metal plate.* ***(b)*** *A thick layer of mica is removed by using a tweezer.* ***(c)*** *Mechanical delamination of residual mica sheets is performed with 3M^{TM} Blue Nitto tape.* ***(d)*** *Sample completely free of mica leaves exposed the Ag layer.* ***(e)*** *After the chemical etching of the Ag layer, the process is completed.*

It is for this reason that a significant part of this thesis work was focused on optimizing this delamination and transfer process, in order to obtain a better and more uniform Ag surface which would allow the entire process to be integrated into a scalable patterning scheme. In particular, I defined and optimized a new process based on three steps of lithography that can improve the final result and enable future advances in the realization of Xene-based devices.
Typically, the fabrication of an operating Field-Effect Transistor (FET) is a common test bench for the validation of any device integration scheme that aims to assess the electrical properties of 2D materials. Hence, in the following, it can be taken as an example the implementation of a back-gate transistor device configuration, with a basic structure represented by two source and drain pads and a channel region composed of

the Xene layer.
The problem underlying the previous method is based on the strong adhesion present between the thick layer of mica and the Ag(111) grown on it.
In contrast to the case of Au(111) deposited on mica, in which it is possible to detach the two materials by simple immersion in water, in the case of silver, there are no chemical solvents that can weaken the adhesion bond and promote the complete detachment. This inevitably complicates the process in the case of our samples because, by performing mechanical delamination, a large amount of strain is released into the sample stack, in a random and uncontrollable way, making the Ag surface strongly roughened (see Figure 3.8a and Appendix Afor further details).

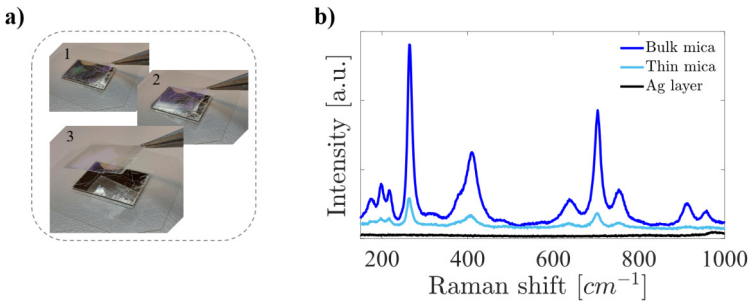

Figure 3.7: ***(a)*** *Pictures of the mechanical delamination process of mica.* ***(b)*** *Raman spectra acquired during mica delamination. The blue line refers to the acquisition before the delamination, i.e., on bulk mica. The light blue spectrum relates to the acquisition after several tape peelings of mica substrate. The black line confirms that the mica residues have been completely removed and, therefore, corresponds to the (Raman-silent) Ag(111) spectrum.*

This surface dramatically hurdles the lithography process and, above all, affects the subsequent Ag etching step: in Figures 3.8b-d some of the attempts to etch silver are shown, where the etching turns out to be random or partially effective. In particular, this is the case of the first two examples shown in Figures 3.8b and c, whereas in the third case of Fig. 3.8d, it can be seen the process correctly completed.
The steps of the optimized method are shown in Figure 3.9. To favour the total detachment of the mica layer, it is necessary to decrease the level of in-plane strain by pre-defining the desired structures and isolating them from each other by etching both the Xenes and the Ag layer into

the surrounding regions (see Figure 3.9a-b).
Subsequently, a second aligned lithography step of the negative previous pattern is performed (Fig. 3.9c), so that the following adhesive layer is only present in contact with the sample regions (Fig. 3.9d). In this way, in the remaining regions, the mechanical mica delamination will be favoured, thus resulting in structures with a sufficiently smooth and clean Ag surface (Fig. 3.9e) to be patterned.
The last aligned lithography step (Fig. 3.9f) is used to define the active regions of the device, which therefore must be Ag-free; in the case in example, this step corresponds to defining multiple transistors. Selectively etching the silver results in the final realization of the sample, which is ready to be electrically characterized (Fig. 3.9g).

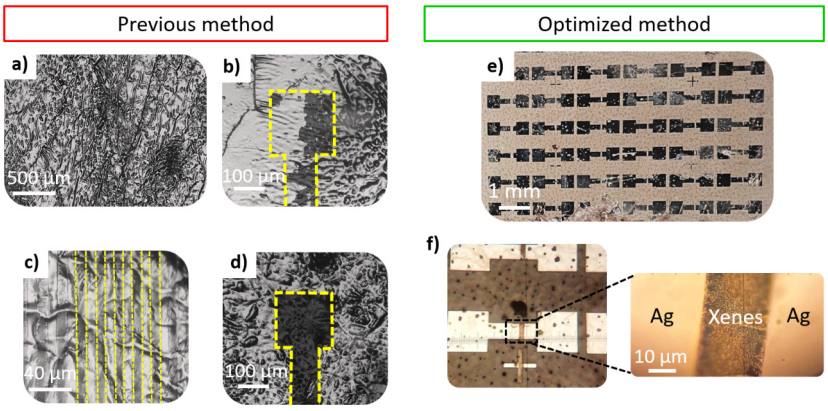

Figure 3.8: *Comparison of the previous method with the new optimized method.* ***(a)*** *Optical image of Ag rough surface after mica delamination.* ***(b-d)*** *Optical images of Ag etching attempts in the case of the contact pad and stripes structures (highlighted in yellow). Only in the last case* ***(d)*** *the Ag etching is successfully completed.* ***(e)*** *Optical image of the completed sample surface after the new optimized processing scheme.* ***(f)*** *Zoomed image of one of the realized structures, where it is possible to see the channel region where the Ag has been etched, leaving the underlying Xene.*

As can be seen in Figure 3.8e-f, the silver surface is more homogeneous, and it is possible to make several devices in series on a single sample, thus demonstrating the scalability of the new process.
The success of the new method is based mostly on the second lithography step, which allows the adhesive layer to be deposited only in correspondence with the pre-defined structures and thus avoiding the

surrounding regions. To demonstrate this, several preliminary tests have been carried out by repeating the process by performing or avoiding the second lithography step. The results are shown in Figure 3.10a-d.
In particular, in the panel on the left, it can be clearly seen how few parts of the sample survive after the mechanical delamination of mica, and the silver layer remaining is heavily wrinkled. On the right, however, it can be noticed how the process including the second lithography step allows for a higher yield and a more homogenous surface.
Furthermore, in Fig. 3.10e, Raman probing at the specific colored points highlighted in Fig. 3.10d is reported.

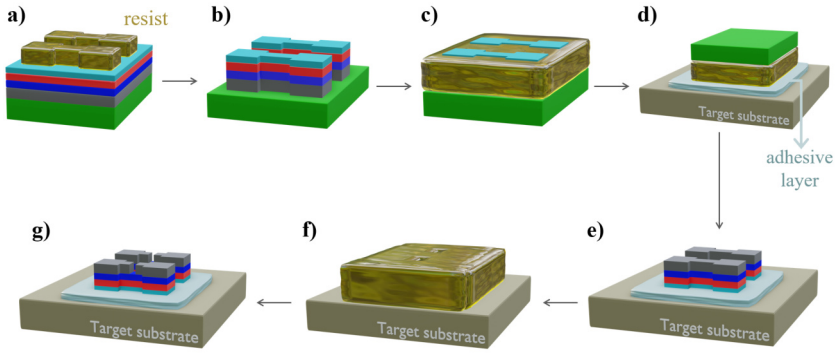

Figure 3.9: *Schematic representation of the new optimized processing scheme for device realization.* ***(a)*** *The first lithography step is to define individual structures.* ***(b)*** *Etching of the Al_2O_3-Xenes-Ag stack in the exposed regions.* ***(c)*** *Second lithography step with the negative pattern.* ***(d)*** *The sample is attached to the target substrate.* ***(e)*** *After completely removing the mica, the sample is washed in acetone to remove the resist.* ***(f)*** *The last lithography step is to define the regions where the Ag is to be removed (in this example it corresponds silicene channels definition).* ***(g)*** *After the Ag etching the completed sample is rinsed again in acetone to remove the resist.*

In the specific case shown in the Figure 3.10, a layer of epoxy glue was used as the adhesive layer and its Raman spectrum is characterized by a strong fluorescence background which also affects the silicene spectrum. The fluorescence background is closely related to the process of absorption by molecules which, having been excited to higher electronic states, emit fluorescence light while relaxing to their lowest vibrational level. In the glue case, this phenomenon is also enhanced due to the thermal degradation of the epoxy resin generated during heat curing. Although the value of the Raman shift is independent of the laser wavelength, this

phenomenon is closely linked to it, and one possible strategy to limit the problems is to use near-IR or UV laser sources or through photobleaching methods [100].
In our case, it is impossible to perform the latter process because it damages the Xene layer. Nonetheless, this effect does not affect the Raman peak position, enabling us to achieve a satisfactory signal-to-noise ratio. The overall so-generated background is corrected with a linear baseline during the fitting procedure, as will be shown in Chapters 4 and 5.

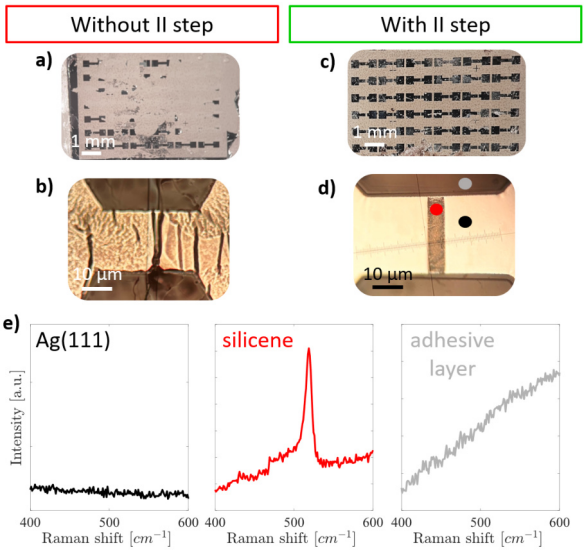

Figure 3.10: *Comparison of the results obtained without performing the second step of lithography* ***(a-b)*** *and performing it* ***(c-d)****. In the panel* ***(e)*** *it is shown the Raman characterization of the sample after the channel opening. The colored dots in* ***(d*** *indicate the positions of the Raman spectrum acquisition where the black, red and grey colors refer respectively to the Ag(111), silicene and glue regions.*

Alternative solutions with respect to glue, are also possible. It can be used a polymer layer, such as polymethyl methacrylate (PMMA), which, being spin-coated, can be more easily controlled in terms of thickness and subsequently used as a dielectric layer in a typical back-gated device configuration. In case a more precise control over the dielectric layer is desired, an additional solution is given by thickening the Al_2O_3 capping layer, for example, by Atomic Layer Deposition (ALD) growth, and either evaporating a metal layer on top or using directly a conductive

paste as the back gate.
As a last option, to further improve the process and increase the cleanliness and homogeneity of the surface, methods without an adhesive layer can be used to hold the sample together with the target substrate. Some possible alternative approaches are, for example, the cold welding process [101] based on the use of a metal layer, e.g., deposited on top of the Al_2O_3 layer, in order to force the union, at elevated pressure and temperatures, with a second metal layer evaporated on the target substrate. Another possible way is represented by the low-temperature direct bonding between the Al_2O_3 surface and a second Al_2O_3 layer deposited on top of the target substrate [102].

3.1.3 Etching procedures

In order to implement the transfer processes described in the previous Subsection 3.1.2, it is necessary to test and optimize the etching procedures for each of the materials involved. As already explained in Section 3.1, the capping layer consists of an aluminum oxide layer approximately 5 nm thick. Due to its oxide nature, it can be etched with a so-called Buffered Oxide Etchant (BOE) solution, which is commonly used in microfabrication for controllable desired etching and is composed of a mixture of hydrofluoric acid (HF) and ammonium fluoride (NH_4F) in different concentrations. Since in our specific case the thickness to be etched is extremely low, the BOE solution used is prepared with the following ratio:

$$BOE_{Al_2O_3} \rightarrow NH_4F : HF = 100 : 1 \tag{3.1}$$

resulting in an etching rate of approximately 7 nm/min. As a preliminary test, a striped pattern has been realized, resulting in regions of Al_2O_3 alternating with regions of only silicene, as shown in Figure 3.11a. The Al_2O_3 etching does not change the position of the Raman peak of silicene, but it affects only its intensity, as demonstrated by the line-scan mapping reported in Figure 3.11b. As can be seen from both the Scanning Electron Microscopy (SEM) image and the linear Raman map, the etched profile is not particularly sharp but shows a kind of thickness gradient and this is unfortunately a general tendency in wet etching, especially if the pattern has small features (for example, below 10 µm). One possible way to avoid the problem would be to use dry etching techniques through dedicated tools, instead of the wet methodology, in order to gain greater etching control and a higher fidelity of pattern replication.
In the case of 3D systems, wet etching can be defined as selective for

a material if a particular solution has a significantly lower etching rate when acting on other types of material. When dealing with 2D materials, owing to extremely low thickness, the entire concept of selectivity becomes relative and uncertain. For this reason, although BOE solution is commonly used for selective etching of oxides compared, for example, to bulk silicon, silicene and stanene can easily be etched if the BOE used is more aggressive, such as with a ratio of $NH_4F : HF = 7 : 1$, in approximately 1 minute. However, in the particular case of multilayer silicene, depending on thickness, it may be necessary to etch it through the widely used solution of potassium hydroxide KOH (20 wt%), for approximately 20 seconds.
Concerning the 300 nm thick Ag(111) layer, the chemical etching process must be carefully tested and calibrated. The commercial Ag etchant solutions based on nitric acid (HNO_3) are not appropriate as they severely damage the entire sample and are too fast to define a temporally controlled etching process.

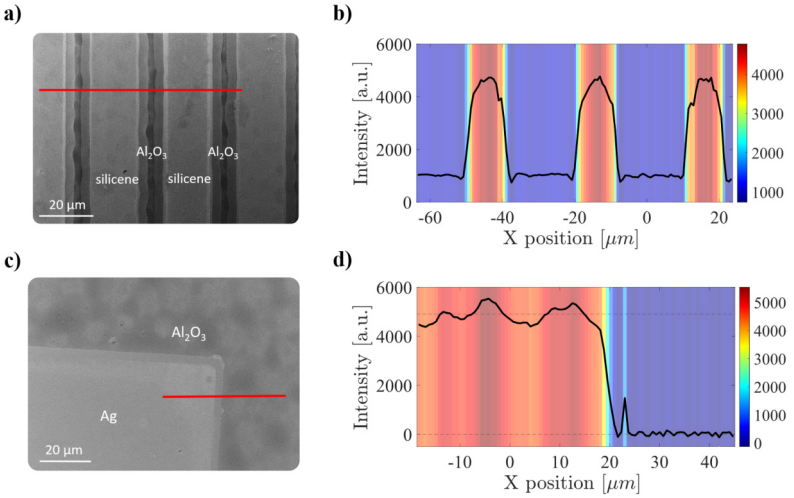

Figure 3.11: *Characterization of the different etching steps.* ***(a)*** *SEM image of a striped pattern alternating between regions where Al_2O_3 is present and regions where it has been etched. In red is highlighted the region of the line-scanning Raman mapping, shown in* ***(b)****, to monitor the intensity of the main silicene peak.* ***(c)*** *SEM image of a square region after the etching of Al_2O_3 and silicene. In red is highlighted the region of the line-scanning Raman mapping, shown in* ***(d)****, to monitor the intensity of the main silicene peak.*

Conversely, solutions based on potassium iodide (KI) and iodine (I_2)

represent an excellent alternative since they can perform the Ag selective etching without damaging the epitaxial Xene layers [99]. However, commercial solutions of this type have typical etching rates of ~ 1 µm/min and, therefore, are too fast. At the same time, diluting the solution leads to the formation of unwanted AgI salts as by-products [99] and, moreover, significantly slows down the entire process resulting in an incomplete removal of the Ag layer, which causes problems especially when defining electrical contacts through insulation trenches.
To avoid these problems it is necessary to prepare a *home-made* solution obtained by dissolving KI and I_2 powders in deionized (DI) water. The resulting Ag etching rate strongly depends on the temperature and concentration of the reagents. For example, higher concentrations of I_2 compared to KI speed up the etching process but do not facilitate the by-products dissolution, while the opposite improves the solubility of the AgI salts [103]. For example, in the case of the etching in the Fig. 3.9b, a faster and more aggressive Ag etching is preferred, contrary to the case in Fig. 3.9g in which greater control is required to avoid damage to the underlying materials. Specifically, in the latter case, the used solution had the following molar concentrations:

$$[KI] = 5.13 \text{ mol/L} \quad \text{and} \quad [I_2] = 0.98 \cdot 10^{-3} \text{ mol/L} \tag{3.2}$$

with an etching rate of ~ 50 nm/min. It is worth mentioning that the preparation of the solutions takes place under a chemical hood where the KI powder is slowly added to a becher with DI water and stirred at room temperature. Once the powder is completely dissolved, the small amount of I_2 is added, continuing to stir for several minutes until the I_2 crystals are completely dissolved.

3.2 Few-layer stanene samples

The few-layer stanene samples are grown in the Omicron NanoTechnology GmbH MBE system, described in Sec. 2.1, on undoped InSb(111) substrate. Before the growth, the substrate is treated with several cycles of sputtering and annealing so as to prepare the surface. Tin is evaporated at a rate of ~ 2 Å/min to the desired thickness (between 5 nm and 50 nm), keeping the substrate at room temperature.
Each sample is characterized by *in-situ* XPS performed before and after the Sn growth. A non-monochromatized X-ray source (Mg anode, $h\nu$ = 1253.6 eV) in surface-sensitive conditions (take-off angle of 37°) has been employed. Before the growth, the In 3*d* and Sb 3*d* core levels of the substrates are shown in Figure 3.12a-b, respectively. After the sputtering and annealing cycles, the substrate is not oxidized as evidenced by

the presence of single spectral lines related to the elemental In and Sb without the presence of the oxide-related components at higher binding energies. After tin growth, in addition to the previously described In 3d and Sb 3d core levels, the Sn 3d core levels (placed in between In 3d and Sb 3d) are also monitored, as shown in Figure 3.12c. The presence of heavy elements like In, Sb and Sn is reflected by the spin-orbit effects resulting in a spin-orbit separation, between the X $d_{5/2}$ and X $d_{3/2}$ components (where X is In, Sb or Sn), equal to Δ^{3d}_{In} = 7.55 eV, Δ^{3d}_{Sb} = 9.37 eV and Δ^{3d}_{Sn} = 8.40 eV.

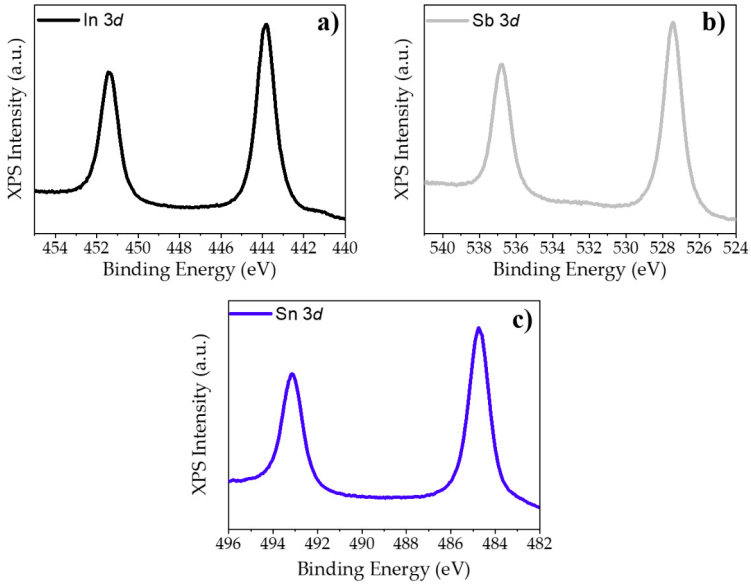

Figure 3.12: *XPS core levels respectively of* ***(a)*** *indium (In),* ***(b)*** *antimony (Sb) and* ***(c)*** *tin (Sn).*

When the samples are taken outside of the MBE chamber, Raman spectroscopy can be used to identify the presence of the α-Sn. Raman spectra have been acquired through a solid-state laser (514 nm) in a backscattering configuration coupled to an optical microscope equipped with a 50x objective, using a laser power of 1 mW and collecting 3 accumulations with an exposure time of 10 seconds. Figures 3.13a-b show the corresponding spectra of substrate and tin, together with the performed curve fit.
The InSb substrate exhibits two Raman peaks at approximately 180 cm^{-1} and 190 cm^{-1}, relative to the transverse optical phonon modes and the longitudinal optical mode [104], respectively, while the α-Sn is charac-

terized by a peak centred around 197 cm^{-1}, characteristic 1Γ peak, as reported in the literature [105, 106].
It should be noted that the three peaks turn out to be in the same frequency region, and therefore it is necessary to have a high lateral spatial resolution to be able to identify the presence of α-Sn.

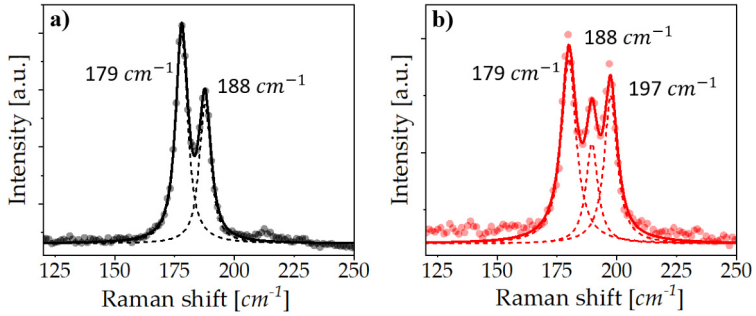

Figure 3.13: *Fitted Raman spectra of* ***(a)*** *InSb substrate and* ***(b)*** *α-Sn. The raw data are the scattered points, the solid curve is the corresponding fit result, and the dashed lines show the components used in the fitting procedure.*

3.2.1 Etching procedures

In this case, although the semiconductor substrate enables a direct approach to be tested, avoiding the need to develop an appropriate transfer process, in order to exploit the material properties, such as electrical measurements, it is necessary to be able to isolate the desired structures with isolation trenches by chemical etching. After several experimental tests, it has been found that the best approach to etching Sn is based on the use of a solution called *aqua regia*, realized with a mixture of nitric acid (HNO_3) and hydrochloric acid (HCl), with a ratio of:

$$HNO_3 : HCl = 1 : 3 \tag{3.3}$$

and diluted 1:50 in H_2O, in order to obtain an etching rate of $\sim$ 20 nm/min. It should be noted that this type of etching is strongly isotropic and therefore requires greater attention when producing patterns with small features (below 10 µm). Even in this case, however, dry etching techniques can be used if extreme precision is required.

Chapter 4

Silicene stabilization

As mentioned in Chapter 1, although silicene obtained by epitaxy is a well-established result [43, 54, 64, 107], its stabilization within a device architecture is still missing, due to severe environmental instability. So far, several methods have been implemented to protect silicene through top face encapsulation by a protective layer passivation (such as graphene [108], h-BN [109] or CaF_2 [110]) or, as in the present work, sequential deposition of Al_2O_3 layer [10]. Despite each method being universal, and in principle, extensible to other Xenes, this protection is limited to the top face of silicene, while, once it is detached from the growth substrate, the bottom face (namely, the interface with the substrate) is prone to fast environmental degradation [98].
Within this framework, the aim of this Chapter is to first show the degradation monitoring of the transferred silicene samples during ambient exposure and, subsequently, present a possible new solution to totally encapsulate silicene after substrate decoupling.

The main experimental results of this Chapter have been published in the article [111]. My personal contribution includes the *ex-situ* Raman analysis and the development of process and transfer methodologies.

4.1 Study of the environmental instability

First of all, the degradability of samples made of silicene directly grown on Ag(111) has been investigated in order to have as a reference the rate of the degradation process and to be able to compare and improve it, subsequently, with the new encapsulation method. For comparison, both monolayer and multilayer configurations of silicene have been

considered.
The delamination and transfer process, described in Figure 3.6, has been applied to each sample and the Ag layer was etched through the processing reported in Subsection 3.1.3. The samples were then exposed to the environmental conditions present in the laboratory, characterized by a temperature of 21 °C and a humidity level of 40%, monitoring the chemical status of silicene by means of Raman spectroscopy. The Raman spectra have been acquired with the 50× objective (0.75 numerical aperture), collecting 3 accumulations with an exposure time of 5 seconds and keeping the incident laser power below 4 mW to avoid damaging the samples.
In Figure 4.1 it is reported the Raman characterization in the case of monolayer and multilayer Si before and after transfer to the target substrate.

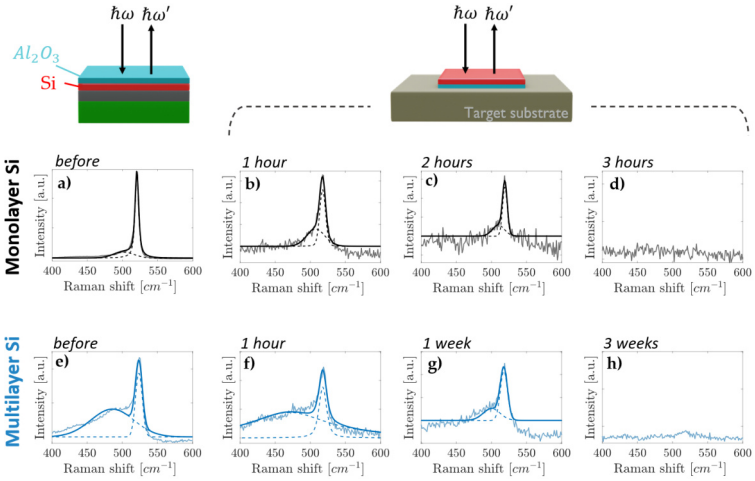

Figure 4.1: *Raman spectroscopy characterization of Al_2O_3-capped mono (a-d) and multilayer (e-h) silicene grown directly on Ag(111).* ***(a)*** *and* ***(e)*** *are the Raman spectra taken before processing, while* ***(b-d)*** *and* ***(f-h)*** *are the Raman spectra acquired after the sample transfer and hence from the Ag-free etched region. In each plot the faint curve is the raw data, the dark curve is the corresponding fit result and the two dashed curves show the two components used in the fitting procedure.*

It should be emphasized that the spectra shown are only some of the collected individual spectra, which may appear with slight differences. This is because, for each sample (of 1 cm^2 size) and every step of time, the spectra were collected in different spatial regions of the surface in

order to verify the material uniformity and, during the time monitoring, it was impossible to re-acquire the spectra in the exact same positions. The spectra shown in Figures 4.1a,e correspond to spectra acquired before the transfer process, i.e., directly after growth in MBE, and for this reason, do not exhibit high noise levels. Instead, the remaining spectra of Figures 4.1b-d and f-h were acquired after silver etching, i.e., on the transferred sample attached to the target substrate through a layer of glue. Therefore, the presence of glue is unavoidably responsible for the increased noise of the related spectra.
Furthermore, spectra acquired in the presence of the underlying glue layer are characterized by a strong background related to the fluorescence phenomenon, as shown in Figure 4.2a and, hence, depending on different factors, such as the variable glue thickness and inherent impurities, the spectra can be either more or less noisy.

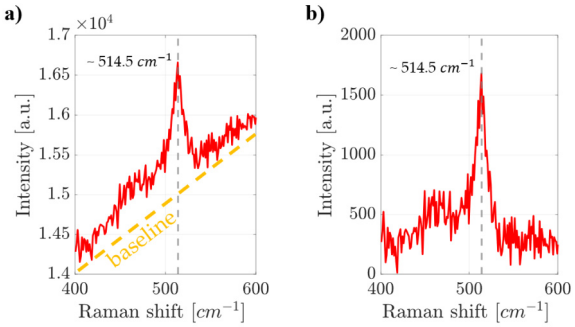

Figure 4.2: *Linear baseline correction procedure performed in the case of the Raman spectra acquired after Ag etching.* ***(a)*** *Raman spectrum obtained on the transferred sample.* ***(b)*** *The same Raman spectrum after the baseline correction.*

However, since the Raman peak position is not affected by this phenomenon and the spectrum can be acquired with a good signal-to-noise ratio, for each spectrum shown, the so-generated background has been corrected with a linear baseline subtraction during the fitting procedure (see Fig. 4.2b).
In order to fit the characteristic asymmetric spectrum of silicene, the Raman analysis has been carried out using a two-component Lorentzian-Gaussian model. After the MBE growth, the spectra of monolayer and multilayer silicene are respectively characterized by the main peak located at 518 cm^{-1} and 522 cm^{-1}, with a full-width half maximum (FWHM) of 8 cm^{-1} and 12 cm^{-1} (see Fig. 4.1a and e). The obtained values are in good agreement with the first-order Raman peak of silicene

[42, 92]. It should be noted, moreover, that in the case of a multilayer sample, the shoulder, located at lower frequencies, exhibits greater intensity, which can be attributed to the presence of an increased disorder. At the end of time monitoring, the results show that, after silver etching, in the case of monolayer silicene, the intensity of the main Raman peak decreases until it disappears completely after about 3 hours (Figure 4.1b-d). In the case of multilayer silicene, the time scale is quite different but the result does not change: the stability of the sample is extended only on the weekly scale, thus confirming the results already obtained for multilayer silicene, which is characterized by longer stability [92, 112]. Tables 4.1a-b show the values of the peak positions obtained with the fitting procedure, expressed as mean value with the relative standard deviation, respectively for monolayer and multilayer silicene, immediately after the silver etching and for each time step thereafter.

a)

Monolayer Si on Ag(111)	Peak 1 [cm^{-1}]	Peak 2 [cm^{-1}]	Intensities ratio (p2/p1)
after etching	516,8 ± 0,4	490 ± 1	~ 0,2
1 hour	517,6 ± 0,5	506 ± 2	~ 0,2
2 hours	518,7 ± 0,5	510 ± 2	~ 0,2
3 hours	/	/	/

b)

Multilayer Si on Ag(111)	Peak 1 [cm^{-1}]	Peak 2 [cm^{-1}]	Intensities ratio (p2/p1)
after etching	519,6 ± 0,4	480 ± 1	~ 0,4
1 hour	518,6 ± 0,4	475 ± 2	~ 0,4
1 week	518,0 ± 0,5	500 ± 1	~ 0,4
3 weeks	/	/	/

Table 4.1: *Fit results obtained for single **(a)** and multilayer **(b)** silicene samples.*

During the silicene degradation process, the absolute Raman peak intensity decreases, but the relative intensity, i.e., the intensities ratios, remains stable for each type of sample.
It should be also noted that, in both cases, if compared with the values obtained directly after the growth, the frequency of the main Raman peak immediately after the etching, results redshifted of approximately 2 cm^{-1} for the monolayer and 3 cm^{-1} for the multilayer. This shift is present when the transferred sample is characterized by Raman spectroscopy after the Ag etching and indicates a mechanism of strain release both during mica delamination and after Ag etching.

4.2 All-Around Encapsulation

The same time monitoring was then repeated for the samples consisting of silicene-stanene heterostructure in which the stanene layer, directly grown on Ag(111), is used as a template for the silicene growth (see Fig. 3.1b). The idea behind this experiment is to exploit the stanene layer, on which the silicene is grown, as a sacrificial layer when the flipped sample is delaminated and stripped of silver. In this scheme, then, the silicene would be encapsulated between the Al_2O_3 layer and the stanene, thus realizing an all-around encapsulation (AAE). For comparison, both single and multilayer silicene samples have been tested, using the same previous parameters, i.e., collecting 3 accumulations with an exposure time of 5 seconds. After the MBE growth, the spectra of monolayer and multilayer silicene are respectively characterized by the main peak located at 517 cm^{-1} and 523 cm^{-1}, with a FWHM of 9 cm^{-1} and 11 cm^{-1} (see Fig. 4.3a and e). The obtained results are reported in Figure 4.3.

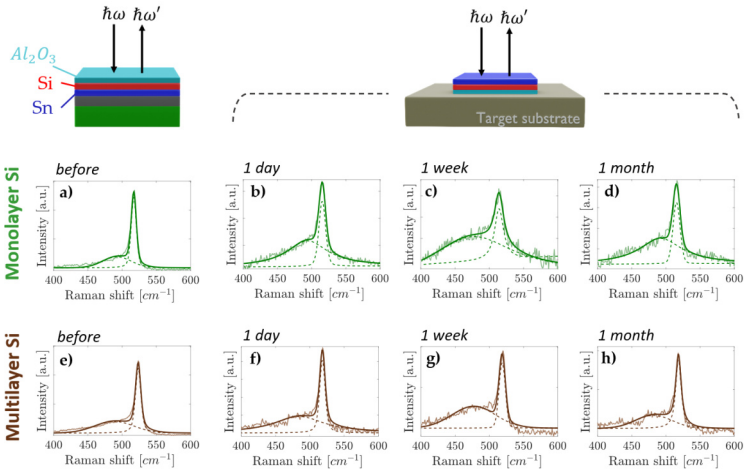

Figure 4.3: *Raman spectroscopy characterization of mono* ***(a-d)*** *and multilayer* ***(e-h)*** *silicene in the AAE scheme.* ***(a)*** *and* ***(e)*** *are the Raman spectra acquired from the Al_2O_3 capping layer before the AAE process.* ***(b-d)*** *and* ***(f-h)*** *are the Raman spectra acquired after 1 day* ***(b-f)****, 1 week* ***(c-g)****, and 1 month* ***(d-h)*** *after Ag etching for mono and multilayer silicene, respectively. In each plot the faint curve is the raw data, the dark curve is the corresponding fit result, and the two dashed curves show the two components used in the fitting procedure.*

After silver etching, in this case, it can be noticed that both for the

monolayer and multilayer case, the stability of the sample has been improved in a timescale of weeks, as evidenced by the absence of significant changes in the Raman spectra over time. As reported in the previous Section 4.1, the characterization has been again extended to the entire surface of the samples by scanning different spatial positions for each step of the time monitoring. In the Tables 4.2 the peak position values obtained by the fitting procedure and the relative intensities ratio are shown for both silicene configurations.

a)

Monolayer Si heterostructure	Peak 1 [cm^{-1}]	Peak 2 [cm^{-1}]	Intensities ratio (p2/p1)
after etching	515,0 ± 0,3	490 ± 1	~ 0,2
1 day	515,3 ± 0,4	488 ± 1	~ 0,3
1 week	514,2 ± 0,6	480 ± 2	~ 0,3
1 month	514,8 ± 0,3	492 ± 1	~ 0,3

b)

Multilayer Si heterostructure	Peak 1 [cm^{-1}]	Peak 2 [cm^{-1}]	Intensities ratio (p2/p1)
after etching	518,9 ± 0,2	486 ± 2	~ 0,2
1 day	518,3 ± 0,3	487 ± 1	~ 0,2
1 week	517,6 ± 0,3	480 ± 1	~ 0,3
1 month	517,8 ± 0,4	479 ± 2	~ 0,2

Table 4.2: *Fit results obtained for single **(a)** and multilayer **(b)** silicene heterostructures.*

The results therefore demonstrate that even after one month, it is possible to identify the presence of silicene by still obtaining its characteristic Raman spectrum unvaried. This confirms that the stanene represents a sacrificial layer when the sample is transferred to the target substrate and the silver is etched. Indeed, after silver removal, the stanene is exposed to the air, sacrificing itself to prevent the silicene oxidation and degradation, at least in a sufficiently long time frame for integration into a device layout. After the successful implementation of the AAE scheme in the case of silicene sandwiched between the stanene layer and the Al_2O_3 capping layer, a thinner sample configuration has been tested in order to investigate the maximum limit of the scheme in terms of thicknesses. To do this, the Al_2O_3 thin layer, deposited at the end of growth in MBE, is replaced with an additional single layer of tin, epitaxially grown on top of the silicene surface. The sketch of the new stacking is reported in Figure 4.4a.
The effectiveness of the *in-situ* encapsulation of silicene by a thin layer of aluminum oxide had already been demonstrated in the case of silicon

grown directly on Ag(111) [10] and was then easily extended to the case of heterostructures [11].
However, replacing this type of capping layer with another Xene requires preliminary validation before the AAE scheme can be applied to this type of sample. For this purpose, the new Sn/silicene/stanene sample has been first characterized through XPS to investigate its chemical status after 1 day of ambient exposure.
On a $\sim 1 \times 1$ cm^2 sample surface two distinct spatial locations have been sampled and the results are shown in Fig. 4.4b-d. The first plot refers to the Si $2p$ core level, while the remaining two are related to the Sn $3d_{5/2}$ core level acquired with a different value of TOA.

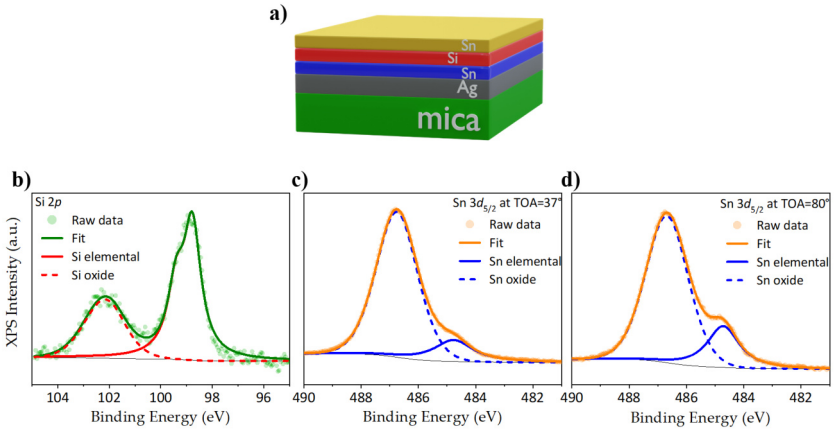

Figure 4.4: *XPS analysis of the Sn/silicene/stanene on Ag(111) configuration after 1 day of exposure to ambient conditions.* ***(a)*** *Si 2p core level where the red curve is related to the elemental Si component, the red dashed to the oxidized component, and the green one is the overall fit.* ***(b)*** *Sn $3d_{5/2}$ core level measured at the take-off angle of 37° and* ***(c)*** *Sn $3d_{5/2}$ core level at take-off angle of 80° where the blue curve is related to the elemental Sn component, the blue dashed to the oxidized component, and the orange one is the overall fit.*

In the case of silicon (Fig. 4.4b), the most intense component at $E_B = 98.77$ eV is related to the elemental Si, characterized by an asymmetric shape profile due to the doublet separation of 0.63 eV between the $2p_{1/2}$ and $2p_{3/2}$. Instead, the minor component at $E_B = 101.99$ eV is related to the formation of silicon oxide (SiO_2) [11]. This result is in agreement with what has been obtained also in the case of the Al_2O_3 capping layer [44], and hence confirms the possibility of partial oxidation of silicene caused by an inhomogeneous capping layer which can present defects

and percolation paths.
Considering instead the Sn $3d_{5/2}$ core level, interestingly, when the XPS is performed with a TOA $= 37^{o}$ (see Fig. 4.4c), i.e., surface sensitive conditions, the main component (at E_B = 486.76 eV) results from the oxidized tin [113, 114], while, if the XPS is carried out with a TOA $= 80^{o}$ (see Fig. 4.4d), i.e., bulk sensitive conditions, the component related to the elemental Sn state, at E_B = 484.77 eV, increases [11].
This result thus proves that, after one day of ambient exposure, the top Sn layer is almost completely oxidized, while the bottom one, between Ag substrate and silicene, is in its pristine chemical status. After establishing the validity of the encapsulation through the use of an additional layer of Xene on top of the sample, the time monitoring through Raman spectroscopy has been performed for the non-transferred single-layer silicene protected by the top Sn capping layer up to 1 month, as shown in Figure 4.5a-d.
Directly after the growth, the Raman spectrum of the single-layer silicene embedded into two Sn layers shows the main peak located at 518 cm^{-1}, with a FWHM of 10 cm^{-1} (see Fig. 4.5a) that is, in agreement with the values of previous samples.

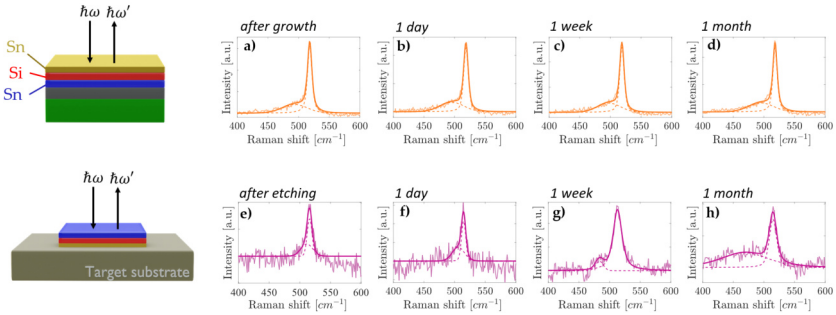

Figure 4.5: *Raman spectroscopy characterization of monolayer silicene embedded into two Sn layers.* ***(a-d)*** *Raman spectra monitored from the top Sn capping layer after growth up to one month of air exposure.* ***(e-h)*** *Raman spectra monitored from the bottom Sn capping layer after the sample transfer and subsequent Ag etching up to 1 month of air exposure. In each plot the faint curve is the raw data, the dark curve is the corresponding fit result, and the two dashed curves show the two components used in the fitting procedure.*

The results, after different time steps, show no significant change in the Raman spectrum of silicene, thus demonstrating that the top Sn capping layer can replace the Al_2O_3 as a method of preserving silicene in ambient

conditions.
At this point, the sample composed of monolayer silicene encapsulated into two Sn layers has been transferred from the growth substrate, i.e., Ag(111) on mica, to a target substrate, in order to repeat the Raman spectroscopy time monitoring also for the thinnest configuration represented by the Sn/silicene/stanene stack.
The results obtained up to 1 month are shown in Figure 4.5e-h. The silicene first-order Raman peak is still traceable even one month after the Ag etching, thus demonstrating the effectiveness of the AAE scheme for the thinnest configuration. As can be noticed in Fig. 4.5, the orange curves are noisier compared to the violet ones because the first ones have been acquired immediately after the sample was grown, i.e., once it was taken out of the UHV conditions inside the MBE chamber, while the latter have been acquired after performing the transfer process shown in Fig. 3.6, i.e., on the transferred sample attached to the target substrate through the glue.
In fact, as already explained in Sec. 4.1, the presence of the glue is unavoidably responsible for the increased noise of the related spectra and, moreover, in order to ensure a homogenous match, each Raman spectrum has been acquired with the same previous parameters reported. Tables 4.3a-b show the peak position values obtained from the fitting procedure and the relative intensities ratios.

a)

Sn-Si-Sn	Peak 1 [cm^{-1}]	Peak 2 [cm^{-1}]	Intensities ratio (p2/p1)
after growth	518,1 ± 0,4	490 ± 1	~ 0,1
1 day	518,5 ± 0,6	493 ± 1	~ 0,2
1 week	518,7 ± 0,3	491 ± 1	~ 0,2
1 month	518,1 ± 0,5	492 ± 1	~ 0,2

b)

Sn-Si-Sn	Peak 1 [cm^{-1}]	Peak 2 [cm^{-1}]	Intensities ratio (p2/p1)
after etching	515,2 ± 0,3	502 ± 2	~ 0,3
1 day	514,0 ± 0,4	503 ± 2	~ 0,3
1 week	514,8 ± 0,6	490 ± 2	~ 0,2
1 month	515,0 ± 0,2	486 ± 2	~ 0,3

Table 4.3: *Fit results obtained in the case of silicene sample protected by the Sn layer.* ***(a)*** *Refers to the case of spectra acquired after the growth and* ***(b)*** *refers to the spectra acquired after the sample transfer.*

Finally, since Figures 4.3 and 4.5 show only some of the collected individual spectra, Figure 4.6 reports the standard deviation of the normalized

spectra for each sample configuration. In this way, it can be noted that, due to the presence of glue, more significant deviations of Raman spectra occur in the case of the transferred sample after the Ag etching (Fig. 4.6a-b,d) compared to the characterization performed directly after the growth (Fig. 4.6c).
The AAE scheme proved to be effective in protecting silicene from degradation both when implemented with the thin Al_2O_3 layer and with 1 ML-thick Sn layer on the top surface. It can be applied to single-layer and multilayer silicene, provided that this is grown on the stanene on Ag(111) template.

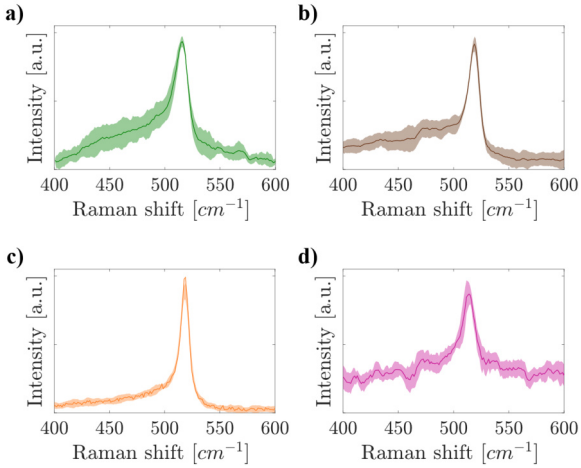

Figure 4.6: *Mean spectra (solid lines) and standard deviations (shaded regions) for single* ***(a)*** *and multilayer* ***(b)*** *silicene heterostructures, and for silicene sample protected by the Sn layer, where* ***(c)*** *refers to the case of spectra acquired after the growth and* ***(d)*** *refers to the spectra acquired after the sample transfer.*

Chapter 5

Strain engineering of silicene

Thanks to their excellent properties combined with high mechanical robustness, 2D materials are of particular interest for the near-future nanotechnology concerning the Internet of Things (IoT) world, such as flexible and wearable electronics or photonics [12, 13]. Examples of applications in this context are flexible transistors, strain sensors, electronic tattoos and origami-inspired bendable systems [115, 116, 117, 118].
Both organic and inorganic 2D materials could represent the perfect candidates since they exhibit optical and electronic properties suitable for application in nano-photonics and -electronics and, at the same time, they are characterized by robust mechanical properties, which allow them to withstand high levels of strain before fracturing.
In this context, it is possible to refer to strain engineering, to denote a general strategy applied to the materials in order to tune their fundamental properties and, for example, to enhance device performance. Mechanisms accessible through strain engineering are, for instance, exciton manipulation [119, 120], carrier mobility boosting [14, 121, 122], piezoresistivity [123] and electronic bandgap tuning [124].
As mentioned in Chapter 1, although exfoliated 2D material flakes are highly promising, their lateral dimension is typically limited to the micrometre scale thus severely limiting their integration in the process of large-scale device realization.
In this respect, silicene, ensuring large-scale uniformity [125], is a valid alternative to scale up flexible devices on a cm^2 scale with the benefit of compatibility with both complementary metal-oxide semiconductor

(CMOS) platform and current silicon semiconductor technology.
The aim of this Chapter is to present the bendable membranes based on silicene and silicene-stanene heterostructures, reporting their strain-responsive behaviour to the application of macroscopic and microscopic mechanical deformations. Finally, a prototype realization of a silicene piezoresistor will be presented, as a first demonstration of the technological potential and a new step towards integration into flexible device architectures.

The main experimental results of this Chapter have been published in the article [126]. My personal contribution includes the Xene membranes fabrication, realization of lithography patterns, performing bending experiments and both Raman and electrical characterization.

5.1 Raman characterization

To realize the bendable membranes, the procedure presented in Figure 3.4 has been implemented in the case of single and multilayer silicene directly grown on Ag(111) (see Fig.3.1a) and single and multilayer silicene on stanene template to form the heterostructure configuration (see Fig. 3.1b).
Raman spectroscopy represents a highly effective tool to monitor the response of the samples as a function of an applied mechanical deformation [127] and a variation of the Raman shift can be related to an extrinsically induced strain in the silicene layer, if the incident laser power is kept below 5 mW to avoid optothermal effects.
In order to better quantify the Raman response of silicene membranes under externally applied uniaxial strain, a three-point bending device, whose operational principle is shown in Figure 5.1a, has been assembled. The instrument is equipped with two cylinders placed on the same plane, which, thanks to a synchronized vertical movement, allows controlled bending of the sample that has been previously centred and fixed on a third cylinder. When performing strain engineering experiments with optical spectroscopy techniques, this geometry is the most convenient as it allows to maintain the vertical position of the sample almost fixed during the bending cycles, avoiding the re-focusing between different acquisitions [124, 128]. The thickness of the sample ($\sim$ 300 nm) is negligible compared to the total thickness $d \sim 0.2$ mm of the flexible polymer and tape and, since d is significantly smaller than the radius of curvature r of the membrane (see Figure 5.1a), the applied strain can be approximated as:

$$\varepsilon = \frac{d}{2r} \tag{5.1}$$

stating that the sample is under pure tensile loading [122, 129]. The bending device can be placed under the microscope of the Raman spectroscopy setup in order to monitor the evolution of the silicene vibrational mode by applying different incremental tensile strain levels.

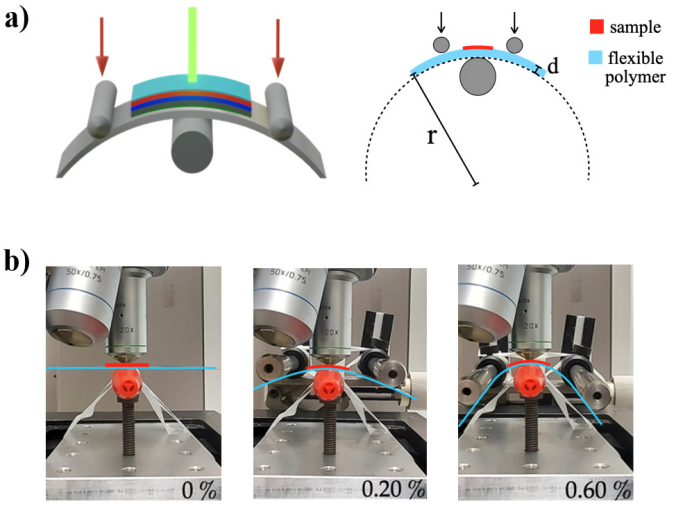

Figure 5.1: ***(a)*** *Schematization of the setup used for applying macroscopic uniaxial strain to the bendable membranes.* ***(b)*** *Optical pictures of the sample upon application of 0%, 0.2% and 0.6% uniaxial strain (the silicene membrane and the supporting flexible substrate are highlighted in red and cyan, respectively).*

The vertical displacement of the two cylinders is controlled through a rotating mechanism and, by executing a defined number of revolutions, the desired height can be reached. Before acquiring the measurements, a general calibration is carried out to calculate and determine the fixed strain values to be applied to each sample. Using a tripod, photos of the curved Polyethylene terephthalate (PET) substrate, from the same position and angle, have been taken and analyzed through vector graphics software, always taking a graduated scale as a reference to match millimetre scale and points (pt) on the screen. In this way, it is possible to obtain an estimation of the maximum and minimum value of the osculating circle diameter that best approximates the curvature and use the average value to extrapolate the percentage strain level. Based on the geometry of the bending device, the strain that can be applied is in the range 0-0.6%.
In Figure 5.2, it is shown the result obtained for each type of sample: Figures 5.2a,c refer to single and multilayer silicene directly grown on

Ag(111) substrate, while Figures 5.2b,d refer to single and multilayer silicene grown on top of stanene layer to form the heterostructure configuration. Each acquired spectrum has been fitted with a two Lorentzian-Gaussian component curve [42], using the Voigt profiles, through the WiRE (Windows-based Raman Environment) software by Renishaw, in order to extrapolate the peak positions values. For each applied strain value, the spectrum acquisition is performed in ten different spatial positions of the samples surface, within an area of $\sim$100 μm^2. As a result, it is possible to express the main peak position values as a mean value associated with a standard deviation, represented by the error bars shown in Figures 5.2c,d.

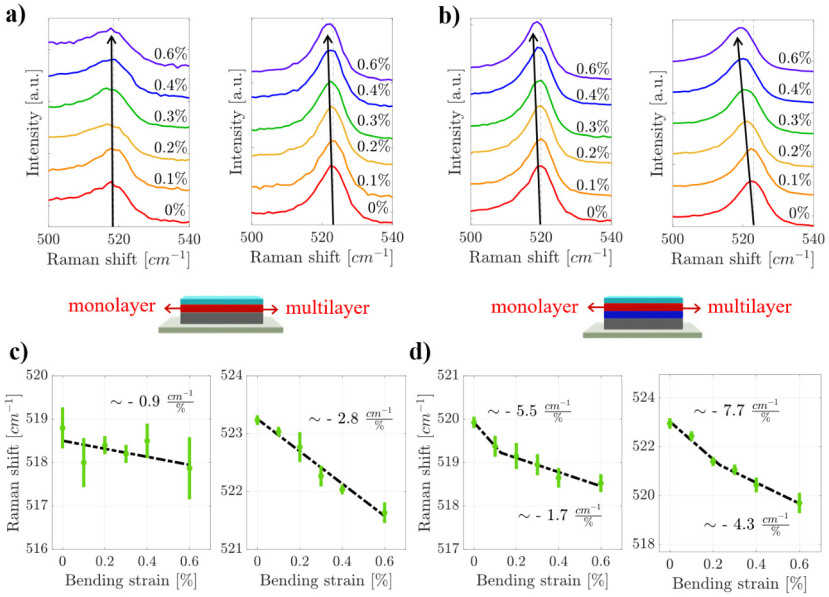

Figure 5.2: *Raman investigations of the bendable membranes based on mono- and multi-layer silicene without* ***(a)*** *and with* ***(b)*** *the stanene layer to form the heterostructure as a function of the applied strain. Frequency position of the Raman modes of the bendable membranes based on mono- and multi-layer silicene without* ***(c)*** *and with* ***(d)*** *the stanene layer to form the heterostructure as a function of the applied strain.*

When the uniaxial strain is applied, there is an increase in Si-Si bond length and a decrease of the atomic interaction, resulting in an expected redshift of the vibrational frequency of the silicene Raman mode, but, as can be seen, the evolution of the Raman spectra displays differences in the response of the silicene-based membranes. In the case of monolayer

silicene on Ag(111), the main component related to the Raman mode has extremely low sensitivity to the applied tensile strain, while the multilayer silicene on Ag(111) is more responsive.
But interestingly, the strain responsitivity is even notable when the stanene layer is introduced to form the heterostructure (Figure 5.2b left panel for the monolayer silicene on stanene, and the right panel for the multilayer silicene on stanene). By performing a linear regression of the experimental data, it is possible to have a quantitative estimation of the strain sensitivity of the samples. The results are shown in Table 5.1. The mono and multilayer silicene membranes display a spectral shift rate respectively of -0.9 $cm^{-1}\%^{-1}$ and -2.8 $cm^{-1}\%^{-1}$, while the Raman response of the heterostructures is characterized by a bimodal linear regime (see Fig. 5.2d). Specifically, the monolayer silicene heterostructure presents a shift rate of -5.5 $cm^{-1}\%^{-1}$ up to 0.1 % of uniaxial strain and -1.7 $cm^{-1}\%^{-1}$ for larger strain value, and the multilayer silicene heterostructure shows spectral shift rates of -7.7 $cm^{-1}\%^{-1}$ up to 0.2 % of uniaxial strain and -4.3 $cm^{-1}\%^{-1}$ for larger strain values.
To determine this behavior, in the case of the heterostructure, the curve has been treated as an elementary broken-line function that has a single break point, and which can therefore be written in the form:

$$f(x) = A|x - x_b| + Bx + q \tag{5.2}$$

where the variable x represents the strain values and x_b corresponds to the break point. The fit parameters are A, B, q, including also the break point ranging between 0 and 0.3%. By extrapolating the values of the coefficients, the two slopes for the respective regimes are defined as:

$$m_1 = B - A \quad \text{and} \quad m_2 = A + B. \tag{5.3}$$

The analysis reported in Table 5.1 confirms that a bimodal linear regime provides the best chi-square (χ^2) value for the heterostructure configuration both in the case of mono and multilayer silicene samples. It is then possible to state that the heterostructure configuration is characterized by an increased strain responsivity of the silicene layers, at least for the strain range below 0.3%, and the observed bimodal regime is strictly connected with the presence of the stanene layer introduced below the mono and multilayer silicene.
As the model already developed for graphene [127], it is possible to use the strain-dependent Raman results shown in Figure 5.2c-d to derive the Grüneisen parameter γ, for the silicene vibrational mode.
The thermodynamic Grüneisen parameter [130] originally expressed the

change in internal energy of an isotropic solid as a function of a change in pressure at constant volume, but it can be asserted, more generally, that it provides a connection between the thermal and mechanical parameters of the material. In fact, since the internal energy is determined by the phonon modes, the macroscopic Grüneisen parameter can also be extended to a microscopic approach: the response of the lattice vibrations to stress or temperature variation is related to the phonon-phonon interactions causing anharmonicity of the crystal potential [131], which reflected in a change of the Raman mode wavenumber.

	monolayer Si	*multilayer Si*	*heterostructure (monolayer)*	*heterostructure (multilayer)*
slope (single line)	- 0.9 $cm^{-1}\%^{-1}$	- 2.8 $cm^{-1}\%^{-1}$	- 2.3 $cm^{-1}\%^{-1}$	- 5.4 $cm^{-1}\%^{-1}$
χ^2	0.37	0.97	0.89	0.97
slopes (two lines)	/	/	- 5.5 $cm^{-1}\%^{-1}$ - 1.7 $cm^{-1}\%^{-1}$	- 7.7 $cm^{-1}\%^{-1}$ - 4.3 $cm^{-1}\%^{-1}$
χ^2	/	/	0.97	0.99

Table 5.1: *Fitting analysis of the strain-dependent Raman response.*

Given a general strain tensor ε, any type of strain configuration can be decomposed into a hydrostatic component ε_h and a shear component ε_s that, assuming equal off-diagonal components, can be respectively expressed as [132]:

$$\varepsilon_h = \varepsilon_{xx} + \varepsilon_{yy} \tag{5.4}$$

$$\varepsilon_s = \sqrt{(\varepsilon_{xx} - \varepsilon_{yy})^2 + 4\varepsilon_{xy}^2} \tag{5.5}$$

where x and y are the longitudinal and transverse directions with respect to strain. In the case of a uniaxial strain applied along x direction, if ν is the Poisson's ratio, the diagonal tensor components satisfy the relations [133]:

$$\varepsilon_{xx} = \varepsilon \quad \text{and} \quad \varepsilon_{yy} = -\nu\varepsilon. \tag{5.6}$$

The solution of the secular equation leads to the phonon shift rates expressed as [134]:

$$\Delta\omega_m^{\pm} = -\omega_m^0 \gamma_m \varepsilon_h \pm \frac{1}{2}\beta_m \omega_m^0 \varepsilon_s \tag{5.7}$$

where ω_m^0 is the m peak position at zero strain, γ_m is the phonon-mode Grüneisen component and β_m is the shear-strain phonon deformation potential. The hydrostatic strain is related to an isotropic size change of the atomic lattice and leads to a Raman frequency shift determined by the Grüneisen parameter γ. The shear strain, instead, is related to an anisotropic distortion of the atomic lattice and leads to a peak splitting governed by the shear deformation potential β.
In our case, the spectra show evident signatures exclusively of the hydrostatic component since, within the limits of experimental resolution, only the E_{2g} peak shift can be identified without any trace of peak splitting. For this reason Eq. 5.7 can be written as:

$$\Delta\omega_{E_{2g}} = -\omega^0_{E_{2g}}\gamma_{E_{2g}}(1-\nu)\varepsilon. \tag{5.8}$$

In this specific case, it is not trivial to express a single Poisson coefficient since one is considering a stack of different materials. As far as the sample is concerned, only the silver substrate ($\sim$ 300 nm) can be taken into account as it represents the predominant thickness. Furthermore, since in all the considered samples, after the strain application, the Raman peak position returns to its initial value, it is possible to state that there is a good adhesion between the sample and the flexible PET substrate, which also has a Poisson coefficient value comparable [127] to that of silver, $\nu_{Ag} = 1/3$ [135].
Combining equation 5.8 with the results in Figure 5.2 for the monolayer and multilayer silicene, results respectively in:

$$\gamma_{\text{mono,Si}} = 0.26 \quad \text{and} \quad \gamma_{\text{multi,Si}} = 0.80 \tag{5.9}$$

while for the heterostructure case, it is possible to derive respectively for the monolayer and multilayer silicene:

$$\gamma_{\text{monoH,Si}} = 0.67 \quad \text{and} \quad \gamma_{\text{multiH,Si}} = 1.54. \tag{5.10}$$

In order to derive a single Grüneisen parameter for each sample configuration, for the heterostructures case it has been used the single linear regime fit of the Raman response as a function of the applied strain reported in Table 5.1. For comparison, the values obtained considering the bimodal regime are reported in Table 5.2.
These values represent the first experimental results of a quantitative estimation of the Grüneisen parameters for silicene supported by different growth templates, but making a comparison with theoretical values is not straightforward, since most of them refer to free-standing silicene, i.e., supported by no substrate. At the same time, it has to be considered

that the theoretical predictions of the vibrational properties of Xenes turned out to be strongly affected by the buckling configuration, type and amount of strain applied and substrate interaction [136]. In particular, the mechanical and electronic properties of silicene are decisively affected by the interaction with the substrate in a different way [137]. The dependence of the silicene electronic properties on the Ag(111) is dramatically reduced when the stanene buffer layer is placed in between. At the same time, however, the theoretical structural models of the silicene-stanene heterostructures [11] have demonstrated a geometrical intermixing of the Xene layers, which can be responsible for the observed improved strain transfer when stanene is incorporated into the membrane.

Sample	Grüneisen parameter (**single** linear regime)	Grüneisen parameter (**bimodal** linear regime)
heterostructure (monolayer)	0.67	1.50 for $\varepsilon < 0.1$ % 0.50 for $\varepsilon \geq 0.1$ %
heterostructure (multilayer)	1.54	2.20 for $\varepsilon < 0.2$ % 1.23 for $\varepsilon \geq 0.2$ %

Table 5.2: *Calculated Grüneisen parameters for the heterostructures considering a single and a bimodal linear regime in the strain-dependent Raman response of Fig. 5.2d.*

5.2 Micro-scale wrinkles

Through the three-point bending system of Fig. 5.1 it is possible to test the strain-responsivity of the membranes on a macroscopic length scale ($\sim$ millimeters) of the mechanical deformation. However, it could be also interesting to investigate the strain response on a different length scale comparable to micro- or nano-scale of typical device architectures. Indeed, wrinkles formation has been reported as an effective method to strain-engineer the material properties, as it allows to localize a high level of stress in a limited region of the 2D material (typically from a few microns to hundreds of nanometres scale) [120].
For this reason, a method to intentionally induce micro-scale uniaxial wrinkle formation has been implemented and tested in the case of the most strain-responsive membrane, i.e., the multilayer silicene-stanene heterostructure. Periodical wrinkles can be generated by releasing a certain amount of elastic tension during the detachment of the membranes from the flexible polymer substrate (see sketch in Figure 5.3a). To quanti-

tatively describe the strain distribution throughout the wrinkles, Raman spectroscopy mapping has been performed in a region of hundreds of μm^2, as shown in Figure 5.3b.
From the Raman mapping, it is possible to investigate the variation of the Raman peak position as a function of the spatial position. In particular, in the lateral regions of each wrinkle, there are areas where the sample shows the peak position around 523-524 cm^{-1}, in agreement with the data at zero strain value in Figure 5.2b, which can therefore be referred to as flat; at the top of the wrinkle, however, one can identify an area where the Raman peak positions shift towards lower wavevectors as a function of the wrinkled morphology parameters, such as the lateral size and height amplitude. In order to investigate the wrinkle morphology, atomic force microscope (AFM) characterization has been performed across the wrinkle modulation (Fig. 5.4). According to the topography and height profile, a single wrinkle has a lateral size $l \sim 35$ µm, and a vertical displacement $h \sim 1.5$ µm.

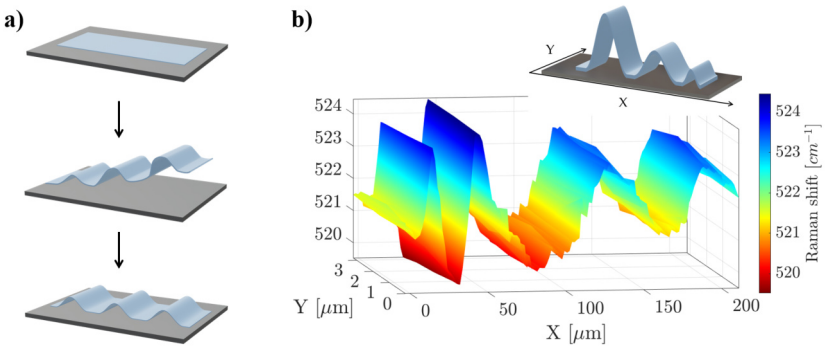

Figure 5.3: ***(a)*** *Schematization of the tension release process that leads to the formation of micro-wrinkles into the membranes.* ***(b)*** *Spatial map of the frequency position of the main silicene Raman peak. Inset: a sketch of the wrinkles mapped in the Raman measurements.*

The maximum of the uniaxial tensile strain ε_M, is accumulated at the top of the wrinkle and can be approximated according to the conventional strain model [120] for 2D materials:

$$\varepsilon_M = \frac{\pi^2 h d}{(1-\nu^2) l^2} \tag{5.11}$$

where d is the thickness of the wrinkled sample, h and l are respectively the vertical displacement and the lateral size of the wrinkle where the

profile can be approximated to a circular shape (it has been considered $h \sim 0.5$ µm from the topmost of the wrinkle in Figure 5.4 corresponding to $l \sim 15$ µm), and ν is the Poisson's coefficient of the wrinkled material. For comparison, wrinkles formation has been induced in a reference sample made by only the Ag/Al_2O_3 stack and structures with the same morphological features were observed. This result confirmed that the wrinkles composed of silicene/stanene stack are compliant with the surface modulations produced in the metallic substrate without delamination from it. For this reason, one possible approximation of the maximum tensile strain on top of the wrinkle can be obtained by replacing in equation 5.11 the Poisson's coefficient of the Ag film (d $\sim$ 300 nm), $\nu_{Ag} = 1/3$ [135].

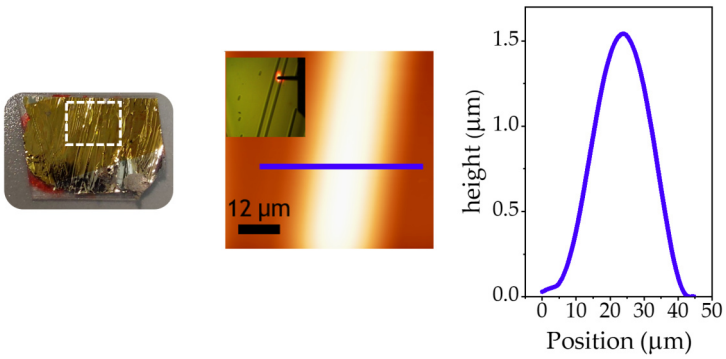

Figure 5.4: *Optical picture of the wrinkled sample with the indication of the wrinkled area and AFM topography and height profile of a selected wrinkle.*

In this way, it is possible to obtain the percent maximum tensile strain of $\sim$ 0.7% at the top of the wrinkle. Moreover, if considering that the Young's modulus of the Ag layer is $E_{Ag} = 80$ GPa [138], thanks to Hooke's law:

$$\sigma = \varepsilon E \tag{5.12}$$

an estimate of the maximum stress in the wrinkle can be obtained, which in this case turns out to be 250 MPa.
On top of the wrinkle investigated by AFM, a maximum Raman frequency shift of $\sim$ - 3 cm^{-1} has been measured with respect to the flat region. Hence, by comparing this result with the values obtained for the macroscopic deformation shown in Fig. 5.2b predicting a strain value of $\sim$0.6%, it can be noted a good agreement with the value derived using

the equation 5.11.
One of the possibilities that arises from the wrinkled geometry is the study of the thermal response of the silicene-stanene membrane as a function of the strain. This can be done by comparing the thermal Raman characterization performed by globally heating the sample through a hot plate with the optothermal response of the sample when the Raman laser source is used both as a probe and a local heater characterized by different incident powers [139].
Through Raman spectroscopy, it is possible to study the temperature dependence of the phonon frequency shifts and derive, for example, the thermal properties of the material such as the thermal conductivity. In all measurements carried out, it has always to be considered that the experimental parameters derived are relatives to the entire silicene/stanene/Ag stack, since, in any case, the Ag layer plays a predominant role in heat dissipation.
Considering the atomic lattice potential energy in the harmonic approximation, it becomes impossible to take into account the temperature dependence of the lattice constant and consider, for instance, the thermal expansion contribution and the anharmonic effects [140]. In particular, the first one is strictly related to temperature and pressure variations, while the second one derives mostly from the phonon-phonon coupling. The anharmonicity, in particular, often results in a Raman frequency shift and a widening of the spectrum, which can be described by a change in the phonon self-energy Σ, expressed as a complex quantity [140]:

$$\Sigma = \Delta(\omega(\mathbf{q}), T) + i\Gamma(\omega(\mathbf{q}), T) \tag{5.13}$$

where the real part is related to the frequency shift and results in the temperature dependence of the phonon frequencies, while the imaginary part is the damping, which partially describes the broadening of the Raman mode.
Moreover, if the material is not suspended, as in the present case, the substrate contribution must also be taken into account. For these reasons, the temperature-dependent Raman shift $\Delta\omega$ of the m mode can be generally written as [141]:

$$\Delta\omega_m(T) = \Delta\omega_m^E(T) + \Delta\omega_m^A(T) + \Delta\omega_m^S(T) \tag{5.14}$$

where the first two terms are respectively related to the thermal expansion of the lattice and anharmonic effects, and the latter is relative to the effect of the strain caused by thermal expansion coefficient mismatch between the material and the supporting substrate.

The results obtained for the laser power-dependent Raman spectroscopy are shown in Figure 5.5 with a comparative inset related to the temperature-dependent Raman response.
The temperature dependence of Raman peak positions [142] can be described by the linear relation:

$$\Delta\omega(T) = \omega(T) - \omega_0 = \chi_T T \tag{5.15}$$

where $\omega(T)$ and ω_0 are the peak position at temperature T and room temperature, respectively, and χ_T is the first-order temperature coefficient.
In the case of the temperature-dependent study, performed by using a hotplate, it can be noticed that, for the considered temperature range, there are no significant variations in the thermal Raman response between the flat (green symbols) and top (blue symbols) regions of the wrinkle.

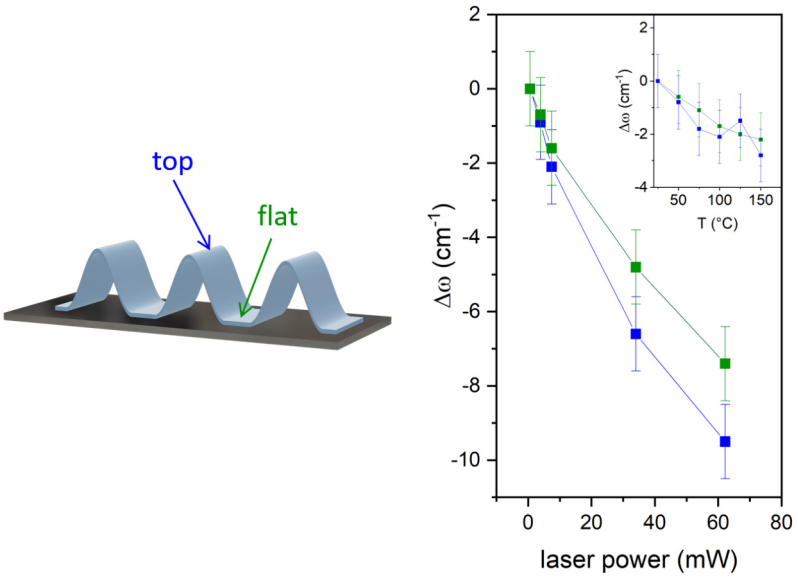

Figure 5.5: *Opto-thermal measurements of the Raman modes at the strained (top) and unstrained (flat) region of the wrinkled membrane. The measurements are carried out by varying the incident laser power in the range 0.5-60 mW. Inset: thermal measurements obtained by globally heating the sample on a hot plate in the range 25-150 °C.*

Both of them display a decreasing trend that, if linearly fitted, allows to calculate the temperature coefficient of the flat and top region, resulting

in:

$$\chi_T^{flat} \sim -0.018 \pm 0.002 \quad \frac{cm^{-1}}{^oC} \tag{5.16}$$

$$\chi_T^{top} \sim -0.019 \pm 0.005 \quad \frac{cm^{-1}}{^oC} \tag{5.17}$$

In analogy with the temperature measurements, the power dependence of the Raman peak positions can be described [139] by the linear relation:

$$\Delta\omega(P) = \omega(P) - \omega_0 = \chi_p P \tag{5.18}$$

where $\omega(P)$ and ω_0 are the peak position at power P and at the minimum laser power, respectively, and χ_p is the power coefficient. By linearly fitting the data trends it is possible to quantitatively assess the power coefficients of the two regions of the wrinkle, which turn out to be:

$$\chi_P^{flat} \sim -0.11 \pm 0.01 \quad \frac{cm^{-1}}{mW} \tag{5.19}$$

$$\chi_P^{top} \sim -0.15 \pm 0.01 \quad \frac{cm^{-1}}{mW} \tag{5.20}$$

It is hence possible to make a comparative study of the Raman responses acquired as a function of the change induced by two different methods, i.e., through hotplate and laser power. The maximum Raman shift has been obtained in the case of the laser power-dependent measurement and it demonstrates that the temperature induced in the material through laser heating with the highest power is higher than 150 ^oC. This result also stems from the fact that the laser-induced heating mechanism has a local nature, due to the spot size of ~ 1 µm, which inevitably creates a temperature gradient in the sample which is reflected in a different thermal conduction in strained (top) and unstrained (flat) regions.
The first-order coefficients obtained as a function of both temperature and laser power describe a redshift of the Raman frequency which can be interpreted as the sum of all contributions reported in the equation 5.14. These results represent a purely quantitative analysis, as the extrapolation of exclusively silicene-related parameters becomes complicated when dealing with this type of sample compared, for example, to the work carried out with exfoliated materials [143, 144, 145]. Nevertheless, they are one of the steps towards a more complete characterization of the properties of supported silicene.
A possible explanation for a strain-dependent thermal conductivity of silicene could be related to an enhancement of the acoustic phonon lifetime, which originates from the flattening of the buckled silicene structure

upon tensile strain [146, 147], although the strain values considered in this work are considerably lower.

5.3 Piezo-resistivity measurements

The last aspect is the integration of the Xenes membranes into the lithographic process flow. In particular, two different methods for realizing metal pads, in contact with the active silicene layers, have been tested: the first way to contact silicene is based on the realization of electrical contacts on the top surface by etching the Al_2O_3 layer, while the second approach is related to the exploitation of the silver layer as the metal to realize the contacts, after an appropriate transfer process of the sample. In the first case, it has been demonstrated that the sample can be patterned both at the beginning and at the end of the process flow described in Figure 3.4. Realizing the lithography process at the end of the membrane realization is possible thanks to the high resistance demonstrated for the PET substrate (see Fig. 3.5). But if the flexible substrate used is not sufficiently stable, the sample can be patterned before the membrane is realized, i.e., before the mica delamination, and then transferred on a substrate, as shown in Figure 5.6.

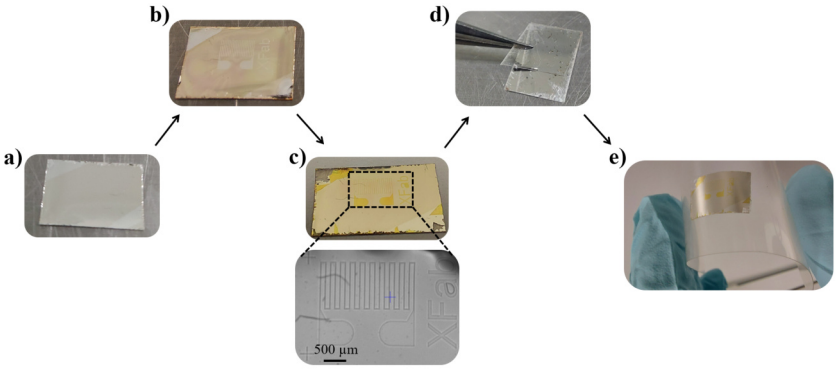

Figure 5.6: ***(a)*** *The sample is taken out of the vacuum and subsequently* ***(b)*** *patterned by means of optical lithography, thus obtaining* ***(c)*** *the electrical contacts after the metal deposition and subsequent lift-off, as for example a microheater or the XFab logo.* ***(d)*** *The sample is flipped for mica delamination through tweezers, and then* ***(e)*** *it is flipped again to be attached to an arbitrary substrate (a PET polymer in the photo).*

In Fig. 5.6b a microheater pattern has been printed through the optical lithography technique, followed by the Al_2O_3 etching, the evaporation of titanium and gold and the subsequent lift-off process (result shown in

Fig. 5.6c). After this step, it is possible to proceed with the mica delamination (Fig. 5.6d) realizing the flexible membrane with the pre-patterned sample (Fig. 5.6e).
To evaluate the durability of the flexible device, the patterned membranes have been wrapped around commonly used laboratory objects having a circular shape with a diameter in the range of 9-60 mm (see Figure 5.7a). By measuring each diameter it is possible to calculate an estimate of the resulting strain applied by using equation 5.1. The obtained values are in the same range as the strain applied through the three-point bending system, and the variation of the Raman peak position for the wrapped membranes (see Fig. 5.7b-c) is in good agreement with the previous bending tests, reported in Fig. 5.2.

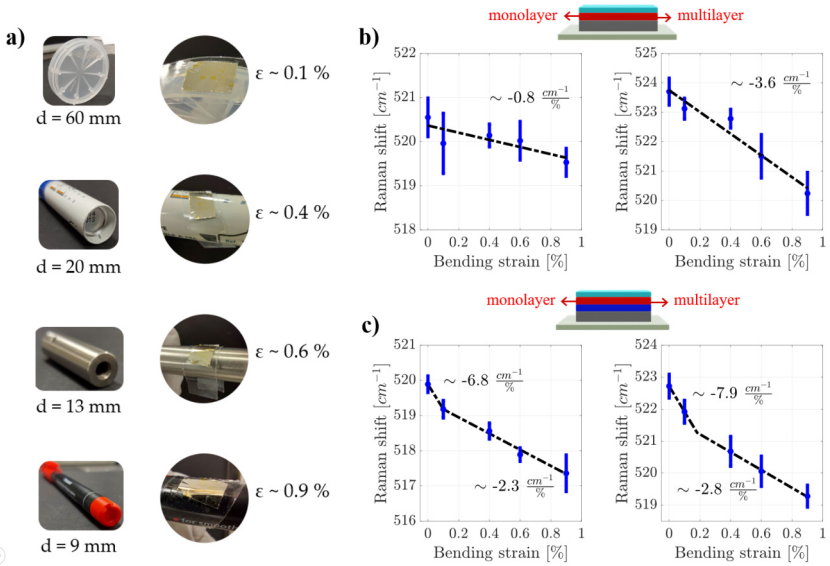

Figure 5.7: ***(a)*** *Images of the common lab objects used to wrap the membranes. Each object has a different diameter d associated with a different strain value ε. Evolution of the Raman peak position as a function of the applied strain induced by wrapping the membranes around the objects shown in (a), in the case of single and multilayer silicene without* ***(b)*** *and with* ***(c)*** *the stanene layer.*

All the silicene-based membranes have been wrapped up for several days without visible structural damages both to the sample surface and metal pattern, as confirmed by the Raman characterization reported in Fig. 5.8a. No variation in the mode intensity and frequency has been

detected over the entire temporal window and after the detachment from the objects. Moreover, all the tested samples have shown high repeatability of the strain-responsive behaviour, along with robustness against mechanical fractures over several bending cycles, showing a reversible shift of the Raman peak frequency within the experimental uncertainty.
When realizing a pattern on the top surface by etching the Al_2O_3 layer, it is possible to contact the Xenes stack, but performing planar transport measurements, for example, is almost impossible due to the presence of the underlying silver layer. This type of configuration is therefore especially useful for vertical configurations.
For this reason, a second approach, oriented to planar measurements, was also explored for the definition of the electrical contacts on the multilayer silicene-stanene heterostructure by using the fabrication process described in Fig. 3.9.

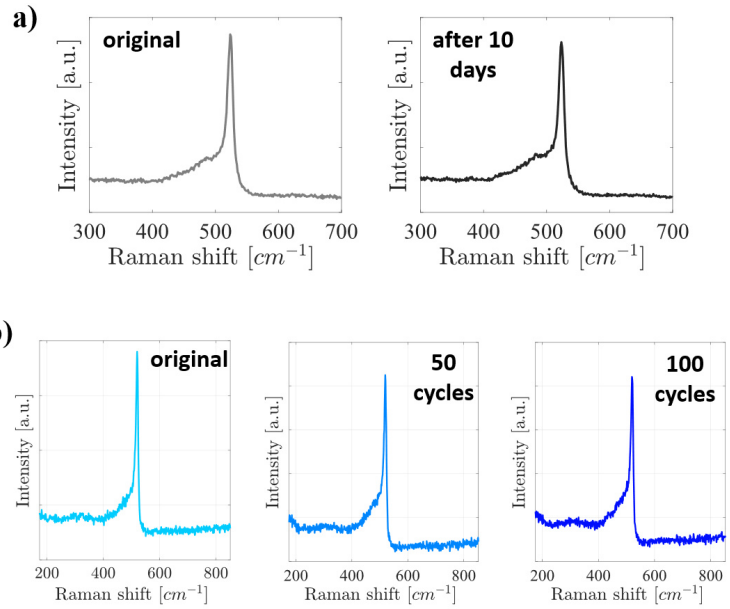

Figure 5.8: ***(a)*** *Raman characterization of the membrane before the processing and after ten days of being wrapped.* ***(b)*** *Raman peak position as a function of the number of bending cycles.*

The realized geometry is shown in the optical microscope image in Figure 5.9a. Specifically, the first circular image on the left shows the sample corresponding to the step described in Fig. 3.9e, while in the second image on the right it is possible to see the completed structure after the

channel realization (step shown in Fig. 3.9g). The channel length is $\sim$ 100 µm.
The so-obtained two-terminal passive device can be tested as a prototypical silicene piezoresistor, where the electrical planar resistance is measured as a function of the applied strain. Indeed, the piezoresistive effect describes the change of the electrical resistivity caused by a mechanical strain applied.
In order to combine the electrical characterization with the strain application, the sample has been mounted on a different setup through which it was possible to apply strain values in the range 0.4-0.6% (see Fig. 5.9b for the experimental setup photo and Fig. 5.9c for the bending method used). Specifically, one side of the sample was fixed to the structure and the other one was left free to move in a controlled manner by a calibrated screw, hence associating a strain value for a defined distance covered.

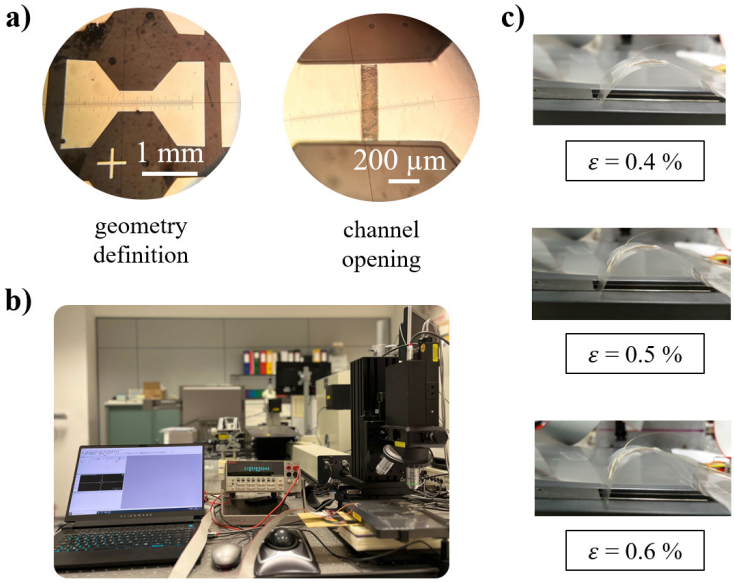

Figure 5.9: ***(a)*** *Optical images of the sample before and after the channel opening.* ***(b)*** *Photo of the experimental setup.* ***(c)*** *Pictures of the bent membrane through the new bending method.*

The electrical resistance measurements were carried out by means of a Keithley Model 2000 Multimeter controlled by using LabVIEW software. In Figure 5.10 the variation of the electrical resistance as a function time during a controlled sequence of bending cycles with different strain values. The initial value at zero strain of the resistance is $R_0 \sim$ 1.1 MΩ

and it is recovered after each bending cycle, thus demonstrating the repeatability of the piezo-resistive effect and the durability of the sample.

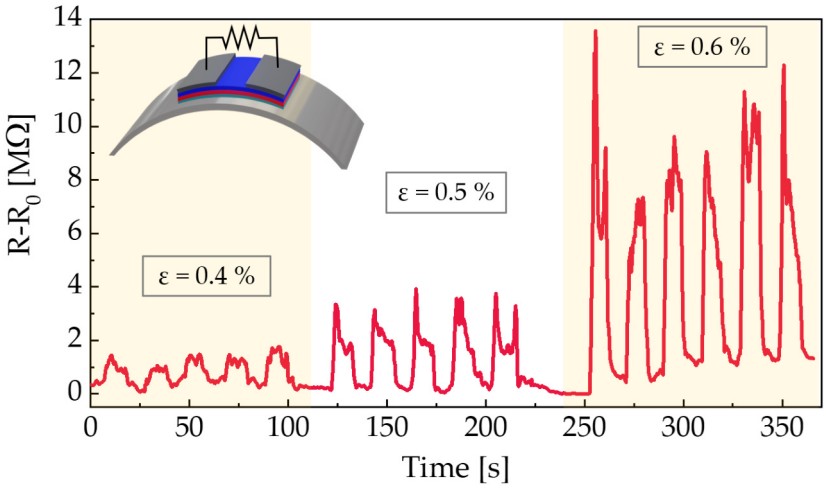

Figure 5.10: *Measurement of the electrical resistance of a two-terminal passive device obtained by using the optimized method reported in Fig. 3.9. Inset: a sketch of the sample.*

Chapter 6

Characterization of α-Sn on InSb

Alpha-tin (α-Sn) is one of the most promising and especially attractive candidates in the field of topological materials, due to the presence of its topological multiphases that are accessible by changing the material properties (such as thickness and strain) or by applying external electromagnetic fields.
In this work, as introduced in Sec. 1.2.2, samples of few-layer stanene grown on InSb(111) substrate allow us to investigate a different configuration in which the Xene layer is grown directly on a semiconductive substrate compared to a metallic one. In this case, therefore, it is possible to characterize the Xene directly, without a specific transfer process.

6.1 Topological properties

As mentioned in Subsec. 1.2.2, tin has a large atomic number if compared with silicon and germanium. This characteristic is reflected in an intense contribution of the spin-orbit coupling (SOC) term that causes not only the splitting of the valence band into light hole (LH) and heavy hole band (HH) bands, but also generates the inversion of LH and conduction bands [148, 149].
Bulk α-Sn is actually a semimetal with a zero-gap protected by the cubic symmetry of its crystal lattice and its topological character could emerge only if this symmetry is broken. One way to break the symmetry is to apply a strain that can be induced by the substrate on which tin is grown, in order to open a gap in the band structure, as shown in Figure 6.1. The

application of a strain, in fact, corresponds to applying a deformation to the material that changes the geometrical structure of the crystal, which is then reflected in a change in the electronic band structure and in a tuning of its physical properties.

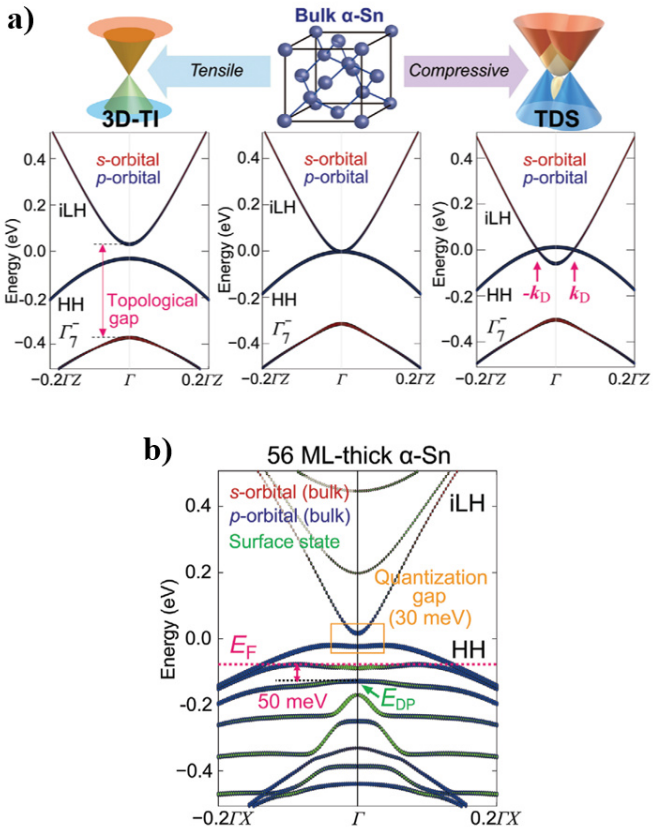

Figure 6.1: ***(a)*** *Calculated band structure for bulk α-Sn, in the case of tensile and compressive strain.* ***(b)*** *Calculated band structure of 56 ML-thick α-Sn under an in-plane compressive strain. Adapted from Ref. [149].*

As reported in Ref. [149], in the case of a resulting compressive strain, bulk α-Sn turns out to be a 3D topological Dirac semimetal (TDS), while with a resulting tensile strain, it turns into a 3D topological insulator (TI), thus obtaining, respectively, a negative or positive energy gap, depending on the experienced strain (Fig. 6.1a).
In particular, the TDSs group represents the 3D counterpart of the characteristic band structure of graphene that would potentially allow to obtain electrons with similar mobility or unusual properties [150]. On the other

hand, the TIs class is characterized by the simultaneous presence of an insulating behaviour in the bulk and a conductive one on the surface which lead to non-dissipative currents [151].
Specifically, their surface shows a Dirac-like band structure characterized by a linear dispersion and spin-momentum locking enabling surface polarization. Such a band structure, in a 2D material, leads to the formation of topological surface states (TSS) which cause the current to flow only on the material interfaces, avoiding the remaining part that will be insulating. Since the current is limited to the film surface, it is possible to get high conductivity and full spin-polarization without dissipation in the bulk. In this respect, it is interesting to point out that a crossover between TDS and TI is possible by exploiting quantum confinement resulting from the thickness reduction of a 3D TDS to the 2D limit (as reported, for example, in Fig. 6.1b).
In the present work, as described in Sec. 3.2, the α-Sn is grown through MBE on undoped indium antimonide InSb(111) substrate. According to previous works [74], the mismatch between the lattice parameter of Sn ($a_{Sn} = 6.489$ Å [152]) and that of InSb ($a_{InSb} = 6.479$ Å [153]) causes an in-plane compressive strain of about $\varepsilon_{\parallel} \sim -0.14\%$.

6.2 Electrical transport measurements

A first set of measurements was performed at the University of Milano-Bicocca. In order to perform the electrical transport measurements, it is necessary to realize a defined Sn structure and contact the material by realizing the metal pads. First of all, the tin was etched through the procedure described in Subsec. 3.2.1, and subsequently the pads pattern was realized by means of a second lithography step aligned on the previous structure.
These samples were patterned using the mask aligner system that allows, through the negative lithography, to completely etch the surrounding Sn regions. The samples belonging to this group had different Sn thicknesses (5 nm, 10 nm and 20 nm) and a single-channel structure that was contacted directly through metal tips.
A microscope cryostat (Linkam HFS600E-PB4) has been used to study the resistance trend as a function of temperature. It includes two metal cryogenic tips that can be manually placed on the sample to make electrical contact. These are connected to a Keithley Source-Meter-Unit 2450, through which the voltage-current curve data can be recorded. The cryostat is cooled with liquid nitrogen and connected to the PC through software to control the temperature.
The samples have been analyzed by measuring the current-voltage (I-V)

curves at different temperatures values between 77 K and 300 K, and the R(T) trend obtained is illustrated in Figure 6.2a. By measuring R(T), it is possible to calculate the energy gap value induced by the strain in the α-Sn films. As reported in literature [154, 155], the curve can be fitted with two different models, respectively.

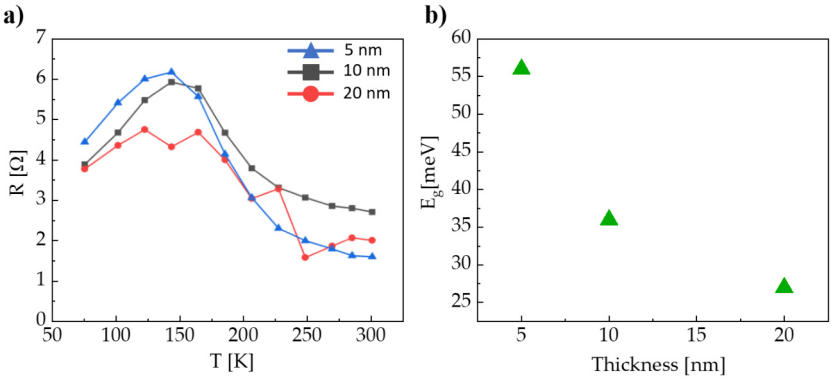

Figure 6.2: ***(a)*** *R(T) curves obtained for α-Sn samples with a thickness of 5 nm (blue curve), 10 nm (black curve) and 20 nm (red curve).* ***(b)*** *Evolution of the centre-zone energy gap as a function of Sn film thickness. Adapted from Ref. [156].*

At higher temperatures, the trend can be described by the Arrhenius model, given by:

$$R_{semi}(T) = R_{\infty} e^{E_g / K_B T} \tag{6.1}$$

where K_B is the Boltzmann constant, R_{∞} is the resistance at high temperature, and E_g is the energy gap. At lower temperatures, the behaviour is well described by the Bloch-Grüneisen model, given by the equation:

$$\frac{1}{R_{metal}(T) - R_0} = \frac{1}{C_1 T^5} + \frac{1}{C_2 T} \tag{6.2}$$

where C_1 and C_2 are related to the prevalence of electron–phonon interactions and the geometry of the Hall bar-like structure, while R_0 is the resistance at T = 0 related to the defects scattering.
As the temperature decreases, the ohmic resistance increases exponentially as in the case of semiconductor [157], while for low temperatures it shows a metallic character. Hence, by approximating the system as a metallic channel in parallel with a semiconductive one, the resulting

resistance can be written as [154, 155]:

$$\frac{1}{R(T)} = \frac{1}{R_{semi}(T)} + \frac{1}{R_{metal}(T)} \tag{6.3}$$

Using this approach [154], it is interesting to note that the expected trend for a 3D metal is described by a T^5 scaling whereas in the case of a 2D metal, the T^4 scaling is more suitable [158]. Therefore, to understand which transport channel is dominant in the material, it is necessary to understand which trend best fits the curve of the experimental data for low temperatures.
Each R(T) curve has been fitted with both models and the results are shown in Table 6.1.

Thickness [nm]	E_g with T^4 [meV]	E_g with T^5 [meV]
5	56	58
10	36	28
20	27	26

Table 6.1: *Energy gap values obtained for the two fits (with T^4 and T^5) as a function of the α-Sn film thickness. Adapted from [156].*

Comparing the chi-square (χ^2) values obtained for both trends for each sample, the T^4 scaling was suitable only for the 5 nm thick sample, while for the remaining samples, no relevant differences were shown in the two distinct interpolations. For this reason, it is possible to state that for the 5 nm thick sample, in the low-temperature region, there is 2D metal behaviour.
As can be seen, the energy gap value increases with decreasing the film thickness and this is in agreement with what is expected from quantum confinement [154, 159].

6.2.1 Magnetotransport measurements

A second set of samples was used to carry out magnetotransport measurements, thanks to the internal collaboration with Dr. Roberto Mantovan.
In this case some of the initial samples were patterned using the mask aligner system, while the subsequent samples were patterned using the maskless lithography. Figure 6.3a shows the pattern of a mask used in the case of a Hall bar design and Fig.6.3 b shows an optical image of

the sample after the Sn etching. The maskless technique allows to be more versatile as one can define the best geometry needed but, in this case, performing isolation trenches (as shown in Fig. 6.3c) can be less time-consuming. Given to the employed setup, the samples have to be bonded to a chip carrier (see Fig. 6.3d) by using a thermocompression bonding machine with aluminium wire.

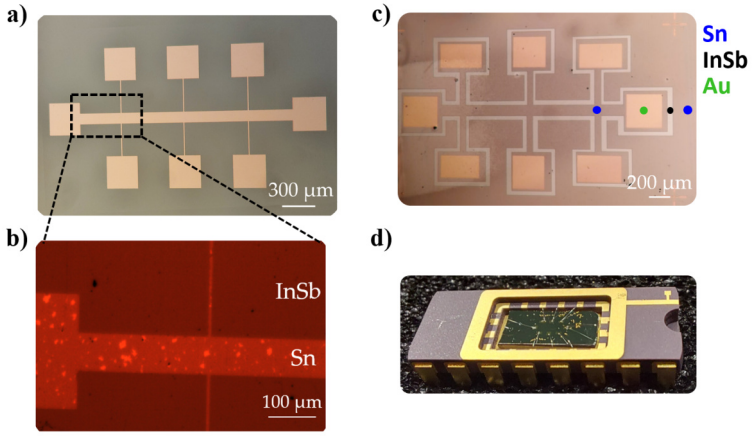

Figure 6.3: ***(a)*** *Optical image of the chrome photo-mask.* ***(b)*** *Optical image of the sample after the Sn etching.* ***(c)*** *Optical image of a sample patterned through maskless lithography, after the Sn etching in the isolation trench.* ***(d)*** *Sample of panel (c) mounted on a chip carrier and bonded to it.*

The experiments were performed in the Hall configuration, in the 5-295 K temperature range. An external magnetic field up to 0.8 T was applied in different directions with respect to the sample plane. As can be seen in Figure 6.4a, θ is the angle between the magnetic field and the sample surface, therefore θ=0° denotes a magnetic field applied parallel to the sample plane, while θ=90° corresponds to directing the field perpendicular to the surface.

It is necessary to point out that, after the Hall bar and contacts realization, the samples had to be cleaved into a rectangular shape to fit the chip carrier. The difficulties arising from the (111) orientation of the substrate in addition to the small size of the employed chip carrier (6 mm × 4 mm) made this type of characterization challenging from the point of view of measurement feasibility.

First of all, single-channel resistance as a function of temperature was measured using geometry conditions similar to those used for the previous experiments and the result for a 10 nm thick α-Sn is shown in Fig. 6.4b. It is possible to note that the trend shown in the Fig. 6.2a is

confirmed also for a different experimental setup.
Subsequently, the transport as a function of the applied external magnetic field has been studied. In particular, the magnetoresistance (MR) of a material quantify the variation of its electrical resistance in an externally-applied magnetic field B and can be expressed as:

$$MR\%(B,T) = \frac{R(B,T) - R(B=0,T)}{R(B=0,T)} \cdot 100\% \tag{6.4}$$

Figure 6.4c shows the magnetic field dependence of the MR for different field orientations, measured at T=6 K, while Figure 6.4d shows the MR as a function of the in-plane field, for different temperature values. Both the measurements refer to the 10 nm thick α-Sn sample.

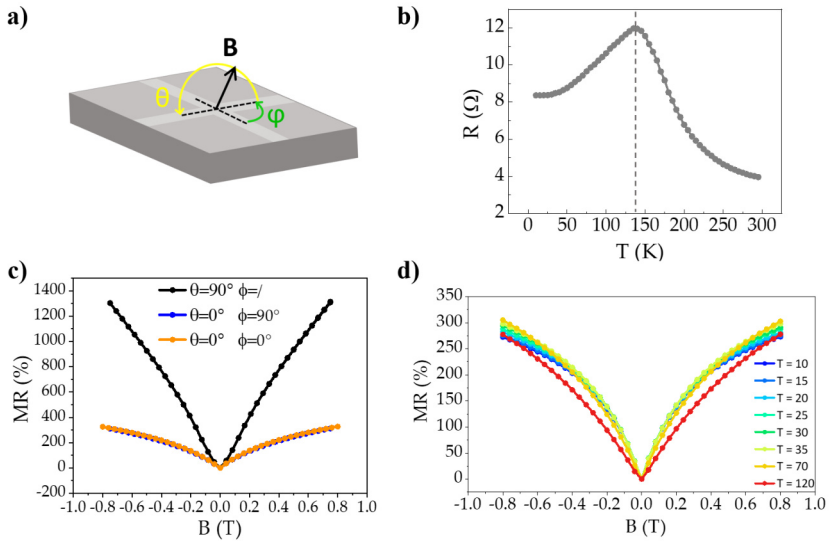

Figure 6.4: ***(a)*** *Sketch of the measurement geometry.* ***(b)*** *Measurements of electrical resistance as a function of temperature (without applying the magnetic field).* ***(c)*** *Measurement of magnetoresistance as a function of an in-plane (blue and orange traces) and out-of-plane (black trace) magnetic field B, measured at T = 6 K.* ***(d)*** *Magnetoresistance as a function of the in-plane magnetic field B, for different temperatures (from 10 to 120 K).*

The out-of-plane MR turns out to be larger than the in-plane one, in agreement with results already reported [160, 149], although the values obtained proved to be an order of magnitude lower. This discrepancy in the results can be attributed to inhomogeneities within the α-Sn in the examined sample.

6.3 Magneto-optical spectroscopy measurements

Experiments with high magnetic fields are useful for identifying the band structure of the materials, for example through the analysis of the optical transitions between different Landau levels. Moreover, they represent a contactless technique, requiring no sample preparation, to gain access to the topological surface states because, by applying a strong magnetic field, it is possible to break the time-reversal symmetry from which they are topologically protected. For these reasons, we performed low-temperature magneto-spectroscopy measurements in the Laboratoire National des Champs Magnetiques Intenses (LNCMI) in Grenoble (France), with the group of Dr. Milan Orlita. The three samples used for the measurements are shown in Table 6.2.

Thickness [nm]	T (growth) [°C]	t (growth) [min]	Rate [Å/min]
10	RT	50	2
20	RT	100	2
50	RT	250	2

Table 6.2: *Summary table of samples measured by magneto-optical spectroscopy. For each one, the thickness, growth temperature, growth duration and deposition rate are reported.*

A picture and the sketch of the experimental setup is shown in Figures 6.5a-b. A Globar has been used as a broadband source of infrared radiation and the experiments were performed at the temperature of 4.2 K in the Faraday configuration, which corresponds to the magnetic field perpendicular to the light wavevector. The available magnetic field ranged from 0 to 16 T and was delivered by a superconducting solenoid (Oxford Instruments).
The sample and the bolometer were placed in a sealed probe kept under low pressure, ensuring sufficient heat transfer with the helium bath of the magnet cryostat. The radiation, analyzed through a Fourier transform spectrometer, was guided to the entrance window of the probe and detected by the bolometer under the sample.
During magneto-transmission measurements, by increasing the magnetic field intensity of well-defined steps, it is measured the amount of light that is transmitted through the material as a function of the radiation energy. In order to study the effects induced by the magnetic

field, all the collected spectra at B≠0 are normalized to the response at B=0. Some of the individual recorded spectra from 10 nm-thick sample are plotted in Figure 6.6a, together with their corresponding derivatives with respect to the magnetic field B (Fig. 6.6b). For clarity, the spectra are vertically stacked, with the offset scaling linearly with B.

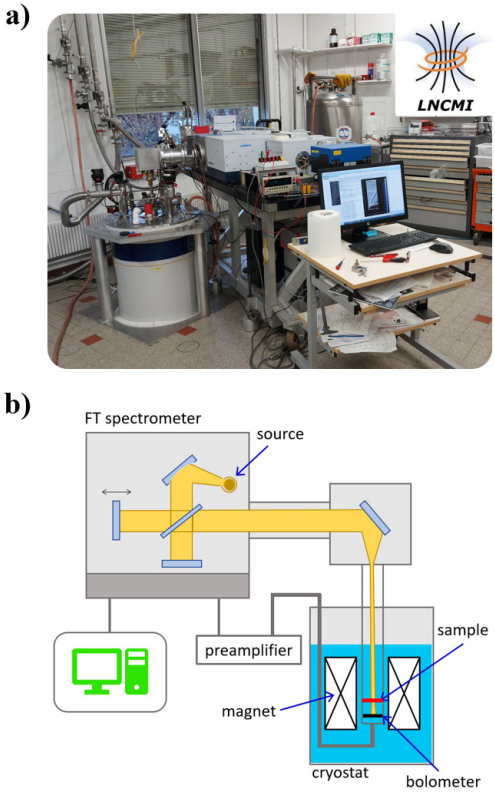

Figure 6.5: ***(a)****Picture of the setup used for magneto-optical measurements, at the LNCMI laboratories in Grenoble.* ***(b)*** *Sketch of the experimental apparatus.*

The three grey areas correspond to regions of no signal, respectively due to: a low signal-to-noise ratio (area 1), a spectral region fully opaque caused by the reststrahlen band of InSb [161] (area 2) and absorption inside the beamsplitter (area 3). Specifically, the reststrahlen effect is a reflectance phenomenon in which the electromagnetic radiation within a narrow energy band cannot propagate within the material due to a change in the refractive index combined with the material-specific absorption band.

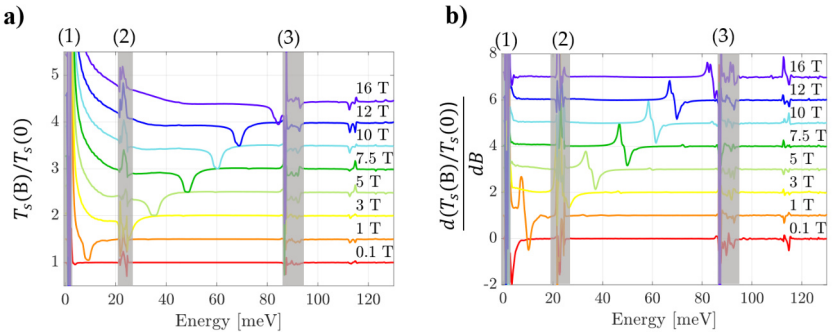

Figure 6.6: ***(a)*** *Low-temperature magneto-transmission spectra collected from sample 10 nm-thick sample and* ***(b)*** *their respective derivatives. The grey areas (1) correspond to the spectral regions where due to the low intensity of the radiation source there is no sufficiently high signal-to-noise ratio, while (2) and (3) areas correspond respectively to the spectral region fully opaque due to the reststrahlen band of InSb and absorption in the beamsplitter.*

The collected spectra are often plotted together with the first or second derivative with respect to the magnetic field or energy, in order to better identify the positions of the different resonances.
For each sample in Table 6.2, the measured magneto-optical spectra and the corresponding derivative with respect to the magnetic field are presented in the form of false-color maps in Figure 6.7.
The resonances observed are relatively narrow, hence the observed minima can be directly associated with the positions of the resonances. The magneto-transmission responses exhibit different transitions which unfortunately were found to be related to the impurities in the InSb substrate. As shown in Fig. 6.8, by repeating a high-resolution measurement for the substrate only, the same features found in the α-Sn on InSb samples were obtained.
The energy gap value of InSb as a function of the temperature [162] is given by:

$$E_g^{InSb}(T) = \frac{0.24 - 6 \cdot 10^{-4} T^2}{T + 500} \tag{6.5}$$

and leads to an energy gap of E_g = 230 meV at T = 4.2 K. For this reason, the observed transitions in the 0-100 meV energy range may be related either to defects or to intraband transitions. The InSb(111) substrate is therefore not suitable for performing this type of measurement, as the large contribution from the substrate may hide the behaviour related to

the α-Sn.

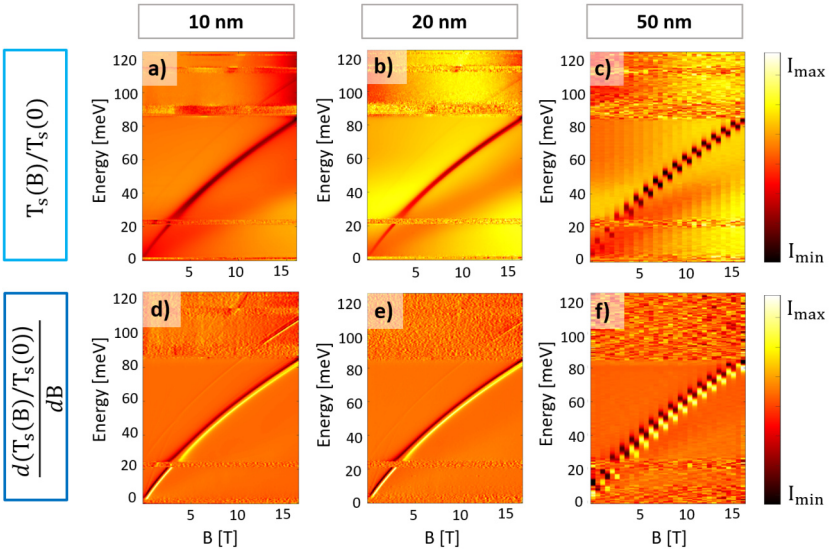

Figure 6.7: *Magneto-transmission spectra of the three samples.* ***(a-c)*** *Relative magneto-transmission T(B)/T(0), measured in the Faraday configuration, of α-Sn samples with thicknesses of 10 nm, 20 nm and 50 nm, respectively.* ***(d-f)*** *Derivative of T(B)/T(0) with respect to the field B.*

However, in spite of the strong substrate response, by closely looking at the collected spectra of Figures 6.7a-c, it is possible to identify a linear trend below the most intense parabolic resonance that correspond to the α-Sn cyclotron resonance line. For this reason, to reduce the contribution of the substrate, it is worth to divide the sample response $\frac{T_s(B)}{T_s(0)}$ by the substrate reference response $\frac{T_r(B)}{T_r(0)}$. For this purpose, further measurements were carried out on the samples and the substrate, using the same parameters and magnetic field steps, so that the two responses could be compared.
The obtained result are shown in Figures 6.9a-c. In this way, as evidenced by the white dotted line in the Figures, the cyclotron resonance line becomes more evident and easily identifiable, especially in the case of the 10 nm-thick sample.
In the cyclotron resonance condition, the maximum energy will be absorbed by the charged particle, resulting in the presence of a dip in the transmitted spectrum. Therefore, by calculating the positions of dips it is possible to have an estimate of the effective mass value of the material.

The individual spectra of 10 nm-thivk sample normalized for the substrate response are shown in Figure 6.10a, highlighting with a red circle the dip position in the spectra. These positions can be linearly fitted to calculate the effective mass of the α-Sn, as reported in Figure 6.10b.

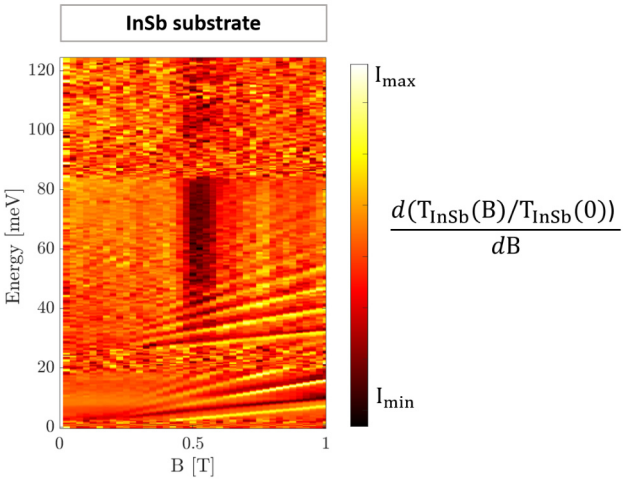

Figure 6.8: *Color map of the derivative of the magneto-transmission spectra with respect to the magnetic field B for the InSb substrate.*

Indeed, the cyclotron frequency turns out to be equal to:

$$f_c = \frac{eB}{2\pi m^* c} \tag{6.6}$$

then by calculating the slope of the linear fit, it is possible to directly derive the effective mass m^* of α-Sn. In the case of 10 nm-thick sample, I obtained a slope of $(7.61 \pm 0.07) \cdot 10^7$ esu g^{-1} cm^{-1} s, thus resulting in an effective mass of:

$$m^*_{\alpha\text{-}Sn} \sim 0.036\ m_e. \tag{6.7}$$

which is consistent with a Dirac dispersion, leading to high mobility. The value obtained is lower than the effective mass values reported in the literature for other Dirac semimetals [163, 164] and being a monoelemental material, the α-Sn advantage also lies in its easier growth.
Although this result represents the first estimate of the effective mass value for 10 nm thick α-Sn grown on InSb(111), the calculated value is in line with the results observed in the case of α-Sn grown on CdTe(001) [165] and on InSb(001) [160] substrate.
As can be seen in Figures 6.9b and c, the cyclotron resonance line becomes weaker and not well defined in the case of samples with higher

Sn thicknesses. In general, these resonance spectra are not easily distinguishable as they present very broad structures and it is challenging to isolate them from the background.

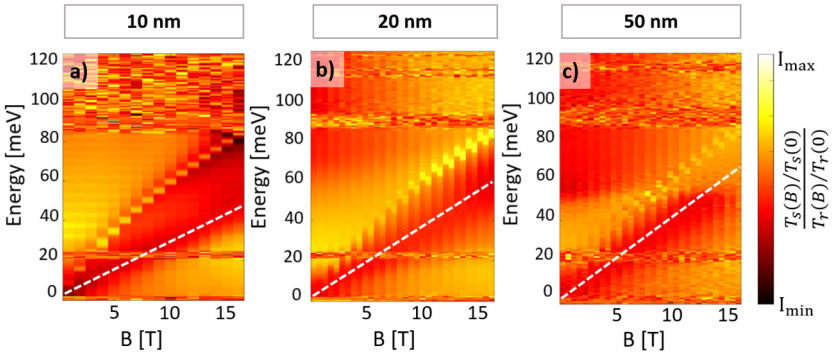

Figure 6.9: *Magneto-transmission color map of the* ***(a)*** *10 nm sample,* ***(b)*** *20 nm sample and* ***(c)*** *50 nm sample. The white dotted line highlights the cyclotron resonance line.*

Although the positions of the dips in the spectra of 20 nm- and 50 nm-thick samples could not be identified, the slope of the resonance lines appears to increase as the thickness of the Sn increases. Since the effective mass is inversely proportional to the slope, this provides qualitative evidence that the effect of quantum confinement is to increase the effective mass of the material.

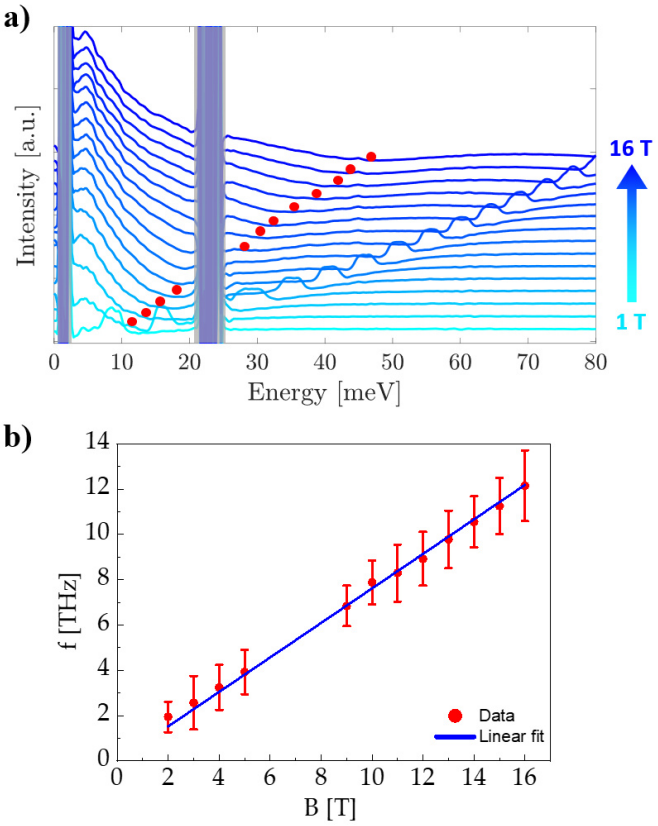

Figure 6.10: ***(a)*** *The relative transmission spectra of 10 nm-thick sample (vertically stacked for clarity) in magnetic field from 1 to 16 T. Red dots indicate the position of the dip.* ***(b)*** *Linear fit of the positions of the cyclotron resonance frequencies as a function of the magnetic field B.*

Conclusions and perspectives

The discovery of graphene has triggered the 2D materials research field giving rise to the Xenes family and generating interest in the investigation of their electronic, optical and mechanical properties. However, the path towards a technological implementation perspective is hindered by synthesis and integration issues.
In a perspective shared by other 2D materials [166, 167], as introduced in Chapter 1, this thesis work is oriented towards the investigation of the actual manipulation and processing of different Xenes configurations, by means of the techniques presented in Chapter 2. Specifically, silicene on Ag(111) has been considered as a paradigmatic case of Xene grown on a metal substrate, while stanene on InSb(111) represented a comparative example of Xene grown on semiconductive substrate. The first one has been used to implement new transfer and process schemes for the stabilization of Xenes under environmental conditions and integration into device architecture. The second one has been considered as a possible option allowing for direct access to the Xene functionalities, such as theoretically-predicted topological properties.
In this context, the achieved results are summarized as follows:

- ✓ defining processing steps to achieve a scalable procedure for patterning and integrating samples of silicene and its heterostructures;
- ✓ testing a possible solution for stabilizing silicene when transferred from the native substrate;
- ✓ obtaining deformable silicene-based membranes that allow one to investigate the strain-induced effects;
- ✓ realize a first prototype silicene-based piezoresistor;

- ✓ directly characterize few-layer stanene demonstrating effects related to quantum confinement.

In order to have access to device fabrication and characterization of the material, it is necessary to test and establish protocols that enable a full manipulation of the material.
To this end, as described in Chapter 3, I developed and optimized different processing procedures that make it possible to solve some of the critical issues, such as Xenes transfer to device structures. Unlike graphene, the mixed sp^2-sp^3 hybridization of Xenes, and in particular of silicene, results in a high environmental reactivity leading to the material degradation. For this reason, a key role in this work is related to the vertically stacked silicene-stanene heterostructures, where silicene is sandwiched in between an Al_2O_3 capping layer on the top surface and the stanene on Ag(111) crystal at the bottom face [11].
As discussed in Chapter 4, the introduction of a stanene buffer layer enabled us to develop an all-around encapsulation scheme to protect silicene against degradation under environmental conditions when disassembled from the native substrate. Moreover, a full 2D encapsulation scheme, where the top and bottom faces of silicene are protected by 2D tin layers, gives rise to an atomically thin Xene stack, demonstrating a long-standing silicene durability. The all-around encapsulation constitutes an advancement for the silicene stability and paves the way for further exploitation of silicene and other Xenes in flexible and wearable electronics.

With this purpose, in addition to the stability result, this type of samples was compared with only-silicene sample from the point of view of the effects induced by macro- and micro-scale strain applied. As detailed in Chapter 5, starting from epitaxial single and multilayer silicene grown on Ag(111) or in the heterostructure configuration, it is possible to realize bendable silicene-based membranes which allows us to study the strain response of the Xene stack. Specifically, it has been demonstrated how the stanene layer, in addition to decreasing the electronic interaction between silicene and Ag substrate, also enhances the mechanical transfer of the applied strain. The multilayer silicene in the heterostructure scheme turned out to have the largest strain responsitivity, thus representing a promising candidate for applications in flexible electronics. The presented process flow can also be extended to the entire class of the epitaxial Xenes and especially applicable to the case of the Ag-supported ones, like borophene, antimonene and bismuthene [168, 169, 170].

As the choice of substrate determines the direction of both the process

and the possible application, few-layer stanene grown on a semiconductive substrate was also taken into consideration for scrutinize path for the development of device mechanisms based on the non-trivial topological character of stanene. This type of growth substrate facilitates the process steps, as no specific transfer process is required to have access to material properties. The characterizations performed on these samples, which have been presented in Chapter 6, include transport and magneto-transport measurements, and the magneto-optical transmission response investigation. The transport analysis allowed us to derive the energy gap value as a function of the film thickness, confirming the effects of quantum confinement. Magneto-optical measurements, carried out using intense magnetic fields showed a significant contribution from the InSb substrate itself, which did not allow the observation of α-Sn related features. At the same time, however, through the detected resonance line, it was possible to calculate the first estimate of the effective mass of α-Sn grown on InSb(111).

In light of the achieved results, however, there are some ongoing improvements and additional future solutions to be taken into account that are summarized as follows:

- ◇ the control of the 2D materials etching through a wet etching process is truly challenging. When working with ultra-thin materials, it is impossible to achieve such a high degree of control. A possible alternative is the use of dry etching by means of dedicated tools such as Reactive Ion Etching (RIE) or Inductively Coupled Plasma-Reactive Ion Etching (ICP-RIE). These techniques relie on different processes to remove the material, such as chemical reactions, physical removal or a combination of these two, that allow us to obtain uniform etching, atomic-scale selectivity and anisotropy when required;

- ◇ in order to facilitate the processes and overcome the Xenes interaction with the native substrate, the growth of silicene on insulating substrates, such as sapphire, should be considered and improved [171];

- ◇ to understand whether the native substrate is a valid solution for contacting Xenes, by scaling the dimensions of the channels, it would be possible to have an estimate of the contact resistance between the Ag(111) and the Xene layers;

- ◇ to realize a stable field-effect transistor architecture through the silicene-stanene heterostructure scheme, the patterned structures

have to be optimized so as to test either a back-gated geometry or the ionic liquid top gating configuration [172];

- ◇ exploring other suitable substrates for stanene growth that enables to reveal and exploit the topological properties of the material.

In conclusion, considering broader perspectives, the achieved results will enable to assess silicene and stanene fundamental properties in relation to other 2D materials and allow for a potential extension of the developed procedures to other Xenes and heterostructures still unexplored.

Appendix A

Procedures for silicene sample processing

As presented in Chapter 3, the realization of silicene-based devices depends mainly on the mica delamination step. In this Appendix, some of the attempts obtained with the previous methods are shown together with the more recent results obtained through the optimized process described in Fig. 3.9.
Figures A.1a-c show images of the surface of three samples, after the mechanical mica removal, that exhibit an increasing level of silver surface roughness which inevitably affects the subsequent patterning and etching steps.

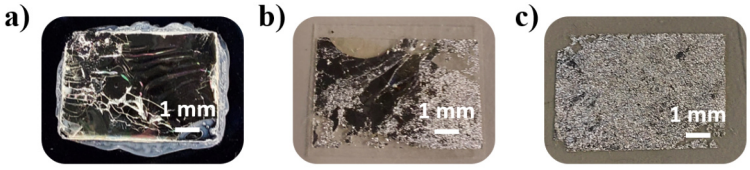

Figure A.1: ***(a)***, ***(b)*** *and* ***(c)*** *show three resulting samples with increasing levels of silver roughness after mica delamination.*

The use of these samples for device definition necessarily implies the identification, for example by SEM, of more homogeneous regions of silver on which to make the desired pattern, greatly complicating the entire fabrication process.
Figures A.2a-c show further details of the inhomogeneous silver surface.

As can be seen from Fig. A.2b, the detachment of the mica in most cases is not complete and requires additional scotch tape peelings that further compromise the underlying silver layer.

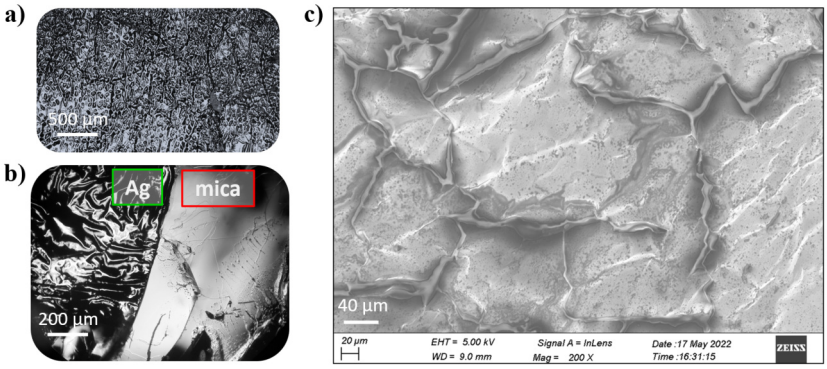

Figure A.2: ***(a)*** *Picture of Ag surface after completed mica delamination.* ***(b)*** *Optical image of the sample surface during mica delamination.* ***(c)*** *SEM image of the rough silver surface.*

Figure A.3 shows the results obtained through the new optimized process in the case of the most recent samples. In particular, Figures A.3a-b present a geometry characterized by several two-terminal passive devices that share a common pad which is useful in performing preliminary electrical measurements using metal tips. Figures A.3c-d report further details of the structure realized with easier geometry after the channel etching.
The results achieved show a much more homogenous silver surface, compared to previous cases, although some impurities and defects remain, mainly related to the use of the adhesive layer underneath.

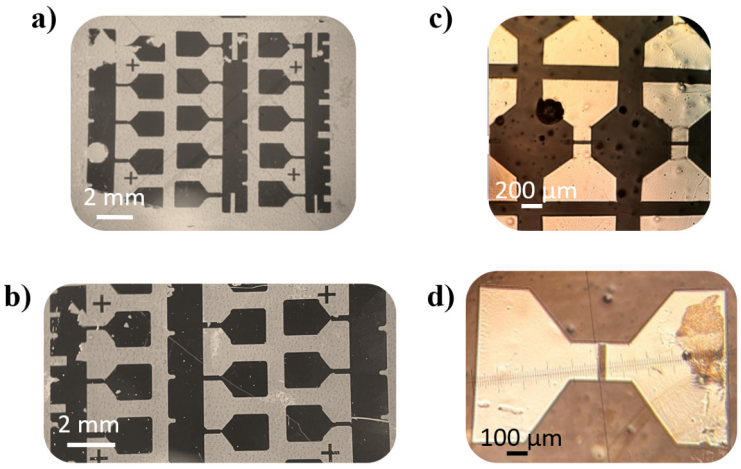

Figure A.3: ***(a)-(b)*** *Results obtained in the most recent samples by means of the optimized method (before channels definition).* ***(c)-(d)*** *Optical images of examples of pre-patterned structures after channel etching.*

Bibliography

[1] K. S. Novoselov, A. K. Geim, S. V. Morozov, D. Jiang, Y. Zhang, S. V. Dubonos, I. V. Grigorieva, and A. A. Firsov, "Electric field effect in atomically thin carbon films.," *Science (New York, N.Y.)*, vol. 306, no. 5696, pp. 666–669, 2004. *(Cited on pages 1, 3, 4, and 8)*

[2] C. Berger, Z. Song, T. Li, X. Li, A. Y. Ogbazghi, R. Feng, Z. Dai, A. N. Marchenkov, E. H. Conrad, P. N. First, and W. A. de Heer, "Ultrathin Epitaxial Graphite: 2D Electron Gas Properties and a Route toward Graphene-based Nanoelectronics," *The Journal of Physical Chemistry B*, vol. 108, no. 52, pp. 19912–19916, 2004. *(Cited on page 1)*

[3] K. S. Novoselov, A. Mishchenko, A. Carvalho, and A. H. Castro Neto, "2D materials and van der Waals heterostructures," *Science*, vol. 353, no. 6298, p. aac9439, 2016. *(Cited on page 1)*

[4] Y. Feng, F. Wang, Z. Yang, and J. Wang, "Two dimensional hexagonal boron nitride (2D-hBN): Synthesis, properties and applications," *Journal of Materials Chemistry C*, vol. 5, 2017. *(Cited on page 1)*

[5] D. Lembke, S. Bertolazzi, and A. Kis, "Single-Layer MoS2 Electronics," *Accounts of Chemical Research*, vol. 48, no. 1, pp. 100–110, 2015. *(Cited on page 1)*

[6] A. Castellanos-Gomez, L. Vicarelli, E. Prada, J. Island, K. Narasimha-Acharya, S. Blanter, D. Groenendijk, M. Buscema, G. Steele, J. Alvarez, H. Zandbergen, J. Palacios, and H. Zant, "Isolation and characterization of few-layer black phosphorus," *2D Materials*, vol. 1, p. 25001, 2014. *(Cited on page 1)*

[7] G. J. Orchin, D. De Fazio, A. Di Bernardo, M. Hamer, D. Yoon, A. R. Cadore, I. Goykhman, K. Watanabe, T. Taniguchi, J. W. A. Robinson, R. V. Gorbachev, A. C. Ferrari, and R. H. Hadfield,

"Niobium diselenide superconducting photodetectors," *Applied Physics Letters*, vol. 114, no. 25, p. 251103, 2019. *(Cited on page 1)*

[8] C. Grazianetti and C. Martella, "The Rise of the Xenes: From the Synthesis to the Integration Processes for Electronics and Photonics," *Materials*, vol. 14, no. 15, 2021. *(Cited on pages 1 and 7)*

[9] A. Molle, J. Goldberger, M. Houssa, Y. Xu, S. C. Zhang, and D. Akinwande, "Buckled two-dimensional Xene sheets," *Nature Materials*, vol. 16, no. 2, pp. 163–169, 2017. *(Cited on page 1)*

[10] A. Molle, G. Faraone, A. Lamperti, D. Chiappe, E. Cinquanta, C. Martella, E. Bonera, E. Scalise, and C. Grazianetti, "Stability and universal encapsulation of epitaxial Xenes," *Faraday Discussions*, vol. 227, pp. 171–183, 2021. *(Cited on pages 2, 13, 31, 45, and 51)*

[11] D. S. Dhungana, C. Grazianetti, C. Martella, S. Achilli, G. Fratesi, and A. Molle, "Two-Dimensional Silicene–Stanene Heterostructures by Epitaxy," *Advanced Functional Materials*, vol. 31, no. 30, p. 2102797, 2021. *(Cited on pages 2, 10, 51, 52, 62, and 88)*

[12] S. Gupta, W. T. Navaraj, L. Lorenzelli, and R. Dahiya, "Ultra-thin chips for high-performance flexible electronics," *npj Flexible Electronics*, vol. 2, no. 1, p. 8, 2018. *(Cited on pages 2, 13, 34, and 55)*

[13] D. Akinwande, N. Petrone, and J. Hone, "Two-dimensional flexible nanoelectronics," *Nature Communications*, vol. 5, no. 1, p. 5678, 2014. *(Cited on pages 2 and 55)*

[14] T. Liu, S. Liu, K.-H. Tu, H. Schmidt, L. Chu, D. Xiang, J. Martin, G. Eda, C. A. Ross, and S. Garaj, "Crested two-dimensional transistors," *Nature Nanotechnology*, vol. 14, no. 3, pp. 223–226, 2019. *(Cited on pages 3 and 55)*

[15] H. Peelaers and C. G. Van de Walle, "Effects of strain on band structure and effective masses in MoS2," *Physical Review B*, vol. 86, no. 24, p. 241401, 2012. *(Cited on page 3)*

[16] J. Wang, Y. Hernandez, M. Lotya, J. N. Coleman, and W. J. Blau, "Broadband Nonlinear Optical Response of Graphene Dispersions," *Advanced Materials*, vol. 21, no. 23, pp. 2430–2435, 2009. *(Cited on page 3)*

[17] Y. Li, C. Yu, Y. Gan, P. Jiang, J. Yu, Y. Ou, D.-F. Zou, C. Huang, J. Wang, T. Jia, Q. Luo, X.-F. Yu, H. Zhao, C.-F. Gao, and J. Li, "Mapping the elastic properties of two-dimensional MoS2 via bi-

modal atomic force microscopy and finite element simulation," *npj Computational Materials*, vol. 4, no. 1, p. 49, 2018. *(Cited on page 3)*

[18] V. Shanmugam, R. A. Mensah, K. Babu, S. Gawusu, A. Chanda, Y. Tu, R. E. Neisiany, M. Försth, G. Sas, and O. Das, "A Review of the Synthesis, Properties, and Applications of 2D Materials," *Particle and Particle Systems Characterization*, vol. 39, no. 6, 2022. *(Cited on page 4)*

[19] J. Zhang, P. Hu, X. Wang, Z. Wang, D. Liu, B. Yang, and W. Cao, "CVD growth of large area and uniform graphene on tilted copper foil for high performance flexible transparent conductive film," *Journal of Materials Chemistry*, vol. 22, no. 35, pp. 18283–18290, 2012. *(Cited on page 4)*

[20] A. Alnuaimi, I. Almansouri, I. Saadat, and A. Nayfeh, "Toward fast growth of large area high quality graphene using a cold-wall CVD reactor," *RSC Adv.*, vol. 7, no. 82, pp. 51951–51957, 2017. *(Cited on page 4)*

[21] A. H. Castro Neto, F. Guinea, N. M. R. Peres, K. S. Novoselov, and A. K. Geim, "The electronic properties of graphene," *Reviews of Modern Physics*, vol. 81, no. 1, pp. 109–162, 2009. *(Cited on page 5)*

[22] D. C. Elias, R. V. Gorbachev, A. S. Mayorov, S. V. Morozov, A. A. Zhukov, P. Blake, L. A. Ponomarenko, I. V. Grigorieva, K. S. Novoselov, F. Guinea, and A. K. Geim, "Dirac cones reshaped by interaction effects in suspended graphene," *Nature Physics*, vol. 7, no. 9, pp. 701–704, 2011. *(Cited on page 5)*

[23] K. I. Bolotin, K. J. Sikes, Z. Jiang, M. Klima, G. Fudenberg, J. Hone, P. Kim, and H. L. Stormer, "Ultrahigh electron mobility in suspended graphene," *Solid State Communications*, vol. 146, no. 9, pp. 351–355, 2008. *(Cited on page 5)*

[24] F. Wang, Y. Zhang, C. Tian, C. Girit, A. Zettl, M. Crommie, and Y. R. Shen, "Gate-Variable Optical Transitions in Graphene," *Science*, vol. 320, no. 5873, pp. 206–209, 2008. *(Cited on page 5)*

[25] C. Lee, X. Wei, J. W. Kysar, and J. Hone, "Measurement of the Elastic Properties and Intrinsic Strength of Monolayer Graphene," *Science*, vol. 321, no. 5887, pp. 385–388, 2008. *(Cited on page 5)*

[26] A. A. Balandin, "Thermal properties of graphene and nanostructured carbon materials," *Nature Materials*, vol. 10, no. 8, pp. 569–581, 2011. *(Cited on page 5)*

[27] S. Tang, W. Wu, X. Xie, X. Li, and J. Gu, "Band gap opening of bilayer graphene by graphene oxide support doping," *RSC Advances*, vol. 7, no. 16, pp. 9862–9871, 2017. *(Cited on page 5)*

[28] Z. H. Ni, T. Yu, Y. H. Lu, Y. Y. Wang, Y. P. Feng, and Z. X. Shen, "Uniaxial strain on graphene: Raman spectroscopy study and band-gap opening," *ACS Nano*, vol. 2, no. 11, pp. 2301–2305, 2008. *(Cited on page 5)*

[29] Z. Xiong, L. Zhong, H. Wang, and X. Li, "Structural Defects, Mechanical Behaviors, and Properties of Two-Dimensional Materials.," *Materials (Basel, Switzerland)*, vol. 14, mar 2021. *(Cited on pages 5 and 7)*

[30] S. Z. Butler, S. M. Hollen, L. Cao, Y. Cui, J. A. Gupta, H. R. Gutiérrez, T. F. Heinz, S. S. Hong, J. Huang, A. F. Ismach, E. Johnston-Halperin, M. Kuno, V. V. Plashnitsa, R. D. Robinson, R. S. Ruoff, S. Salahuddin, J. Shan, L. Shi, M. G. Spencer, M. Terrones, W. Windl, and J. E. Goldberger, "Progress, Challenges, and Opportunities in Two-Dimensional Materials Beyond Graphene," *ACS Nano*, vol. 7, no. 4, pp. 2898–2926, 2013. *(Cited on page 5)*

[31] R. Ganatra and Q. Zhang, "Few-Layer MoS2: A Promising Layered Semiconductor," *ACS Nano*, vol. 8, no. 5, pp. 4074–4099, 2014. *(Cited on page 5)*

[32] C. Ruppert, B. Aslan, and T. F. Heinz, "Optical Properties and Band Gap of Single- and Few-Layer MoTe2 Crystals," *Nano Letters*, vol. 14, no. 11, pp. 6231–6236, 2014. *(Cited on page 5)*

[33] A. Berkdemir, H. R. Gutiérrez, A. R. Botello-Méndez, N. Perea-López, A. L. Elías, C.-I. Chia, B. Wang, V. H. Crespi, F. López-Urías, J.-C. Charlier, H. Terrones, and M. Terrones, "Identification of individual and few layers of WS2 using Raman Spectroscopy," *Scientific Reports*, vol. 3, no. 1, p. 1755, 2013. *(Cited on page 5)*

[34] A. Splendiani, L. Sun, Y. Zhang, T. Li, J. Kim, C.-Y. Chim, G. Galli, and F. Wang, "Emerging Photoluminescence in Monolayer MoS2," *Nano Letters*, vol. 10, no. 4, pp. 1271–1275, 2010. *(Cited on page 6)*

[35] G. Eda, H. Yamaguchi, D. Voiry, T. Fujita, M. Chen, and M. Chhowalla, "Photoluminescence from Chemically Exfoliated MoS2," *Nano Letters*, vol. 11, no. 12, pp. 5111–5116, 2011. *(Cited on page 6)*

[36] K. K. Kim, A. Hsu, X. Jia, S. M. Kim, Y. Shi, M. Dresselhaus, T. Palacios, and J. Kong, "Synthesis and Characterization of Hexagonal Boron Nitride Film as a Dielectric Layer for Graphene Devices," *ACS Nano*, vol. 6, no. 10, pp. 8583–8590, 2012. *(Cited on page 6)*

[37] S. Kim, A. Hsu, M. Park, S. Chae, S. Yun, J. Lee, D.-H. Cho, W. Fang, C. Lee, T. Palacios, M. Dresselhaus, K. Kim, Y. H. Lee, and J. Kong, "Synthesis of large-area multilayer hexagonal boron nitride for high material performance," *Nature Communications*, vol. 6, p. 8662, 2015. *(Cited on page 6)*

[38] H. Zhang, C.-X. Liu, X.-L. Qi, X. Dai, Z. Fang, and S.-C. Zhang, "Topological insulators in Bi2Se3, Bi2Te3 and Sb2Te3 with a single Dirac cone on the surface," *Nature Physics*, vol. 5, no. 6, pp. 438–442, 2009. *(Cited on page 6)*

[39] A. Ambrosi, Z. Sofer, J. Luxa, and M. Pumera, "Exfoliation of Layered Topological Insulators Bi2Se3 and Bi2Te3 via Electrochemistry," *ACS Nano*, vol. 10, no. 12, pp. 11442–11448, 2016. *(Cited on page 6)*

[40] K. Shahil, M. Hossain, V. Goyal, and A. Balandin, "Micro-Raman spectroscopy of mechanically exfoliated few-quintuple layers of Bi2Te3, Bi2Se3, and Sb2Te3 materials," *Journal of Applied Physics*, vol. 111, p. 54305, 2012. *(Cited on page 6)*

[41] A. Molle, C. Grazianetti, L. Tao, D. Taneja, M. H. Alam, and D. Akinwande, "Silicene, silicene derivatives, and their device applications," *Chemical Society Reviews*, vol. 47, no. 16, pp. 6370–6387, 2018. *(Cited on page 7)*

[42] E. Cinquanta, E. Scalise, D. Chiappe, C. Grazianetti, B. Van Den Broek, M. Houssa, M. Fanciulli, and A. Molle, "Getting through the nature of silicene: An sp2-sp3 two-dimensional silicon nanosheet," *Journal of Physical Chemistry C*, vol. 117, no. 32, pp. 16719–16724, 2013. *(Cited on pages 7, 32, 48, and 58)*

[43] P. De Padova, C. Ottaviani, C. Quaresima, B. Olivieri, P. Imperatori, E. Salomon, T. Angot, L. Quagliano, C. Romano, A. Vona, M. Muniz-Miranda, A. Generosi, B. Paci, and G. Le Lay, "24 h stability of thick multilayer silicene in air," *2D Materials*, vol. 1, no. 2, p. 21003, 2014. *(Cited on pages 7 and 45)*

[44] A. Molle, C. Grazianetti, D. Chiappe, E. Cinquanta, E. Cianci, G. Tallarida, and M. Fanciulli, "Hindering the Oxidation of Silicene

with Non-Reactive Encapsulation," *Advanced Functional Materials*, vol. 23, no. 35, pp. 4340–4344, 2013. *(Cited on pages 7 and 51)*

[45] J. Yoshinobu, K. Mukai, H. Ueda, S. Yoshimoto, S. Shimizu, T. Koitaya, H. Noritake, C.-C. Lee, T. Ozaki, A. Fleurence, R. Friedlein, and Y. Yamada-Takamura, "Formation of BN-covered silicene on ZrB2/Si(111) by adsorption of NO and thermal processes," *The Journal of Chemical Physics*, vol. 153, no. 6, p. 64702, 2020. *(Cited on page 7)*

[46] K. Takeda and K. Shiraishi, "Theoretical possibility of stage corrugation in Si and Ge analogs of graphite," *Phys. Rev. B*, vol. 50, no. 20, pp. 14916–14922, 1994. *(Cited on page 8)*

[47] G. G. Guzmán-Verri and L. C. Lew Yan Voon, "Electronic structure of silicon-based nanostructures," *Physical Review B*, vol. 76, no. 7, p. 75131, 2007. *(Cited on page 8)*

[48] S. Cahangirov, M. Topsakal, E. Aktürk, H. Şahin, and S. Ciraci, "Two- and One-Dimensional Honeycomb Structures of Silicon and Germanium," *Physical Review Letters*, vol. 102, no. 23, p. 236804, 2009. *(Cited on page 8)*

[49] N. D. Drummond, V. Zólyomi, and V. I. Fal'ko, "Electrically tunable band gap in silicene," *Physical Review B*, vol. 85, no. 7, p. 75423, 2012. *(Cited on pages 8 and 9)*

[50] M. Henini, "Molecular beam epitaxy," *Molecular Beam Epitaxy*, 2013. *(Cited on page 8)*

[51] L. Meng, Y. Wang, L. Zhang, S. Du, R. Wu, L. Li, Y. Zhang, G. Li, H. Zhou, W. A. Hofer, and H.-J. Gao, "Buckled Silicene Formation on Ir(111)," *Nano Letters*, vol. 13, no. 2, pp. 685–690, 2013. *(Cited on page 9)*

[52] A. Fleurence, R. Friedlein, T. Ozaki, H. Kawai, Y. Wang, and Y. Yamada-Takamura, "Experimental Evidence for Epitaxial Silicene on Diboride Thin Films," *Physical Review Letters*, vol. 108, no. 24, p. 245501, 2012. *(Cited on page 9)*

[53] A. Stepniak-Dybala and M. Krawiec, "Formation of Silicene on Ultrathin Pb(111) Films," *The Journal of Physical Chemistry C*, vol. 123, no. 27, pp. 17019–17025, 2019. *(Cited on page 9)*

[54] P. Vogt, P. De Padova, C. Quaresima, J. Avila, E. Frantzeskakis, M. C. Asensio, A. Resta, B. Ealet, and G. Le Lay, "Silicene: Compelling Experimental Evidence for Graphenelike Two-Dimensional

Silicon," *Physical Review Letters*, vol. 108, no. 15, p. 155501, 2012. *(Cited on pages 9, 10, and 45)*

[55] N. Takagi, C.-L. Lin, K. Kawahara, E. Minamitani, N. Tsukahara, M. Kawai, and R. Arafune, "Silicene on Ag(111): Geometric and electronic structures of a new honeycomb material of Si," *Progress in Surface Science*, vol. 90, no. 1, pp. 1–20, 2015. *(Cited on page 9)*

[56] C.-L. Lin, R. Arafune, K. Kawahara, N. Tsukahara, E. Minamitani, Y. Kim, N. Takagi, and M. Kawai, "Structure of Silicene Grown on Ag(111)," *Applied Physics Express*, vol. 5, no. 4, p. 45802, 2012. *(Cited on page 9)*

[57] H. Enriquez, S. Vizzini, A. Kara, B. Lalmi, and H. Oughaddou, "Silicene structures on silver surfaces," *Journal of Physics: Condensed Matter*, vol. 24, no. 31, p. 314211, 2012. *(Cited on page 9)*

[58] H. Jamgotchian, Y. Colignon, N. Hamzaoui, B. Ealet, J. Y. Hoarau, B. Aufray, and J. P. Bibérian, "Growth of silicene layers on Ag(111): unexpected effect of the substrate temperature," *Journal of Physics: Condensed Matter*, vol. 24, no. 17, p. 172001, 2012. *(Cited on page 9)*

[59] D. Kaltsas, L. Tsetseris, and A. Dimoulas, "Structural evolution of single-layer films during deposition of silicon on silver: a first-principles study," *Journal of Physics: Condensed Matter*, vol. 24, no. 44, p. 442001, 2012. *(Cited on page 9)*

[60] B. Mortazavi, A. Dianat, G. Cuniberti, and T. Rabczuk, "Application of silicene, germanene and stanene for Na or Li ion storage: A theoretical investigation," *Electrochimica Acta*, vol. 213, pp. 865–870, 2016. *(Cited on page 9)*

[61] R. Pawlak, C. Drechsel, P. D'Astolfo, M. Kisiel, E. Meyer, and J. I. Cerda, "Quantitative determination of atomic buckling of silicene by atomic force microscopy," *Proceedings of the National Academy of Sciences*, vol. 117, no. 1, pp. 228–237, 2020. *(Cited on page 9)*

[62] F. Bechstedt, *Principles of Surface Physics*. Springer-Verlag Berlin Heidelberg, 2003. *(Cited on page 9)*

[63] R. Arafune, C.-L. Lin, K. Kawahara, N. Tsukahara, E. Minamitani, Y. Kim, N. Takagi, and M. Kawai, "Structural transition of silicene on Ag(111)," *Surface Science*, vol. 608, pp. 297–300, 2013. *(Cited on page 10)*

[64] P. Moras, T. O. Mentes, P. M. Sheverdyaeva, A. Locatelli, and C. Carbone, "Coexistence of multiple silicene phases in silicon

grown on Ag(1 1 1)," *Journal of Physics Condensed Matter*, vol. 26, no. 18, 2014. *(Cited on pages 10, 30, and 45)*

[65] Z.-X. Guo, S. Furuya, J.-i. Iwata, and A. Oshiyama, "Absence and presence of Dirac electrons in silicene on substrates," *Physical Review B*, vol. 87, no. 23, p. 235435, 2013. *(Cited on page 10)*

[66] E. Scalise, E. Cinquanta, M. Houssa, B. Van Den Broek, D. Chiappe, C. Grazianetti, G. Pourtois, B. Ealet, A. Molle, M. Fanciulli, V. V. Afanas'Ev, and A. Stesmans, "Vibrational properties of epitaxial silicene layers on (111) Ag," *Applied Surface Science*, vol. 291, pp. 113–117, 2014. *(Cited on pages 10 and 32)*

[67] Y. Xu, B. Yan, H. J. Zhang, J. Wang, G. Xu, P. Tang, W. Duan, and S. C. Zhang, "Large-gap quantum spin hall insulators in tin films," *Physical Review Letters*, vol. 111, no. 13, 2013. *(Cited on pages 10 and 11)*

[68] F.-f. Zhu, W.-j. Chen, Y. Xu, C.-l. Gao, D.-d. Guan, C.-h. Liu, D. Qian, S.-C. Zhang, and J.-f. Jia, "Epitaxial growth of two-dimensional stanene," *Nature Materials*, vol. 14, no. 10, pp. 1020–1025, 2015. *(Cited on page 10)*

[69] C.-Z. Xu, Y.-H. Chan, P. Chen, X. Wang, D. Flötotto, J. A. Hlevyack, G. Bian, S.-K. Mo, M.-Y. Chou, and T.-C. Chiang, "Gapped electronic structure of epitaxial stanene on InSb(111)," *Physical Review B*, vol. 97, no. 3, p. 35122, 2018. *(Cited on page 10)*

[70] Y. Zang, T. Jiang, Y. Gong, Z. Guan, C. Liu, M. Liao, K. Zhu, Z. Li, L. Wang, W. Li, C. Song, D. Zhang, Y. Xu, K. He, X. Ma, S.-C. Zhang, and Q.-K. Xue, "Realizing an Epitaxial Decorated Stanene with an Insulating Bandgap," *Advanced Functional Materials*, vol. 28, no. 35, p. 1802723, 2018. *(Cited on page 10)*

[71] J. Yuhara, Y. Fujii, K. Nishino, N. Isobe, M. Nakatake, L. Xian, A. Rubio, and G. Le Lay, "Large area planar stanene epitaxially grown on Ag (1 1 1)," *2D Materials*, vol. 5, no. 2, p. 25002, 2018. *(Cited on pages 11 and 30)*

[72] R. Ahmed, T. Nakagawa, and S. Mizuno, "Structure determination of ultra-flat stanene on Cu(111) using low energy electron diffraction," *Surface Science*, vol. 691, p. 121498, 2020. *(Cited on page 11)*

[73] C. X. Zhao and J. F. Jia, "Stanene: A good platform for topological insulator and topological superconductor," *Frontiers of Physics*, vol. 15, no. 5, 2020. *(Cited on page 11)*

[74] C. Z. Xu, Y. H. Chan, Y. Chen, P. Chen, X. Wang, C. Dejoie, M. H. Wong, J. A. Hlevyack, H. Ryu, H. Y. Kee, N. Tamura, M. Y. Chou, Z. Hussain, S. K. Mo, and T. C. Chiang, "Elemental Topological Dirac Semimetal: α -Sn on InSb(111)," *Physical Review Letters*, vol. 118, no. 14, pp. 1–5, 2017. *(Cited on pages 12 and 75)*

[75] A. A. Burkov, "Topological semimetals," *Nature Materials*, vol. 15, no. 11, pp. 1145–1148, 2016. *(Cited on page 12)*

[76] J. E. Moore, "The birth of topological insulators," *Nature*, vol. 464, no. 7286, pp. 194–198, 2010. *(Cited on page 12)*

[77] S. Deng, A. V. Sumant, and V. Berry, "Strain engineering in two-dimensional nanomaterials beyond graphene," *Nano Today*, vol. 22, pp. 14–35, 2018. *(Cited on page 13)*

[78] B. Feng, Z. Ding, S. Meng, Y. Yao, X. He, P. Cheng, L. Chen, and K. Wu, "Evidence of Silicene in Honeycomb Structures of Silicon on Ag(111)," *Nano Letters*, vol. 12, no. 7, pp. 3507–3511, 2012. *(Cited on page 15)*

[79] C. Grazianetti, E. Cinquanta, and A. Molle, "Two-dimensional silicon: The advent of silicene," *2D Materials*, vol. 3, no. 1, 2016. *(Cited on page 15)*

[80] J. Yuhara, H. Shimazu, K. Ito, A. Ohta, M. Araidai, M. Kurosawa, M. Nakatake, and G. Le Lay, "Germanene Epitaxial Growth by Segregation through Ag(111) Thin Films on Ge(111)," *ACS Nano*, vol. 12, no. 11, pp. 11632–11637, 2018. *(Cited on page 16)*

[81] A. M. Tokmachev, D. V. Averyanov, I. A. Karateev, O. E. Parfenov, A. L. Vasiliev, S. N. Yakunin, and V. G. Storchak, "Topotactic synthesis of the overlooked multilayer silicene intercalation compound SrSi2," *Nanoscale*, vol. 8, no. 36, pp. 16229–16235, 2016. *(Cited on page 16)*

[82] M. A. Van Hove, W. H. Weinberg, and C.-M. Chan, "Kinematic LEED Theory and Its Limitations. In: Low-Energy Electron Diffraction: Experiment, Theory and Surface Structure Determination," pp. 91–144, Berlin, Heidelberg: Springer Berlin Heidelberg, 1986. *(Cited on page 20)*

[83] D. P. Woodruff, "Low Energy Electron Diffraction," Elsevier, 2016. *(Cited on page 20)*

[84] M. A. Van Hove, W. H. Weinberg, and C.-M. Chan, "Ordered Surfaces: Structure and Diffraction Pattern. In: Low-Energy Electron

Diffraction: Experiment, Theory and Surface Structure Determination," pp. 47–90, Berlin, Heidelberg: Springer Berlin Heidelberg, 1986. *(Cited on page 20)*

[85] D. A. Long, "Survey of Light-scattering Phenomena," in *The Raman Effect*, pp. 3–18, 2002. *(Cited on page 21)*

[86] S. Mosca, C. Conti, N. Stone, and P. Matousek, "Spatially offset Raman spectroscopy," *Nature Reviews Methods Primers*, vol. 1, no. 1, p. 21, 2021. *(Cited on page 21)*

[87] Herman A. Szymanski, ed., *Raman Spectroscopy: Theory and Practice*. Springer New York, 1967. *(Cited on page 21)*

[88] D. A. Long, "Quantum Mechanical Theory of Rayleigh and Raman Scattering," in *The Raman Effect*, pp. 49–84, 2002. *(Cited on page 21)*

[89] E. Smith and G. Dent, "The Raman Experiment – Raman Instrumentation, Sample Presentation, Data Handling and Practical Aspects of Interpretation," in *Modern Raman Spectroscopy*, pp. 21–75, 2019. *(Cited on page 23)*

[90] P. Vogt, P. Capiod, M. Berthe, A. Resta, P. De Padova, T. Bruhn, G. Le Lay, and B. Grandidier, "Synthesis and electrical conductivity of multilayer silicene," *Applied Physics Letters*, vol. 104, no. 2, p. 21602, 2014. *(Cited on page 30)*

[91] D. A. Mckeown, M. I. Bell, and E. S. Etz, "Vibrational analysis of the dioctahedral mica: 2M1 muscovite," vol. 84, no. 7-8, pp. 1041–1048, 1999. *(Cited on page 32)*

[92] C. Grazianetti, E. Cinquanta, L. Tao, P. De Padova, C. Quaresima, C. Ottaviani, D. Akinwande, and A. Molle, "Silicon Nanosheets: Crossover between Multilayer Silicene and Diamond-like Growth Regime," *ACS Nano*, vol. 11, no. 3, pp. 3376–3382, 2017. *(Cited on pages 33 and 48)*

[93] M. Kang, J. H. Byun, S. Na, and N. L. Jeon, "Fabrication of functional 3D multi-level microstructures on transparent substrates by one step back-side UV photolithography," *RSC Adv.*, vol. 7, no. 22, pp. 13353–13361, 2017. *(Cited on page 34)*

[94] W. Macdonald, M. Looney, D. MacKerron, R. Eveson, R. Adam, K. Hashimoto, and K. Rakos, "Latest Advances in Substrates for Flexible Electronics," *Journal of The Society for Information Display - J SOC INF DISP*, vol. 15, 2007. *(Cited on page 34)*

[95] B. Zhu, H. Wang, W. R. Leow, Y. Cai, X. J. Loh, M.-Y. Han, and X. Chen, "Silk Fibroin for Flexible Electronic Devices," *Advanced Materials*, vol. 28, no. 22, pp. 4250–4265, 2016. *(Cited on page 34)*

[96] J. Kim, A. Banks, H. Cheng, Z. Xie, S. Xu, K.-I. Jang, J. W. Lee, Z. Liu, P. Gutruf, X. Huang, P. Wei, F. Liu, K. Li, M. Dalal, R. Ghaffari, X. Feng, Y. Huang, S. Gupta, U. Paik, and J. A. Rogers, "Epidermal Electronics with Advanced Capabilities in Near-Field Communication," *Small*, vol. 11, no. 8, pp. 906–912, 2015. *(Cited on page 34)*

[97] R. Dahiya and S. Gennaro, "Bendable Ultra-Thin Chips on Flexible Foils," *IEEE Sensors Journal*, vol. 13, pp. 4030 – 4037, 2013. *(Cited on page 34)*

[98] L. Tao, E. Cinquanta, D. Chiappe, C. Grazianetti, M. Fanciulli, M. Dubey, A. Molle, and D. Akinwande, "Silicene field-effect transistors operating at room temperature," *Nature Nanotechnology*, vol. 10, no. 3, pp. 227–231, 2015. *(Cited on pages 35 and 45)*

[99] C. Martella, G. Faraone, M. H. Alam, D. Taneja, L. Tao, G. Scavia, E. Bonera, C. Grazianetti, D. Akinwande, and A. Molle, "Disassembling Silicene from Native Substrate and Transferring onto an Arbitrary Target Substrate," *Advanced Functional Materials*, vol. 30, no. 42, p. 2004546, 2020. *(Cited on pages 35 and 42)*

[100] E. Yakubovskaya, T. Zaliznyak, J. Martínez Martínez, and G. T. Taylor, "Tear Down the Fluorescent Curtain: A New Fluorescence Suppression Method for Raman Microspectroscopic Analyses," *Scientific Reports*, vol. 9, no. 1, p. 15785, 2019. *(Cited on page 39)*

[101] J. J. Blackstock, Z. Li, and G.-y. Jung, "Template stripping using cold welding," *Journal of Vacuum Science & Technology A*, vol. 22, no. 3, pp. 602–605, 2004. *(Cited on page 40)*

[102] H. K. Sahoo, L. Ottaviano, Y. Zheng, O. Hansen, and K. Yvind, "Low temperature bonding of heterogeneous materials using Al2O3 as an intermediate layer," *Journal of Vacuum Science & Technology B*, vol. 36, no. 1, p. 11202, 2017. *(Cited on page 40)*

[103] U. P. Shinde, H. S. Aher, and T. bhavsing Pawar, "Solubility and Density of Silver Iodide in Water and DMF at Various Temperatures as Function of Potassium Iodide.," *IOSR Journal of Applied Physics*, vol. 09, pp. 64–67, 2017. *(Cited on page 42)*

[104] A. T. Vogel, J. De Boor, M. Becker, J. V. Wittemann, S. L. Mensah, P. Werner, and V. Schmidt, "Ag-assisted CBE growth of or-

dered InSb nanowire arrays," *Nanotechnology*, vol. 22, no. 1, 2011. *(Cited on page 43)*

[105] C. J. Buchenauer, M. Cardona, and F. H. Pollak, "Raman Scattering in Gray Tin," *Physical Review B*, vol. 3, no. 4, pp. 1243–1244, 1971. *(Cited on page 44)*

[106] J. Menéndez and H. Höchst, "Study of the phase transition in heteroepitaxially grown films of αSn by Raman spectroscopy," *Thin Solid Films*, vol. 111, no. 4, pp. 375–379, 1984. *(Cited on page 44)*

[107] H. Li, F. Hui-Xia, and S. Meng, "Silicene: from monolayer to multilayer — A concise review," *Chinese Physics B*, vol. 24, no. 8, p. 86102, 2015. *(Cited on page 45)*

[108] V. Ritter, J. Genser, D. Nazzari, O. Bethge, E. Bertagnolli, and A. Lugstein, "Silicene Passivation by Few-Layer Graphene," *ACS Applied Materials and Interfaces*, vol. 11, no. 13, pp. 12745–12751, 2019. *(Cited on page 45)*

[109] J. Genser, D. Nazzari, V. Ritter, O. Bethge, K. Watanabe, T. Taniguchi, E. Bertagnolli, F. Bechstedt, and A. Lugstein, "Optical Signatures of Dirac Electrodynamics for hBN-Passivated Silicene on Au(111)," *Nano Letters*, vol. 21, no. 12, pp. 5301–5307, 2021. *(Cited on page 45)*

[110] D. Nazzari, J. Genser, V. Ritter, O. Bethge, E. Bertagnolli, T. Grasser, W. M. Weber, and A. Lugstein, "Epitaxial Growth of Crystalline CaF2 on Silicene," *ACS Applied Materials and Interfaces*, vol. 14, no. 28, pp. 32675–32682, 2022. *(Cited on page 45)*

[111] D. S. Dhungana, C. Massetti, C. Martella, C. Grazianetti, and A. Molle, "All-around encapsulation of silicene," *Nanoscale Horiz.*, vol. 8, no. 10, pp. 1428–1434, 2023. *(Cited on page 45)*

[112] P. De Padova, A. Generosi, B. Paci, C. Ottaviani, C. Quaresima, B. Olivieri, E. Salomon, T. Angot, and G. Le Lay, "Multilayer silicene: clear evidence," *2D Materials*, vol. 3, no. 3, p. 31011, 2016. *(Cited on page 48)*

[113] M. A. Stranick and A. Moskwa, "SnO by XPS," *Surface Science Spectra*, vol. 2, no. 1, pp. 45–49, 1993. *(Cited on page 52)*

[114] M. A. Stranick and A. Moskwa, "SnO2 by XPS," *Surface Science Spectra*, vol. 2, no. 1, pp. 50–54, 1993. *(Cited on page 52)*

[115] A. Daus, S. Vaziri, V. Chen, Ç. Köroğlu, R. W. Grady, C. S. Bailey, H. R. Lee, K. Schauble, K. Brenner, and E. Pop, "High-performance flexible nanoscale transistors based on transition metal dichalcogenides," *Nature Electronics*, vol. 4, no. 7, pp. 495–501, 2021. *(Cited on page 55)*

[116] L. T. Quynh, C.-W. Cheng, C.-T. Huang, S. S. Raja, R. Mishra, M.-J. Yu, Y.-J. Lu, and S. Gwo, "Flexible Plasmonics Using Aluminum and Copper Epitaxial Films on Mica," *ACS Nano*, vol. 16, no. 4, pp. 5975–5983, 2022. *(Cited on page 55)*

[117] X. Han, K. J. Seo, Y. Qiang, Z. Li, S. Vinnikova, Y. Zhong, X. Zhao, P. Hao, S. Wang, and H. Fang, "Nanomeshed Si nanomembranes," *npj Flexible Electronics*, vol. 3, no. 1, p. 9, 2019. *(Cited on page 55)*

[118] D. Kireev, J. Kampfe, A. Hall, and D. Akinwande, "Graphene electronic tattoos 2.0 with enhanced performance, breathability and robustness," *npj 2D Materials and Applications*, vol. 6, no. 1, p. 46, 2022. *(Cited on page 55)*

[119] I. Niehues, R. Schmidt, M. Drüppel, P. Marauhn, D. Christiansen, M. Selig, G. Berghäuser, D. Wigger, R. Schneider, L. Braasch, R. Koch, A. Castellanos-Gomez, T. Kuhn, A. Knorr, E. Malic, M. Rohlfing, S. Michaelis de Vasconcellos, and R. Bratschitsch, "Strain Control of Exciton-Phonon Coupling in Atomically Thin Semiconductors," *Nano letters*, vol. 18, no. 3, pp. 1751–1757, 2018. *(Cited on page 55)*

[120] A. Castellanos-Gomez, R. Roldán, E. Cappelluti, M. Buscema, F. Guinea, H. S. Van Der Zant, and G. A. Steele, "Local strain engineering in atomically thin MoS2," *Nano Letters*, vol. 13, no. 11, pp. 5361–5366, 2013. *(Cited on pages 55, 62, and 63)*

[121] T. Sohier, D. Campi, N. Marzari, and M. Gibertini, "Mobility of two-dimensional materials from first principles in an accurate and automated framework," *Physical Review Materials*, vol. 2, no. 11, p. 114010, 2018. *(Cited on page 55)*

[122] I. M. Datye, A. Daus, R. W. Grady, K. Brenner, S. Vaziri, and E. Pop, "Strain-Enhanced Mobility of Monolayer MoS2," *Nano Letters*, vol. 22, no. 20, pp. 8052–8059, 2022. *(Cited on pages 55 and 57)*

[123] F. Li, T. Shen, C. Wang, Y. Zhang, J. Qi, and H. Zhang, "Recent Advances in Strain-Induced Piezoelectric and Piezoresistive Effect-Engineered 2D Semiconductors for Adaptive Electronics

and Optoelectronics," *Nano-Micro Letters*, vol. 12, no. 1, p. 106, 2020. *(Cited on page 55)*

[124] F. Carrascoso, H. Li, R. Frisenda, and A. Castellanos-Gomez, "Strain engineering in single-, bi- and tri-layer MoS2, MoSe2, WS2 and WSe2," *Nano Research*, vol. 14, no. 6, pp. 1698–1703, 2021. *(Cited on pages 55 and 56)*

[125] C. Grazianetti, C. Martella, and A. Molle, "The Xenes Generations: A Taxonomy of Epitaxial Single-Element 2D Materials," *physica status solidi (RRL) – Rapid Research Letters*, vol. 14, no. 2, p. 1900439, 2020. *(Cited on page 55)*

[126] C. Martella, C. Massetti, D. S. Dhungana, E. Bonera, C. Grazianetti, and A. Molle, "Bendable Silicene Membranes," *Advanced Materials*, p. 2211419, 2023. *(Cited on page 56)*

[127] T. M. G. Mohiuddin, A. Lombardo, R. R. Nair, A. Bonetti, G. Savini, R. Jalil, N. Bonini, D. M. Basko, C. Galiotis, N. Marzari, K. S. Novoselov, A. K. Geim, and A. C. Ferrari, "Uniaxial strain in graphene by Raman spectroscopy: G peak splitting, Grüneisen parameters, and sample orientation," *Physical Review B*, vol. 79, no. 20, p. 205433, 2009. *(Cited on pages 56, 59, and 61)*

[128] O. Çakıroğlu, J. O. Island, Y. Xie, R. Frisenda, and A. Castellanos-Gomez, "An Automated System for Strain Engineering and Straintronics of 2D Materials," *Advanced Materials Technologies*, p. 2201091, 2022. *(Cited on page 56)*

[129] R. Schmidt, I. Niehues, R. Schneider, M. Drüppel, T. Deilmann, M. Rohlfing, S. M. de Vasconcellos, A. Castellanos-Gomez, and R. Bratschitsch, "Reversible uniaxial strain tuning in atomically thin WSe2," *2D Materials*, vol. 3, no. 2, p. 21011, 2016. *(Cited on page 57)*

[130] E. Grüneisen, "Zustand des festen Körpers BT - Thermische Eigenschaften der Stoffe," pp. 1–59, Springer Berlin Heidelberg, 1926. *(Cited on page 59)*

[131] J. M. Ziman, *Electrons and phonons: the theory of transport phenomena in solids*. Oxford university press, 2001. *(Cited on page 60)*

[132] S. Reich, H. Jantoljak, and C. Thomsen, "Shear strain in carbon nanotubes under hydrostatic pressure," *Physical Review B*, vol. 61, no. 20, pp. R13389–R13392, 2000. *(Cited on page 60)*

[133] G. Grimvall, *Thermophysical properties of materials*. Elsevier Science Pub. Co. Inc.,New York, NY, 1986. *(Cited on page 60)*

[134] N. S. Mueller, S. Heeg, M. P. Alvarez, P. Kusch, S. Wasserroth, N. Clark, F. Schedin, J. Parthenios, K. Papagelis, C. Galiotis, M. Kalbáč, A. Vijayaraghavan, U. Huebner, R. Gorbachev, O. Frank, and S. Reich, "Evaluating arbitrary strain configurations and doping in graphene with Raman spectroscopy," *2D Materials*, vol. 5, no. 1, pp. 30–35, 2018. *(Cited on page 60)*

[135] G. N. Greaves, A. L. Greer, R. S. Lakes, and T. Rouxel, "Poisson's ratio and modern materials," *Nature materials*, vol. 10, no. 11, pp. 823–837, 2011. *(Cited on pages 61 and 64)*

[136] X. J. Ge, K. L. Yao, and J. T. Lü, "Comparative study of phonon spectrum and thermal expansion of graphene, silicene, germanene, and blue phosphorene," *Physical Review B*, vol. 94, no. 16, pp. 1–8, 2016. *(Cited on page 62)*

[137] E. Cinquanta, G. Fratesi, S. dal Conte, C. Grazianetti, F. Scotognella, S. Stagira, C. Vozzi, G. Onida, and A. Molle, "Optical response and ultrafast carrier dynamics of the silicene-silver interface," *Physical Review B*, vol. 92, no. 16, p. 165427, 2015. *(Cited on page 62)*

[138] H. Mizubayashi, J. Matsuno, and H. Tanimoto, "Young's modulus of silver films," *Scripta Materialia*, vol. 41, no. 4, pp. 443–448, 1999. *(Cited on page 64)*

[139] E. Bonaventura, D. S. Dhungana, C. Martella, C. Grazianetti, S. Macis, S. Lupi, E. Bonera, and A. Molle, "Optical and thermal responses of silicene in Xene heterostructures," *Nanoscale Horizons*, vol. 7, no. 8, pp. 924–930, 2022. *(Cited on pages 65 and 67)*

[140] D. Tristant, A. Cupo, X. Ling, and V. Meunier, "Phonon Anharmonicity in Few-Layer Black Phosphorus," *ACS Nano*, vol. 13, no. 9, pp. 10456–10468, 2019. *(Cited on page 65)*

[141] D. Yoon, Y.-W. Son, and H. Cheong, "Negative Thermal Expansion Coefficient of Graphene Measured by Raman Spectroscopy," *Nano Letters*, vol. 11, no. 8, pp. 3227–3231, 2011. *(Cited on page 65)*

[142] T. Wang, H. Wang, K. Kui, W. Liang, X. Luo, F. Verpoort, and Y. Zeng, "Xenes as an Emerging 2D Monoelemental Family: Fundamental Electrochemistry and Energy Applications," *Advanced Functional Materials*, vol. 30, p. 2002885, 2020. *(Cited on page 66)*

[143] I. Calizo, A. A. Balandin, W. Bao, F. Miao, and C. N. Lau, "Temperature dependence of the raman spectra of graphene and graphene multilayers," *Nano Letters*, vol. 7, no. 9, pp. 2645–2649, 2007. *(Cited on page 67)*

[144] L. Su and Y. Zhang, "Temperature coefficients of phonon frequencies and thermal conductivity in thin black phosphorus layers," *Applied Physics Letters*, vol. 107, no. 7, 2015. *(Cited on page 67)*

[145] H. Gu, Y. Lu, D. Zhu, K. Li, S. Zheng, J. Wang, K. W. Ang, K. Xu, and X. Liu, "High temperature study on the thermal properties of few-layer Mo0.5W0.5S2 and effects of capping layers," *Results in Physics*, vol. 7, pp. 4394–4397, 2017. *(Cited on page 67)*

[146] H. Xie, T. Ouyang, É. Germaneau, G. Qin, M. Hu, and H. Bao, "Large tunability of lattice thermal conductivity of monolayer silicene via mechanical strain," *Physical Review B*, vol. 93, no. 7, pp. 1–19, 2016. *(Cited on page 68)*

[147] H. Liu, G. Qin, and M. Hu, "Uniform Strain-Dependent Thermal Conductivity of Pentagonal and Hexagonal Silicene," *Frontiers in Materials*, vol. 8, pp. 1–11, 2021. *(Cited on page 68)*

[148] F. H. Pollak, M. Cardona, C. W. Higginbotham, F. Herman, and J. P. Van Dyke, "Energy-Band Structure and Optical Spectrum of Grey Tin," *Physical Review B*, vol. 2, no. 2, pp. 352–363, 1970. *(Cited on page 73)*

[149] L. D. Anh, K. Takase, T. Chiba, Y. Kota, K. Takiguchi, and M. Tanaka, "Elemental Topological Dirac Semimetal α-Sn with High Quantum Mobility," *Advanced Materials*, vol. 33, no. 51, pp. 1–9, 2021. *(Cited on pages 73, 74, and 79)*

[150] B. Q. Lv, T. Qian, and H. Ding, "Experimental perspective on three-dimensional topological semimetals," *Reviews of Modern Physics*, vol. 93, no. 2, p. 25002, 2021. *(Cited on page 74)*

[151] X.-L. Qi and S.-C. Zhang, "Topological insulators and superconductors," *Reviews of Modern Physics*, vol. 83, no. 4, pp. 1057–1110, 2011. *(Cited on page 75)*

[152] J. THEWLIS and A. R. DAVEY, "Thermal Expansion of Grey Tin," *Nature*, vol. 174, no. 4439, p. 1011, 1954. *(Cited on page 75)*

[153] W. Martienssen, O. Madelung, H. Landolt, and R. Börnstein, "Landolt-Börnstein numerical data and functional relationships in science and technology, New series," 1996. *(Cited on page 75)*

[154] O. Vail, P. Taylor, P. Folkes, B. Nichols, B. Haidet, K. Mukherjee, and G. de Coster, "Growth and Magnetotransport in Thin-Film α-Sn on CdTe," *Physica Status Solidi (B) Basic Research*, vol. 257, no. 1, pp. 1–7, 2020. *(Cited on pages 76 and 77)*

[155] J. Ding, C. Liu, V. Kalappattil, Y. Zhang, O. Mosendz, U. Erugu, R. Yu, J. Tian, A. DeMann, S. B. Field, X. Yang, H. Ding, J. Tang, B. Terris, A. Fert, H. Chen, and M. Wu, "Switching of a Magnet by Spin-Orbit Torque from a Topological Dirac Semimetal," *Advanced Materials*, vol. 33, no. 23, p. 2005909, 2021. *(Cited on pages 76 and 77)*

[156] C. Crosta, *Studio delle proprietà elettroniche dell'isolante topologico α-Sn per applicazioni spintroniche*. Bachelor's thesis, Milano-Bicocca, 2022. *(Cited on pages 76 and 77)*

[157] N. W. Ashcroft and N. D. Mermin, *Solid state physics*. Holt, Rinehart and Winston New York, 1976. *(Cited on page 76)*

[158] E. H. Hwang and S. Das Sarma, "Acoustic phonon scattering limited carrier mobility in two-dimensional extrinsic graphene," *Physical Review B*, vol. 77, no. 11, p. 115449, 2008. *(Cited on page 77)*

[159] G. J. de Coster, P. A. Folkes, P. J. Taylor, and O. A. Vail, "Effects of orientation and strain on the topological characteristics of CdTe/α-Sn quantum wells," *Physical Review B*, vol. 98, no. 11, p. 115153, 2018. *(Cited on page 77)*

[160] Y. Ding, H. Song, J. Huang, J. Yao, Y. Gu, L. Wei, Y. B. Chen, Y. Deng, H. Yuan, H. Lu, and Y.-F. Chen, "Wafer-Scale and Topologically Nontrivial α-Sn Films Grown on InSb(001) by Molecular-Beam Epitaxy," *Physical Review Applied*, vol. 17, no. 1, p. 14015, 2022. *(Cited on pages 79 and 84)*

[161] U. Merkt, M. Horst, T. Evelbauer, Kotthaus, and J. P., "Cyclotron and spin resonance in electron inversion layers on Insb," vol. 34, no. 10, 1986. *(Cited on page 81)*

[162] C. L. Littler and D. G. Seiler, "Temperature dependence of the energy gap of InSb using nonlinear optical techniques," *Applied Physics Letters*, vol. 46, no. 10, pp. 986–988, 1985. *(Cited on page 82)*

[163] M. Uchida, Y. Nakazawa, S. Nishihaya, K. Akiba, M. Kriener, Y. Kozuka, A. Miyake, Y. Taguchi, M. Tokunaga, N. Nagaosa, Y. Tokura, and M. Kawasaki, "Quantum Hall states observed in thin films of Dirac semimetal Cd3As2," *Nature Communications*, vol. 8, no. 1, 2017. *(Cited on page 84)*

[164] Z. Hu, J. Koo, Y. Hu, Q. Wang, M. Abeykoon, D. Graf, Y. Liu, H. Lei, J. Ma, M. Shi, B. Yan, and C. Petrovic, "Topological Dirac semimetal BaAuSb," *Physical Review Research*, vol. 5, no. 1, pp. 1–8, 2023. *(Cited on page 84)*

[165] T. Wojtowicz, M. Dobrowolska, G. Yang, H. Luo, J. K. Furdyna, L. W. Tu, and G. K. Wong, "Far-infrared determination of cyclotron and plasma-shifted cyclotron resonances in thin MBE-grown films of α-Sn," *Semiconductor Science and Technology*, vol. 5, no. 3 S, 1990. *(Cited on page 84)*

[166] Y. Liu, X. Duan, H.-J. Shin, S. Park, Y. Huang, and X. Duan, "Promises and prospects of two-dimensional transistors," *Nature*, vol. 591, no. 7848, pp. 43–53, 2021. *(Cited on page 87)*

[167] S. Wang, X. Liu, M. Xu, L. Liu, D. Yang, and P. Zhou, "Two-dimensional devices and integration towards the silicon lines," *Nature Materials*, vol. 21, no. 11, pp. 1225–1239, 2022. *(Cited on page 87)*

[168] B. Feng, J. Zhang, Q. Zhong, W. Li, S. Li, H. Li, P. Cheng, S. Meng, L. Chen, and K. Wu, "Experimental realization of two-dimensional boron sheets.," *Nature chemistry*, vol. 8, no. 6, pp. 563–568, 2016. *(Cited on page 88)*

[169] Y. Shao, Z. L. Liu, C. Cheng, X. Wu, H. Liu, C. Liu, J. O. Wang, S. Y. Zhu, Y. Q. Wang, D. X. Shi, K. Ibrahim, J. T. Sun, Y. L. Wang, and H. J. Gao, "Epitaxial Growth of Flat Antimonene Monolayer: A New Honeycomb Analogue of Graphene," *Nano Letters*, vol. 18, no. 3, pp. 2133–2139, 2018. *(Cited on page 88)*

[170] S. Sun, J.-Y. You, S. Duan, J. Gou, Y. Z. Luo, W. Lin, X. Lian, T. Jin, J. Liu, Y. Huang, Y. Wang, A. T. S. Wee, Y. P. Feng, L. Shen, J. L. Zhang, J. Chen, and W. Chen, "Epitaxial Growth of Ultraflat Bismuthene with Large Topological Band Inversion Enabled by Substrate-Orbital-Filtering Effect," *ACS Nano*, vol. 16, no. 1, pp. 1436–1443, 2022. *(Cited on page 88)*

[171] C. Grazianetti and A. Molle, "Engineering Epitaxial Silicene on Functional Substrates for Nanotechnology," *Research*, vol. 2019, pp. 1–8, 2019. *(Cited on page 89)*

[172] D. Wang, S. Zhao, R. Yin, L. Li, Z. Lou, and G. Shen, "Recent advanced applications of ion-gel in ionic-gated transistor," *npj Flexible Electronics*, vol. 5, no. 1, p. 13, 2021. *(Cited on page 90)*

Acknowledgements

I would like to acknowledge my Supervisor, Dr. Alessandro Molle, for the chance to undertake this research project and for believing in me from the very beginning. I would like to thank my Tutor, Prof. Emiliano Bonera, who has been continuously supportive and highly helpful, with competence and professionality.
Sincere thanks also to Prof. Fabio Pezzoli and his entire research group, for the measurements taken and the detailed and stimulating discussions.

I would like to express my gratitude to Dr. Carlo Grazianetti and Dr. Christian Martella, who have guided me step by step over the years; I thank Carlo for his numerous advices and exhaustive explanations, and Christian for sharing new ideas and insights.
My deep thanks to Mario, who has been a daily reference point for both cleanroom processes and tennis discussions.
My heartfelt thanks to the colleagues and friends of CNR-IMM who helped me and contributed to enrich my professional and personal experience, especially to Eleonora and Pinak, for everything we shared in the lab but especially outside.

Thanks to my lifelong friends for always being by my side, no matter where or when, and to Grazia for the invaluable moments spent together.

As I promised, a special thanks to the staff of Fisio & Riabilita, especially Simone, Laura, Paolo and Francesca without whom it would have been impossible to come back to the lab so quickly with a new cruciate ligament.

Finally, I dedicate this work to my family: my achievements are especially your merit.

Ringraziamenti

Desidero ringraziare prima di tutto il mio Supervisor, Dr. Alessandro Molle, per avermi dato l'opportunità di intraprendere questo progetto di ricerca e aver creduto in me fin dall'inizio. Ringrazio inoltre il mio Tutor, Prof. Emiliano Bonera che, con competenza e professionalità, è stato di continuo supporto e altamente disponibile.
Un sincero ringraziamento anche al Prof. Fabio Pezzoli e a tutto il suo gruppo di ricerca per le misure effettuate e le discussioni dettagliate e stimolanti.

Ringrazio infinitamente il Dr. Carlo Grazianetti e il Dr. Christian Martella che i questi anni mi hanno seguito passo dopo passo; ringrazio Carlo per i numerosi consigli e spiegazioni sempre chiare ed esaustive e Christian per la condivisione di nuove idee e spunti di riflessione.
Un caro ringraziamento a Mario, che con la sua vasta esperienza è stato un punto di riferimento quotidiano sia per i processi in cleanroom che per discussioni tennistiche.
Un grazie di cuore ai i colleghi e gli amici del CNR-IMM che in qualsiasi modo mi hanno aiutato e contribuito ad arricchire la mia esperienza professionale e personale, in modo particolare a Eleonora e Pinak, per tutto quello che abbiamo condiviso in laboratorio ma soprattutto fuori.

Grazie agli amici di una vita per essere sempre al mio fianco, non importa dove e quando, e a Grazia per tutti i momenti trascorsi insieme.

Come promesso, un ringraziamento speciale allo staff di Fisio & Riabilita, in particolare Simone, Laura, Paolo e Francesca senza i quali sarebbe stato impossibile tornare così velocemente in laboratorio con un crociato nuovo.

Infine, dedico questo lavoro alla mia famiglia: i miei risultati sono soprattutto merito vostro.